The Astrophysical Journal, 987:13 (42pp), 2025 July 1 https://doi.org/10.3847/1538-4357/adce03

Unveiling the Diversity of Type IIn Supernovae via Systematic Light-curve Modeling

C. L. Ransome[1] and V. A. Villar[1,2]

[1] Center for Astrophysics | Harvard & Smithsonian, 60 Garden Street, Cambridge, MA 02138-1516, USA

[2] The NSF AI Institute for Artificial Intelligence and Fundamental Interactions, USA

Received 2024 September 14; revised 2025 February 18; accepted 2025 February 27; published 2025 June 23

Abstract

Type IIn supernovae (SNe IIn) are a highly heterogeneous subclass of core-collapse supernovae, spectroscopically characterized by signatures of interaction with a dense circumstellar medium (CSM). Here, we systematically model the light curves of 142 archival SNe IIn using the Modular Open Source Fitter for Transients. We find that the observed and inferred properties of SN IIn are diverse, but there are some trends. The typical supernova CSM is dense ($\sim 10^{-12}$ g cm^{-3}) with highly diverse CSM geometry, with a median CSM mass of $\sim 1\,M_\odot$. The ejecta are typically massive ($\gtrsim 10\,M_\odot$), suggesting massive progenitor systems. We find positive correlations between the CSM mass and the rise and fall times of SNe IIn. Furthermore, there are positive correlations between the rise time and fall times and the *r*-band luminosity. We estimate the mass-loss rates of our sample (where spectroscopy is available) and find a high median mass-loss rate of $\sim 10^{-2}\,M_\odot$ yr^{-1}, with a range between 10^{-3} and $1\,M_\odot$ yr^{-1}. These mass-loss rates are most similar to the mass loss from great eruptions of luminous blue variables, consistent with the direct progenitor detections in the literature. We also discuss the role that binary interactions may play, concluding that at least some of our SNe IIn may be from massive binary systems. Finally, we estimate a detection rate of 1.6×10^5 yr^{-1} in the upcoming Legacy Survey of Space and Time at the Vera C. Rubin Observatory.

Unified Astronomy Thesaurus concepts: Supernovae (1668); Core-collapse supernovae (304); Light curves (918); Astronomy data modeling (1859); Stellar mass loss (1613)

Materials only available in the online version of record: figure set, machine-readable tables

1. Introduction

As a massive star exhausts its nuclear fuel, radiation pressure can no longer support the stellar core, leading to a core-collapse supernova (CCSN). The underlying engines, progenitor systems, and immediate environments of stars shape the observed CCSN properties, leading to a zoo of spectral and photometric classes. Arguably, one of the most heterogeneous CCSN classes is the Type IIn supernova class (SN IIn), named such due to narrow features superimposed on emission lines. These narrow features are notably, but not exclusively, seen on the hydrogen Balmer lines, perhaps most obviously seen on the Hα profile (A. V. Filippenko 1989; E. M. Schlegel 1990; A. V. Filippenko 1997; C. L. Ransome et al. 2021).

This unique spectroscopic signature points to a complex circumstellar environment. Narrow emission features arise when the supernova (SN) ejecta collides with a preexisting dense and slow circumstellar medium (CSM; N. N. Chugai 1991; N. N. Chugai et al. 2004). The resultant complex emission profiles in the Balmer series can be decomposed into a narrow component with a full width at half-maximum (FWHM) of $\sim 10^2$ km s^{-1}, an intermediate width component (FWHM of $\sim 10^3$ km s^{-1}) and a broad component (FWHM of $\sim 10^3$–10^4 km s^{-1}), each arising from a unique component of the CSM or SN itself (N. N. Chugai 2001; N. N. Chugai et al. 2004; L. Dessart et al. 2009; R. M. Humphreys et al. 2012; C. Huang & R. A. Chevalier 2018). Early CSM interaction features are common among CCSNe, arising from the photoionization of a confined CSM or inflated H-rich envelope, photoionized by high-energy photons from the shock breakout (D. Khazov et al. 2016; J. Fuller & D. Tsuna 2024; W. V. Jacobson-Galán et al. 2024). However, these features fade within roughly a week and are distinct from the CSM interaction characteristic of Type IIn supernovae (SNe IIn) that are powered by shock interaction and endure much longer.

The dense CSM surrounding SN IIn must be created by the progenitor (or perhaps a companion) through mass-loss events toward the end of the star's life (N. Smith 2014). The progenitor mass loss may manifest from a diverse set of mechanisms. These mechanisms range from line-driven winds to dramatic outbursts, such as the great eruption of η Car in the 1880s, in which the progenitor lost mass at a rate of $\dot{M} \sim 1\,M_\odot$ yr^{-1}. This event produced a massive CSM, in excess of $10\,M_\odot$ (N. Smith et al. 2003, 2010). Alternatively, the mass loss may be due to interactions in a close binary system (A. Kashi et al. 2013; N. Soker & A. Kashi 2013; N. Smith 2014; A. Ercolino et al. 2024). A combination of these mechanisms may then produce a highly complex circumstellar environment. In some cases, mass-loss episodes are observed to precede the SN in the years or months prior to the terminal explosion (E. O. Ofek et al. 2014b; N. Smith et al. 2014; N. L. Strotjohann et al. 2021; T. Pessi et al. 2022; A. Reguitti et al. 2024). Other mass-loss mechanisms may include unstable burning (N. Smith 2014), gravity wave-driven pulsations (J. H. Shiode & E. Quataert 2014; S. C. Wu & J. Fuller 2022), and outbursts due to pair instability (for very massive progenitors, with an initial mass in excess of $100\,M_\odot$) (S. E. Woosley et al. 2007; S. I. Blinnikov 2010; S. E. Woosley 2017). However, for SNe IIn, high mass-loss rates are required to produce the solar masses of CSM in a relatively short period of time (the CSM interaction is typically prompt, so the CSM is not distant). The required mass-loss rates are between 10^{-3} and $10\,M_\odot\,\mathrm{yr}^{-1}$ (N. Smith 2014, 2017; N. Dukiya et al. 2024; D. Hiramatsu et al. 2024b), which precludes the classic line-driven winds of red supergiants (RSGs; E. R. Beasor et al. 2020).

A commonly suggested SN IIn progenitor system are luminous blue variables (LBVs), massive evolved stars that undergo dramatic mass-loss episodes (R. Kotak & J. S. Vink 2006; N. Smith 2014). A small number of SNe IIn have direct progenitor detections from pre-explosion images. For example, SN 2005gl had archival, pre-explosion Hubble Space Telescope (single-band) imaging, and it was found that the progenitor was a probable LBV with mass in excess of $50\,M_\odot$ (A. Gal-Yam et al. 2007; A. Gal-Yam & D. C. Leonard 2009). It has recently been found, however, that the environments of SNe IIn are inconsistent with the environments of single massive stars, i.e., they do not trace star formation, generally (J. P. Anderson et al. 2012; S. M. Habergham et al. 2014; C. L. Ransome et al. 2022), suggesting multiple progenitor types. Similarly, spectroscopic studies of the hosts of SNe IIn have unveiled that there may be a population of SNe IIn in a young environment, and a population in an older environment, with peaks in age bins of 0–20 Myr and 100–400 Myr (L. Galbany et al. 2018).

Proposed lower-mass progenitors include stars on the lowest end of the CCSN range (8–10 $M_\odot$) that end their lives as an electron-capture supernova (ecSN; e.g., SN 2011ht) (N. Smith et al. 2013). It should be noted, however, that some ecSN candidates are more consistent with flash ionization than CSM–ejecta interaction due to the fleeting interaction features (e.g., SN 2018zd) (J. Zhang et al. 2020; D. Hiramatsu et al. 2021). A notable possible low-mass SN IIn progenitor is that of SN 2008S (M. T. Botticella et al. 2009). This transient peaked at only $M_R \approx -14$ mag, leading to suggestions that this was more likely a massive star in eruption (i.e., an SN impostor) than a bona fide SN (e.g., N. Smith et al. 2009a). Pre-explosion data were analyzed by J. L. Prieto et al. (2008), who found a dust-enshrouded progenitor in Spitzer Space Telescope imaging. Those authors suggest that the source in the Spitzer data was consistent with a progenitor with an initial mass of $\approx 10\,M_\odot$. SN 2008S was also compared to other, seemingly non-terminal, transients such as NGC 300-OT, and others (e.g., E. Berger et al. 2009; T. A. Thompson et al. 2009; N. Smith et al. 2010, 2011; R. J. Foley et al. 2011). SN 2008S was dubbed an intermediate luminosity red transient, and has also been linked to electron-capture supernovae (ecSNe; M. T. Botticella et al. 2009). Unlike SN 2018zd, it had enduring CSM interaction features. Later work monitored the late-time evolution of SN 2008S, finding that the transient had become fainter than the pre-explosion progenitor; this suggests that SN 2008S may indeed be a terminal event (S. M. Adams et al. 2016). Alternatively, those authors also note that a surviving progenitor may be self-obscured by extreme dust, leaving the determination of the ultimate fate of this transient uncertain.

The progenitors of other SNe classes are known to shed mass, manifesting as the aforementioned "flash-ionization" SNe, and may also undergo more violent mass-loss events. For example, the more commonly observed CCSN progenitors, RSGs, i.e., the progenitors of SNe IIP and IIL (S. J. Smartt 2009; S. J. Smartt et al. 2009) may make up a proportion of the SN IIn progenitor channel. Based on environmental analyses, the distribution of the star formation association of SNe IIn can be recreated with a mix of the environments of LBVs and RSGs (T. Kangas et al. 2017). However, for enough material to be stripped from the star, a higher mass-loss rate than the canonical RSG wind (e.g., E. R. Beasor et al. 2020), or a different mass-loss mechanism is required (N. Smith 2006). N. Smith et al. (2009b) find that the mass loss of the galactic RSG, VY CMa, is episodic. High-resolution IR spectra of the circumstellar environment of this RSG show that there are CO clouds from mass ejections occurring approximately hundreds of years ago. The mass-loss rate, luminosity, wind speed, and mass are also found to be larger than those of Betelgeuse. Those authors conclude that the CSM produced by this star may result in an SN IIn. Indeed, one massive RSG progenitor has been observed to suffer from pre-explosion outbursts, leading to fleeting CSM interaction, i.e., the progenitor of SN 2020tlf (W. V. Jacobson-Galán et al. 2022). We do note, however, that such activity is seemingly not ubiquitous (e.g., SN 2023ixf and SN 2024ggi) and lacks any precursor in data in an extensive 5000+ day pre-explosion baseline, to deep limits of a few $10^4\,L_\odot$ in the case of SN 2023ixf (Y. Dong et al. 2023; C. L. Ransome et al. 2024; M. Shrestha et al. 2024). RSGs, particularly massive RSGs, may be an important lower-mass ($\lesssim 25\,M_\odot$) SN IIn progenitor route if there is prolonged (decades to centuries) mass loss; however, the lower end of LBV initial mass overlaps with the upper range of RSGs. Indeed, massive RSGs may possibly evolve blueward to form LBVs (N. Smith et al. 2004; N. Smith 2014). One possible progenitor of an SN IIn that may be a lower-mass ($\lesssim 25\,M_\odot$) star is SN 2016jbu, which may have had a yellow hypergiant progenitor, with an initial mass of $\approx 22\,M_\odot$ (S. J. Brennan et al. 2022), but C. D. Kilpatrick et al. (2018) found it to be consistent with a more massive LBV.

While there are some commonalities between members of the SN IIn class, such as the narrow components on the Balmer profile, a blue continuum (R. A. Stathakis & E. M. Sadler 1991; M. Turatto et al. 1993) and being generally more luminous than other SN II with an average observed peak of $M_B = -18.7$ mag (M. Kiewe et al. 2012), the SN IIn class is highly heterogeneous. Some SNe IIn are intrinsically faint, peaking at $M_V \approx -14$ mag (e.g., SN 2008S) (M. T. Botticella et al. 2009; S. M. Adams et al. 2016). Other SNe IIn lay within the "standard" CCSN region in the luminosity-timescale space of exploding transients (M. M. Kasliwal et al. 2011; V. A. Villar et al. 2017) with peak absolute magnitudes in the range of −17 to −19 mag (W. Li et al. 2011; M. Kiewe et al. 2012; F. Taddia et al. 2013). Furthermore on the extreme of the luminosity axis of the luminosity timescale, there are the superluminous SNe (SLSNe), where some Type II SLSNe (SLSNe II) may be powered by CSM interaction similarly to that of SNe IIn, i.e., an SLSN-IIn (N. Smith et al. 2007; S. Q. Wang et al. 2019). Indeed, the SN IIn, SN 2006gy, was the most luminous SN observed at the time of discovery with a peak absolute magnitude of $M_R \sim -21$ mag (N. Smith et al. 2007).

Furthermore, the light-curve morphologies of SNe IIn are highly diverse. On the extreme of the timescale axis of the luminosity-timescale phase space, some SNe IIn are long-lived in Hα emission due to ongoing CSM interaction. Some SNe IIn remain observable for decades post-explosion—for example, SN 1978K, which was only discovered in 1990, thought to be a classical nova initially but the SN was found in archival data (M. A. Dopita & S. D. Ryder 1990; S. Ryder et al. 1993;

Table 1

Sources of Our Sample of Spectroscopically Confirmed and Photometrically Monitored SNe

Source	Initial Sample	Number	Cut	Reference
ZTF Bright Transient Survey	118	85	33	C. Fremling et al. (2020a), D. A. Perley et al. (2020a)
Palomar Transient Factory	42	25	17	A. Nyholm et al. (2020)
Gold SNe IIn	37	8	29	C. L. Ransome et al. (2021)
Pan-STARRS1 Medium Deep	24	16	8	V. Villar et al. (2019)
Young Supernova Experiment (DR1)	13	9	4	P. D. Aleo et al. (2023)
Total	234	142	92	

Note. The number of SNe IIn is recorded along with the reference for the source. Some of the YSE sample overlaps with the ZTF sample. In these cases, we consider them as YSE SNe.

N. N. Chugai et al. 1995). The earliest example of a long-lived SN IIn was one of the original three SNe IIn in the sample of E. M. Schlegel (1990), SN 1988Z, with long-lived SNe IIn sometimes termed SN 1988Z-like or IIn-E (S. M. Habergham et al. 2014; D. Branch & J. C. Wheeler 2017). Perhaps the most well-known long-lived SN IIn is SN 2005ip. M. Stritzinger et al. (2012) found that the CSM interaction was still ongoing more than 6 yr post-explosion. The light-curve decline stalled in a plateau that remained at an almost constant brightness of ∼−15 mag for ∼5000 days. Furthermore, 3 yr post-explosion, SN 2005ip remained the strongest Hα source in its host, NGC 2906 (S. M. Habergham et al. 2014). SN 2005ip only began to decline more rapidly 5000 days post-explosion (O. D. Fox et al. 2020). These long-lived SNe IIn seem to form a small but interesting subgroup that may have a more extended CSM compared to other SNe IIn or perhaps a central engine driving ongoing CSM interaction. For a recent example of a long-lived SN IIn, see SN 2017hcc (N. Smith & J. E. Andrews 2020; P. Chandra et al. 2022a; S. Moran et al. 2023). Further to this long-lived behavior seen in some SNe IIn (see also O. D. Fox et al. 2013), "bumpy" light curves are observed, which may indicate interaction with denser regions of CSM, perhaps from more discrete mass-loss events from the progenitor (e.g., SN 2006jd and iPTF13z) (M. Stritzinger et al. 2012; A. Nyholm et al. 2017). The light-curve shapes that characterize the SN IIP (with recombination wave-driven plateaus) and SN IIL (linearly declining) classes are seen in some SNe IIn, designated SN IIn-P (e.g., SN 2011ht and PTF 11iqb) (J. C. Mauerhan et al. 2013; N. Smith et al. 2015) and SN IIn-L (e.g., SN 1998S and SN 1999el) (E. Di Carlo et al. 2002; F. Taddia et al. 2015). These may be considered members of a continuum of pre-SN mass loss, between that of more standard SNe II and "classical" SNe IIn.

The SN IIn class is highly heterogeneous, with great photometric, spectral, and environmental diversity. With the advent of large transient surveys in the past couple of decades, we now have a large population of SNe IIn, including hundreds of events. In this paper, we perform the first systematic physical modeling of a large sample of multiband SNe IIn light curves, with the aim of inferring their physical properties and the CSM that surrounds them. Throughout this work, we assume a standard reddening law, with $R_V = A_V/E(B-V) = 3.1$ according to J. A. Cardelli et al. (1989). We assume a standard flat ΛCDM cosmology with $H_0 = 67.7\,\mathrm{km\,s^{-1}Mpc^{-1}}$ and $\Omega_\mathrm{M} = 0.307$ (Planck Collaboration et al. 2016). This paper is organized as follows: In Section 2, we describe the models of SN IIn light curves and our approach to modeling our large sample. In Section 3, we outline our sample of 142 SNe IIn collected from various sources. In Section 4, we present our results and analysis, including our light curves, inferred parameter distributions, tests for clustering of parameters, and exploring correlations between parameter pairs, and then discuss the diversity of SN IIn light curves. We outline the photometric groupings of our sample in Section 5. The mass-loss rates of the progenitors are presented in Section 6. In Section 8, we discuss the implications of our findings for the possible progenitor routes of our SNe IIn. In Section 9, we describe future developments and present an estimate on the rates of SNe IIn in the upcoming wide field survey at the Vera C. Rubin Observatory. Finally, in Section 10, we summarize our findings.

2. Modeling the Light Curves of SNe IIn

We adopt the model for ejecta–CSM interaction-driven light curves that are used in the Modular Open Source Fitter for Transients (`MOSFiT`; J. Guillochon et al. 2017) developed by V. A. Villar et al. (2017) and B. Jiang et al. (2020), which builds on earlier work by W. D. Arnett (1980, 1982), R. A. Chevalier (1982), and E. Chatzopoulos et al. (2012). `MOSFiT`[3] is an open-source Python-based package that performs Bayesian inference on the multiband light curves of SNe and other thermal transients (J. Guillochon et al. 2017).

The ejecta–CSM interaction model follows the reverse and forward shocks produced by the interaction between the SN ejecta and CSM, both of which are assumed to be spherically symmetric. This interaction converts kinetic energy into thermalized radiation,

$$\begin{aligned} L &= \epsilon \frac{dE_\mathrm{kin}}{dt} = \frac{\epsilon}{2}\frac{d}{dt}(M_\mathrm{sw} v_\mathrm{sh}^2) \\ &= \epsilon\left(M_\mathrm{sw} v_\mathrm{sh}\frac{dv_\mathrm{sh}}{dt} + \frac{1}{2}\frac{dM_\mathrm{sw}}{dt}v_\mathrm{sh}^2\right) \end{aligned} \quad (1)$$

where ϵ is the efficiency coefficient of the conversion of kinetic energy to radiation in the CSM–ejecta interaction. Here, $\epsilon = 0.5$ is assumed (consistent with typical literature assumptions; e.g., A. J. van Marle et al. 2010; T. J. Moriya et al. 2012, 2013; L. Dessart et al. 2015; V. A. Villar et al. 2017). v_sh is the shock velocity, and the swept-up mass is M_sw.

Using the sample outlined in Table 1 and Section 3, along with the parameters described in Table 2, we use `MOSFiT` to fit the light curves of our sample of SNe IIn. The multiband light curves of our sample were downloaded from public repositories described in Section 3, with a small amount of private data. The CSM interaction model in `MOSFiT` assumes

---

[3] https://mosfit.readthedocs.io

Table 2
The `MOSFiT` CSM Model Prior Distributions Used in the Fitting of Our SN IIn Light Curves

Parameter	Value or Range of Values	Log-uniform Sampling	Median and Spread
$\log(N_{\rm H}/{\rm cm}^{-3})$	10^{16}–10^{23} cm^{-3}	True	$18.9^{+1.9}_{-1.9}$
$t_{\rm exp}$	-20–0 days	False	$-10.4^{+5.7}_{-7.7}$ days
$T_{\rm min}$	1–10^4 K	True	2587^{+4960}_{-2570} K
s	0–3	False	$1.37^{+0.67}_{-0.93}$
n	7–12	False	$9.44^{+1.79}_{-1.80}$
δ	0	Fixed	…
r_0	1–100 au	True	$13.1^{+35.2}_{-9.7}$ au
$\log(M_{\rm CSM}/M_\odot)$	0.1–50 $M_\odot$	True	$0.10^{+0.80}_{-0.57}$
$M_{\rm ej}$	1.0–50 $M_\odot$	False	$20.1^{+19.0}_{-14.9}$ $M_\odot$
$v_{\rm ej}$	10^3–10^5 km s^{-1}	True	4721^{+3750}_{-2022} km s^{-1}
$\log(\rho_0/{\rm g\ cm}^{-3})$	10^{-15}–10^{-10} g cm^{-3}	True	$-11.2^{+0.87}_{-1.08}$ g cm^{-3}
ϵ	0.5	Fixed	…
$\log(\sigma/{\rm mag})$	10^{-5}–1.0 mag	True	$-1.0^{+0.4}_{-1.3}$

Note. The median values from the joint posterior distributions are also shown with spread from the 16% and 84% confidence intervals.

an expanding blackbody, where the photospheric radius expands until a minimum temperature is reached (i.e., a floor temperature), at which point the photospheric radius recedes. `MOSFiT` fits for all bands, accounting for Milky Way $E(B-V)$ and fits for host extinction. The parameters in the CSM–ejecta interaction model are as follows: $M_{\rm CSM}$ is the CSM mass, $M_{\rm ej}$ is the mass of the SN ejecta, s is the CSM density profile exponent, where $\rho_{\rm CSM} \propto r^{-s}$, in which $s = 0$ would represent a shell-like CSM and $s = 2$ would represent a wind-like CSM profile, with a steeper profile approaching $s = 3$. Unlike previous works, we extend `MOSFiT` to include models up to $s = 3$ using the solution set from B. Jiang et al. (2020). n is the inner ejecta density profile parameter and δ is the outer ejecta density profile parameter (which we fix at 0) and are both indices in a power law that describes the SN ejecta density profile. The value of n is determined by the progenitor type; $n = 7$ would suggest a compact progenitor, and $n = 12$ would represent a more extended progenitor. R. A. Chevalier (1982) describe the ejecta density profile as a broken power law dependent on n and δ as indices with $\rho_{\rm SN} = g^n t^{n-3} r^{-n}$, where g^n is given by

$$g^n = \frac{1}{4\pi(\delta - n)} \frac{[2(5-\delta)(n-5)E_{\rm KE}]^{\frac{n-2}{2}}}{[(3-\delta)(n-3)M_{\rm ej}]^{\frac{n-5}{2}}} \tag{2}$$

where $E_{\rm KE}$ is the SN kinetic energy.

The inner ejecta density parameter, n, may determine whether the input luminosity increases or decreases for $t < t_{\rm FS}$, where $t_{\rm FS}$ is the shock-crossing time. This is also dependent on whether the CSM geometry is shell- or wind-like, respectively (as $L_{\rm inp} \propto {}^{\frac{2n+6s-ns-15}{n-s}}$). Brighter transients result if $n = 12$ for a shell-like CSM geometry ($s = 0$) compared to the wind-like ($s = 2$) case. r_0 is the inner CSM radius. $v_{\rm ej}$ is the representative velocity of the SN ejecta (related to the SN kinetic energy through $E_{\rm KE} = \frac{3}{10} M_{\rm ej} v_{\rm ej}^2$) and ρ_0 is the density of the CSM at the inner radius of the CSM. $t_{\rm exp}$ is the time of explosion, relative to the first observation. $T_{\rm min}$ is the minimum photospheric temperature—i.e., the temperature at which the photosphere begins to recede in our models. Finally, $N_{\rm H}$ is the host hydrogen column density.

We used nested sampling via `dynesty` (J. S. Speagle 2020) with 1000 live points to fit each light curve. Convergence is reached when the marginalized likelihood between samples stabilizes for a given stopping value. This is when the change in the log-evidence ($d\log z$) is below a given threshold (in this case, $d\log z = 0.1$). The redshift and Milky Way extinction are fixed using the values recorded in the literature or YSE-PZ (D. A. Coulter et al. 2023), which uses `dustmaps` (G. M. Green et al. 2018) and `extinction`[4] to calculate these values.

Additional quantities may be derived from the parameters inferred by `MOSFiT`. We calculate the mass-loss rate and the outer CSM radius. The CSM extent is calculated using

$$R_{\rm CSM} = \left(\frac{3M_{\rm CSM}}{4\pi\rho_0 r_0^s} + r_0^3\right)^{\frac{1}{3}}. \tag{3}$$

This CSM extent can be thought of as a lower limit, as we are only able to probe CSM that interacts with the SN ejecta within the observational window. Indeed, radio observations may also reveal interaction with distant, more diffuse CSM (e.g., P. Chandra et al. 2012). Furthermore, O. D. Fox et al. (2011) found that around 15% of SNe IIn exhibit late-time emission from preexisting dust. This dust was formed from material ejected from the progenitors in LBV-like eruptions.

Finally, we estimate the CSM velocity using the FWHM of the narrow component of the Hα emission line in velocity space (as per C. L. Ransome et al. 2021) so that we can estimate mass-loss rates. The CSM velocity may vary considerably, from ∼10 to 10^3 km s^{-1}, depending on the progenitor system. We do note, however, that the CSM may be radiatively accelerated; hence, this measured width may be larger than what would be measured for unshocked CSM. In high-resolution spectra, this may be seen as narrow absorption features.

Furthermore, we can take the parameters inferred by `MOSFiT`, and our estimates for the CSM velocities to estimate the mass-loss rates with other observational quantities, such as the luminosity. Utilizing the luminosity arising from the CSM–ejecta interaction, the mass-loss rate can be represented as

$$\dot{M} = 2\epsilon L \frac{v_{\rm CSM}}{v_{\rm sh}^3} \tag{4}$$

where L is the luminosity, $v_{\rm CSM}$ is the CSM velocity, and $v_{\rm sh}$ is the velocity of the shock, and ϵ is the efficiency of the conversion of kinetic energy to radiation (e.g., N. Smith 2017; D. Dickinson et al. 2024; N. Dukiya et al. 2024). Those authors assume the shock velocity to be 2500 km s^{-1} (see also N. Smith 2014). In this work, however, we estimate the shock velocity from our model in `MOSFiT`, which traces the position of the shock front (both forward and reverse shock fronts) over time.

The shock velocity can be directly calculated from spectral modeling (e.g., S. J. Brennan et al. 2023). However, a relatively high-resolution spectroscopic measurement is required for these calculations. In lieu of these measurements, we can take the time derivative of the position of, for example,

---

[4] https://github.com/kbarbary/extinction

the reverse shock, as calculated in `MOSFiT`, which uses the solutions of E. Chatzopoulos et al. (2012),

$$\frac{dr_{\rm RS}}{dt} = \frac{d}{dt}\left(r_0 + \beta_r \left[\frac{(Ag^n)}{D}\right]^{\frac{1}{n-s}} t^{\frac{n-3}{n-s}}\right) \tag{5}$$

where $r_{\rm RS}$ is the position of the reverse shock front at time t. β_r and A are constants that are dependent on s and n. We assume a constant $v_{\rm sh}$ for these mass-loss rate calculations, taking the average value over the first 100 days after $t_{\rm exp}$, the time of explosion.

These inferred parameters, as well as being informative on the SN characteristics, may also inform on progenitor properties such as the mass-loss rates. These mass-loss rates may be linked to the progenitors themselves (e.g., N. Smith 2017). Observed features can also be used to infer the physical parameters of SNe IIn. For example, the rise times and peak luminosities can be used to constrain the CSM density, SN ejecta energy, and ejecta mass (T. J. Moriya et al. 2012, 2014). The model used by those authors is similar to that of E. Chatzopoulos et al. (2012) but differs in that their models of the bolometric light curve assume that the unshocked CSM is optically thin (i.e., the diffusion time is much shorter than the shock-crossing time). Therefore, this model traces the evolution of the shock more directly.

Recent efforts have also explored more complex light-curve morphologies observed in SNe IIn, such as bumps and rebrightenings, which cannot be reproduced in our model. D. K. Khatami & D. N. Kasen (2024) approach this problem by considering different ejecta mass to CSM mass ratios and a "breakout" parameter. The breakout parameter is related to where the shock breakout occurs, where the shock emerges from the outer CSM, and the degree of the deceleration of the shock. Those authors demonstrate that different sets of parameters (e.g., more CSM than ejecta or vice versa) can reproduce features such as the secondary "humps" seen in some SNe IIn such as SN 2019zrk (C. Fransson et al. 2022). R. Chiba & T. J. Moriya (2024) found that for $s \neq 2$, models that use a dense CSM and follow the evolution of the shocks, and where the shocks emerge from the CSM, can reproduce various light-curve shapes. These models can also reproduce the long plateaus characteristic of the long-lived SNe IIn. A notable example of an SN IIn with a clear rebrightening is SN 2021qqp (D. Hiramatsu et al. 2024b). The secondary bump in this object was likely due to the SN ejecta interacting with material ejected from a violent precursor mass-loss event, and was reproduced by pre-SN eruption models adapted from T. Matsumoto & B. D. Metzger (2022).

Another photometric category of SNe IIn that has been explored is SLSNe IIn. In particular, L. Dessart et al. (2015) present radiation-hydrodynamic simulations of interaction-powered SLSNe (i.e., SLSNe IIn) in 1D and 2D. Those authors use a multigroup radiation transport approach implemented in the `HERACLES` code in order to model the photometric and spectroscopic properties with a more realistic treatment of opacities of SLSNe IIn. The models of L. Dessart et al. (2015) reproduce the evolution of photometry, spectroscopy, and polarimetry of SLSNe IIn based on input explosion energetics, ejecta characteristics, mass-loss rates, and CSM configuration. These simulations were able to reproduce the observed photometric, spectroscopic, and polarization characteristics of the well-known SNe IIn SN 2006gy and SN 2010jl. Given the simplifying assumptions of our model, we directly compare our models to those of L. Dessart et al. (2015). We find a general agreement in the inferred CSM masses, presented in Appendix A, suggesting that `MOSFiT` provides reliable CSM estimates for the range explored here.

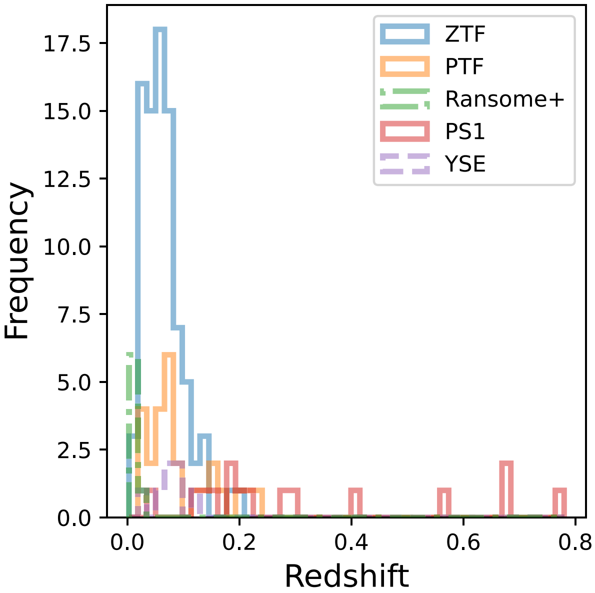

Figure 1. The redshift distribution of our SN IIn sample. The majority of our sample is relatively nearby with $z < 0.1$, but this range extends to more distant redshifts ($z \simeq 0.8$) with the inclusion of SNe IIn discovered by the Pan-STARRS1 Medium Deep survey.

3. The Sample

We select our sample following the schema described by C. L. Ransome et al. (2021). Our sample of SNe IIn spans an explosion date from 1989 to 2023, covering a redshift range of 0.003–0.780 (shown in Figure 1). The observed (uncorrected for Malmquist bias) mean absolute peak r-band magnitude of our sample is −19.2 mag with a standard deviation of 1.0 mag; the peak r-band absolute magnitude distribution is shown in Figure 2. We also show the Malmquist-corrected distribution in Figure 2; we describe this correction in Figure 18 in Appendix B. These SNe IIn have reliable spectroscopic classifications such that we can rule out misclassified SNe that exhibit early-time flash-ionization features. Our selected sample also requires sufficient photometric coverage for our inference (i.e., we exclude events with small observing baselines or with significant temporal gaps). Finally, we do not include objects where the reduced photometric data are not easily publicly accessible. Our sample and the sources are summarized in Table 1.

After thorough inspection of the reported SNe IIn, we note that some objects are likely nuclear transients (such as active galactic nuclei (AGN)), based on the object being highly central to their hosts and red color evolution inconsistent with SNe IIn. If there is insufficient spectral information to confirm an SN IIn classification, we exclude the transient from our sample. Moreover, we exclude bona fide SNe IIn that exhibit multiple peaks in their light curve (e.g., SN 2019zrk) (C. Fransson et al. 2022; N. Soker 2022) or are extremely long lasting, such as SN 2005ip, as these cases are not an appropriate application of the E. Chatzopoulos et al. (2012) models.

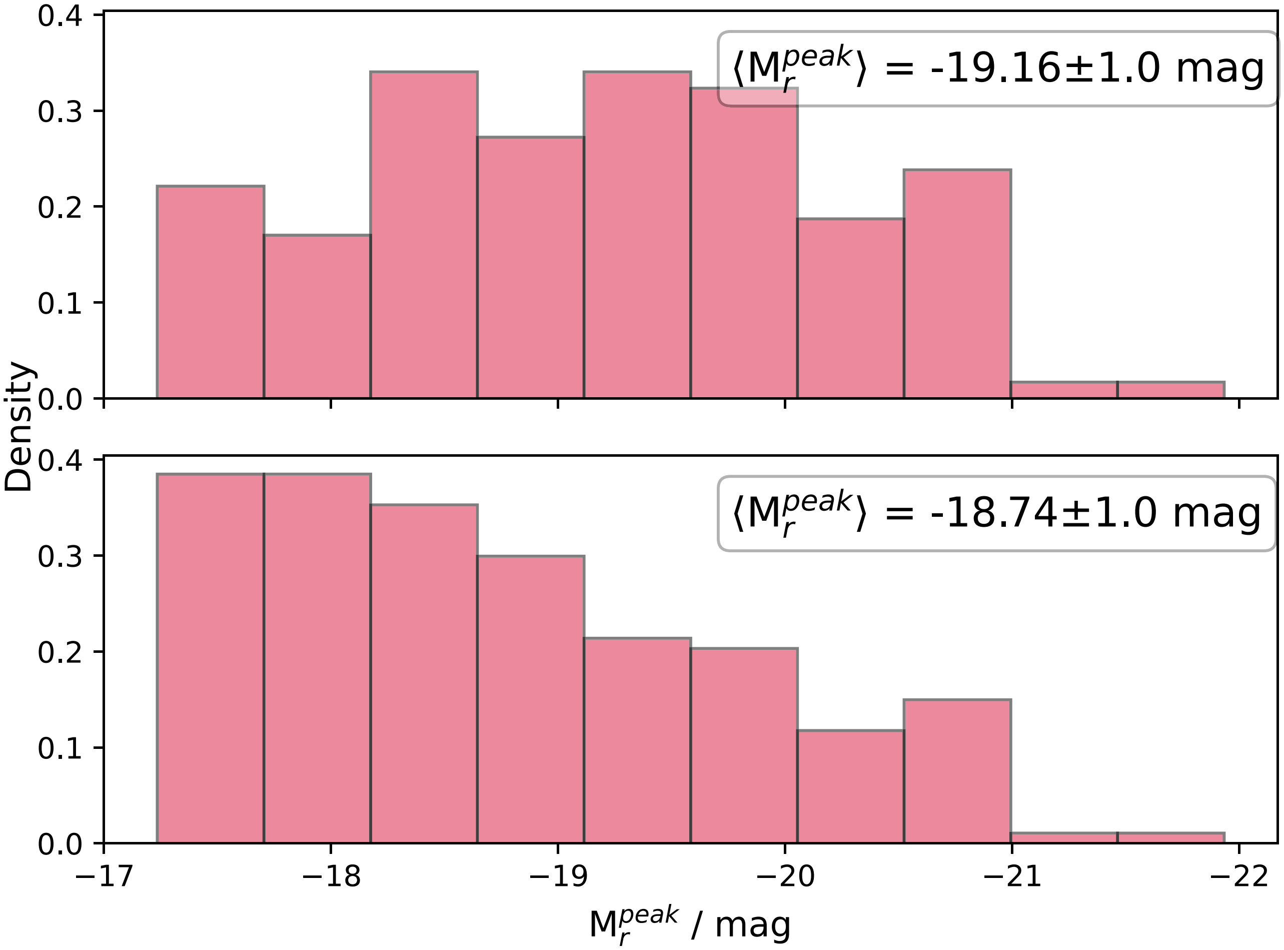

Figure 2. The peak r-band absolute magnitude distribution for our sample of SNe IIn. These distributions are corrected for host and Milky Way extinction. The top panel is the observed distribution and the bottom panel is Malmquist corrected.

Our general selection criteria can be summarized as follows:

1. There is at least one spectrum taken over a week post-discovery to rule out flash-ionization SNe (see D. Khazov et al. 2016; W. V. Jacobson-Galán et al. 2024).
2. The Hα profiles should be complex (with at least two Gaussian components). Moreover, the spectra should be SN spectra, rather than narrow host lines misinterpreted as interaction signatures (see C. L. Ransome et al. 2021).
3. There are data covering a baseline of at least 50 days for our inference.
4. The SNe should not have clear "bumps" in the light curves (e.g., dip and rise) again, as in the case of SN 2021qqp (D. Hiramatsu et al. 2024b).

Our SNe IIn were selected from both the literature and large optical surveys. Our largest source for SNe IIn (with 85 members) is the Zwicky Transient Facility Bright Transient Survey (ZTF BTS). The SNe IIn from the ZTF BTS[5] are spectroscopically confirmed (e.g., using SEDMachine) (N. Blagorodnova et al. 2018) and are typically observed in two filters: g and r bands (C. Fremling et al. 2020a; D. A. Perley et al. 2020a). The ZTF BTS spectroscopic sample includes only transients with apparent magnitudes $<$19 mag. The transients in this sample extend to a redshift of ~ 0.2. Of the excluded transients from this subsample (of a total of 119), 15 are excluded for having a short baseline, 13 have either no publicly available spectra or the available spectra were within 7 days post-discovery, and five had bumps or double peaks. One additional object is central to its host and has a very red peak (with $g - r \approx 1$ mag), indicating this transient may be an AGN rather than an SN IIn.

Our next largest source of events is the Palomar Transient Factory (PTF; S. B. Cenko et al. 2006), and this sample is presented in the light-curve analysis of A. Nyholm et al. (2020). The majority of the full sample of 42 from A. Nyholm et al. (2020) have a single classification spectrum, but the majority of these do have a spectrum after our 7 day cut. From these 42 SNe IIn, we use 25 in our analysis. The photometry for this subsample was obtained from WISEeREP[6] (O. Yaron & A. Gal-Yam 2012). These SNe extend to a redshift of ∼0.2. Of this sample, 12 of the SNe had a short baseline or data quality issues (one transient had large uncertainties on all points); four had an ambiguous classification spectrum (either within our cutoff range or exhibiting strong host lines), and one had a bumpy light curve.

We incorporate eight SNe IIn, which were presented by C. L. Ransome et al. (2021) from their "gold" sample. These objects are from the literature and are well-studied transients with well-sampled spectroscopy, exhibiting CSM interaction signatures for multiple epochs. All events in this sample are within

---

[5] https://sites.astro.caltech.edu/ztf/bts/bts.php

[6] https://www.wiserep.org

$z <= 0.02$. These observations include data from numerous filters from multiple instruments and telescopes. In their full gold sample, C. L. Ransome et al. (2021) identify 37 transients. We cut 29 of these objects from our sample. Of these cut SNe, 22 had no easily obtainable public photometric data, four were long-lived SNe IIn, two were thermonuclear, and one is possible an SN impostor.

The 16 SNe IIn from the Pan-STARRS1 Medium Deep Survey (K. C. Chambers et al. 2016a) are the spectroscopically confirmed sample of SNe IIn (V. Villar et al. 2019). These SNe IIn tend to be more distant (out to redshift ∼0.78) than the relatively nearby transients in our other sources and are observed in five bands, Pan-STARRS (*grizy*). The full Pan-STARRS1 sample consisted of 24 SNe. Out of the eight excluded transients from this sample, seven had short baselines, and another had an incorrect redshift measurement.

Finally, we incorporate an additional eight SNe IIn from the first data release (DR1) of the Young Supernova Experiment (YSE; D. O. Jones et al. 2021; P. D. Aleo et al. 2023). Of these, three overlap with ZTF BTS in this sample, but these eight SNe were discovered by YSE in the Pan-STARRS griz filters. In total, there are 13 SNe IIn from the YSE DR1 subsample. Out of these five excluded SNe, three have a spectrum within 1 week of discovery, and one has a short baseline.

As our data originate from various sources, a small amount of cleaning was required. This mostly takes the form of treating data points with a signal-to-noise ratio (SNR) of less than 3 as an upper limit. We also truncate earlier times where precursor emission was identified, but including the "main" event (which would be much brighter; this was only seen in two objects). After data filtering, our sample consists of 142 SNe IIn (with 92 transients removed from an initial sample of 234, outlined in Table 1).

4. Exploring the Sample

Our full set of light-curve fits and inferred parameters for our sample of 142 SNe IIn are presented in online tables and figure sets. We also present the light curves of our sample in Figure 3. These light curves show the data and models for each filter per SN with an offset for legibility. Also plotted are the realizations (independent samples from the posterior distribution) inferred by `MOSFiT`. Complementary to these light curves is an example parameter corner plot (Figure 4), showing the marginalized posterior distributions inferred by our `MOSFiT` light-curve modeling.

4.1. Inferred SN Properties

We first examine the joint posterior distributions for the inferred SN and CSM properties from `MOSFiT`. The median parameter values and the 16th/84th percentile spread in the distribution are shown in Table 3. Note that these values are calculated using *all* posterior realizations. Furthermore, to assess the quality of our fits, we consider a white noise parameter, σ (in units of magnitude), which is inferred by `MOSFiT`. This gauges the underestimation of uncertainty in the data. The median white noise value is $\log(\sigma/\mathrm{mag}) = -1$. This metric suggests that there may be some unaccounted for uncertainties or short-term variability in the data, which is then compensated for with the σ parameter in our fits. We next explore the most interesting physical parameters in more detail.

The parameter that governs the CSM density profile, s, is left as a free parameter and varied between 0 and 3. This parameter is informative on the progenitor mass-loss mechanisms, although it is often fixed to either $s = 0$ or 2 or assumed to be the latter (T. J. Moriya et al. 2012; E. O. Ofek et al. 2014a). Note that $s = 0$ corresponds to an eruptive mass-loss episode, while $s = 2$ corresponds to a constant ("wind-like") mass loss, a steeper CSM density profile is given by $s > 2$. The full distribution of inferred s values is shown in the top left panel of Figure 5. It can be seen from this distribution that there is a peak toward higher values of s, i.e., more wind-like; however, the joint distribution spans the prior range, showing great diversity. Generally, s is well constrained when the individual transient posterior distributions are considered.[7] This joint posterior distribution has a median and spread of $1.37^{+0.67}_{-0.93}$, with a typical uncertainty of ∼0.2 for individual events. While there is a slight preference toward wind-like constant mass loss, generally, the SN IIn sample does not undergo mass loss at a steady rate.

The distribution of the SN ejecta geometric parameter, n, which was varied between 7 and 12, is shown in the top right panel of Figure 5. This parameter is related to the polytropic index of the core of the progenitor. For example, an RSG-like progenitor is consistent with $n = 12$, and an LBV or Wolf–Rayet–like progenitors may have n values between 7 and 10 (e.g., S. A. Colgate & C. McKee 1969; C. D. Matzner & C. F. McKee 1999). We find a fairly uniform spread in the distribution of n; however, there is a preference for lower values. Similarly to s, in the literature, n is often fixed. Typically, values of 7, 10, or 12 are assumed (e.g., R. A. Chevalier & C. M. Irwin 2011; T. J. Moriya et al. 2013, 2014). The median value and spread of the joint posterior distribution of n are $9.44^{+1.79}_{-1.80}$. The typical uncertainty for individual SNe is ∼0.9, i.e., our posteriors for n are broad and therefore only somewhat informative. Therefore, the wide spread in n seen in Figure 5 may be due to model uncertainty.

The bottom panels of Figure 5 show the full posterior distributions of the inner CSM radius, r_0 (right), and the CSM density at this inner radius, ρ_0 (left). r_0 is varied between 1 and 100 au, representative of the radii of evolved stars, assuming the inner CSM radius is similar to the progenitor radius (e.g., A. Fassia et al. 2001; T. J. Moriya et al. 2017; V. Morozova et al. 2017; L. Dessart & D. J. Hillier 2022). This range is also consistent with the prior distribution used by V. A. Villar et al. (2017). We vary ρ_0 between 10^{-15} and $10^{-10}\,\mathrm{g\,cm^{-3}}$, consistent with theoretical studies of CSM interaction-powered SNe (e.g., L. Dessart et al. 2015; O. Yaron et al. 2017; D. Tsuna et al. 2023). This range also covers the higher densities found for interaction-powered SLSNe IIn, for example, SLSN-IIn, ASSASN-15ua (D. Dickinson et al. 2024, was found to have a CSM density of $\approx 10^{-10}\,\mathrm{g\,cm^{-3}}$). The majority of our SN IIn sample requires high CSM densities within a few tens of astronomical units (of the order 10^{14} cm), with the distributions of ρ_0 peaking at $\sim 10^{-12}\,\mathrm{g\,cm^{-3}}$. The median inner CSM density and spread are $\log(\rho_0/\mathrm{g\ cm^{-3}}) = -11.2^{+0.9}_{-1.1}$ with a typical individual uncertainty of ∼0.4. This distribution is skewed to the denser end of our prior distribution. While this distribution does tend toward a high-density CSM, the individual posterior distributions (shown in Appendix C) generally do not cut off at the prior edge and are typically well constrained. The distribution of r_0 has a median and spread of $13.1^{+35.2}_{-9.7}$ au. The typical uncertainty is ∼2 au. We show the distribution of ρ_0 against

---

[7] Presented in Figure 19 in Appendix C.

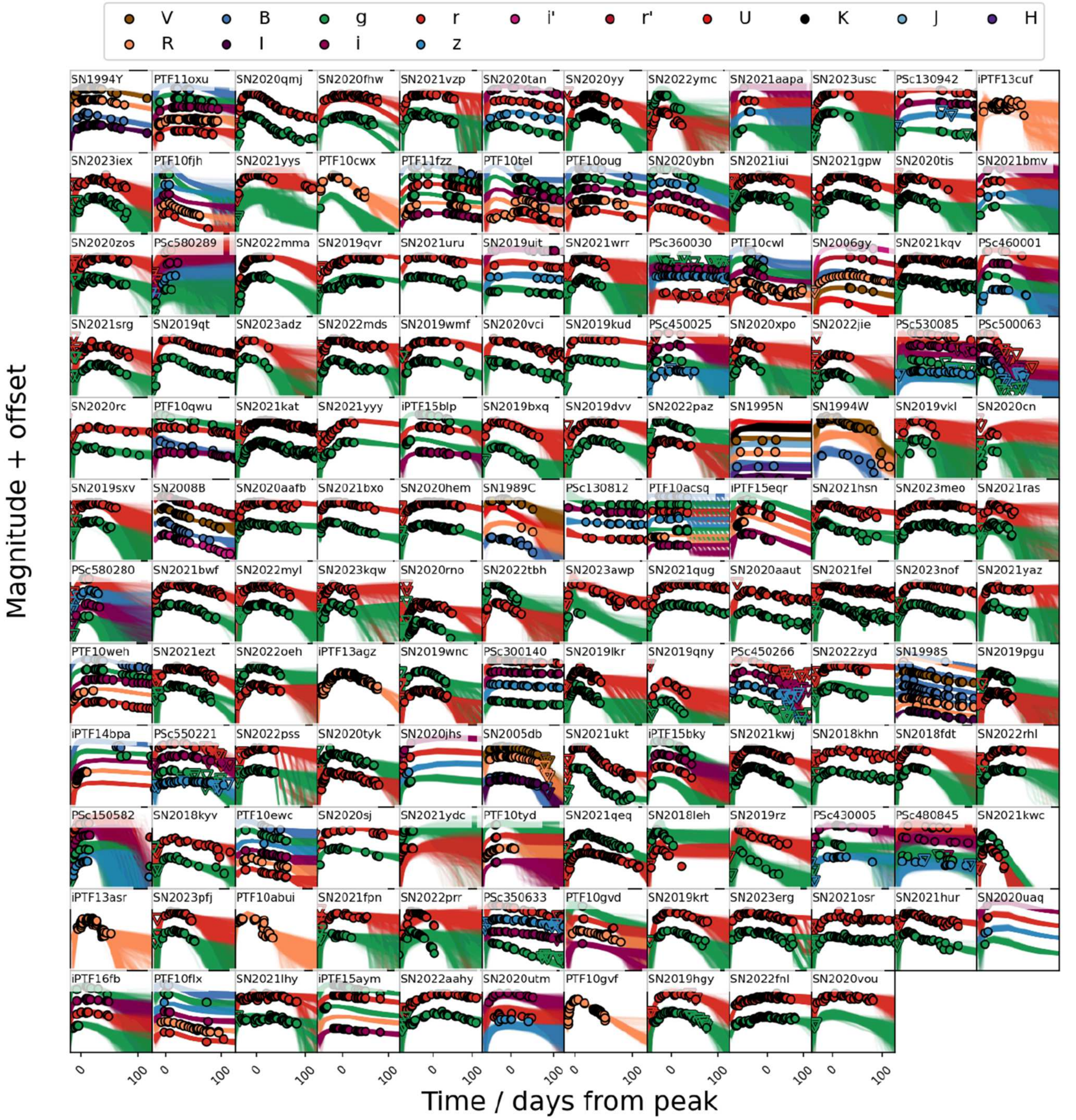

Figure 3. The photometric data and the `MOSFiT` fits for each of our 142 SNe IIn. Each band that is fit is offset for clarity. The time range covers the full range of the observed data. Detections are shown as solid circles and upper limits are shown as upended unfilled triangles. Note that the x-axes are not aligned for each subplot. The x-axis labels show time relative to the peak.

r_0 in Figure 6. We find that there is generally a negative correlation between r_0 and ρ_0, with a smaller inner CSM radius having higher CSM densities.

The CSM mass distribution is shown in the top left panel of Figure 7. We vary the CSM mass distribution between 0.1 and 50 $M_{\odot}$. The lower end of this prior range is consistent with that used by V. A. Villar et al. (2017) and probes examples of SNe IIn in the literature with lower CSM masses, such as SN 1994W (N. N. Chugai & I. J. Danziger 1994; L. Dessart et al. 2009). We extend the upper range of our prior distribution compared to V. A. Villar et al. (2017), however, to account for the high mass CSM seen around LBVs. The famous η Car, for example, has tens of solar masses of CSM (e.g., N. Smith et al. 2003). Other SNe IIn with estimated CSM masses in the literature include SN 2005gl (0.03 $M_{\odot}$) (A. Gal-Yam & D. C. Leonard 2009; S. J. Smartt 2009), SN 2005ip (a few solar masses) (N. Smith et al. 2009c, 2017; O. D. Fox et al. 2020, SN 2010jl (3–10 $M_{\odot}$) (C. Fransson et al. 2014; E. O. Ofek et al. 2014c), and SN 2017hcc ($\sim$10 $M_{\odot}$) (N. Smith & J. E. Andrews 2020). In our distribution, there is a clear peak around 1 $M_{\odot}$ (with a median and spread of $\log(M_{\rm CSM}/M_{\odot}) = 0.10^{+0.80}_{-0.57}$). For an individual SN, the typical uncertainty is around 0.4 $M_{\odot}$, implying most are well

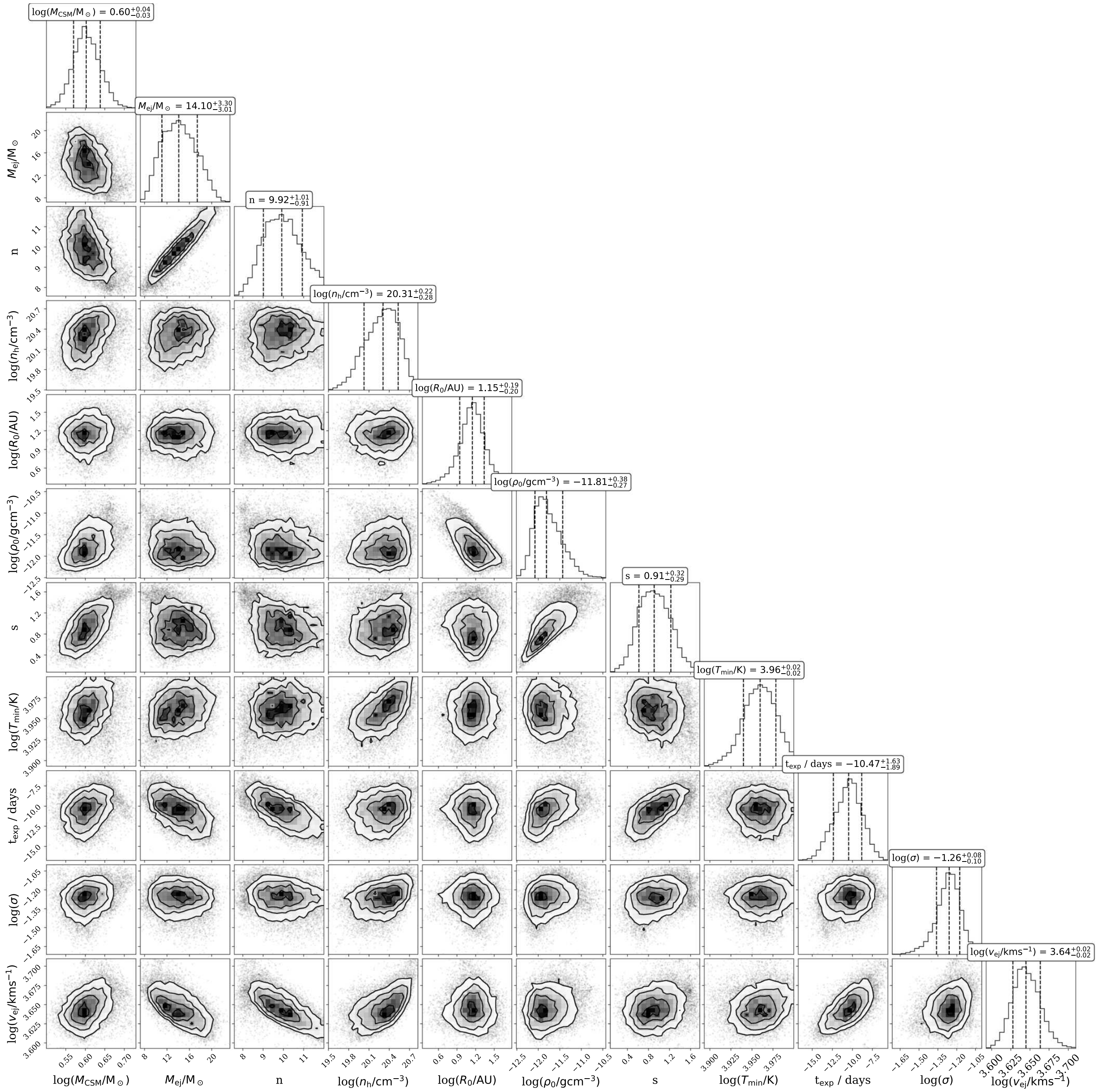

Figure 4. Corner plot for SN 2021gpw, one of the SNe IIn from the ZTF BTS subsample with data in the *gr* bands. Shown are the posterior distributions of each parameter used in the model implemented by `MOSFiT`, with the median and 16% and 84% confidence intervals on the distribution. The complete figure set (142 images) is available in the online journal. In addition, copies of the figures can be found at https://github.com/AstroSkip/Unveiling_data.
(The complete figure set (142 images) is available in the online article.)

constrained. This CSM mass distribution is largely consistent with the literature values.

In the top right panel of Figure 7, we present the joint posterior distribution for the ejecta mass. Our prior ranges between 1 and 50 $M_\odot$. This range was chosen to account for progenitors that are stripped, and therefore have lower ejecta masses (e.g., the low ejecta masses inferred for SN 1988Z, SN 2011ht, and SN 2020pvb) (N. N. Chugai & I. J. Danziger 1994; N. N. Chugai 2016; N. Elias-Rosa et al. 2024), and also massive progenitors that may have large ejecta masses (e.g., ASASSN-14il) (N. Dukiya et al. 2024). The ejecta mass distribution peaks at the highest values of our prior. The median value of the ejecta mass and spread is $20.1^{+19.0}_{-14.9}\,M_\odot$, consistent with more massive progenitor systems. The typical spread for any individual event is $\sim 8\,M_\odot$, suggesting that the marginal posterior distributions are broad.

The bottom left panel of Figure 7 shows the distribution of the total mass, which we define as

$$M_{\rm tot} = M_{\rm CSM} + M_{\rm ej}. \tag{6}$$

The total mass describes the lower limit of the mass of the progenitor prior to its death. It excludes the mass of a remnant

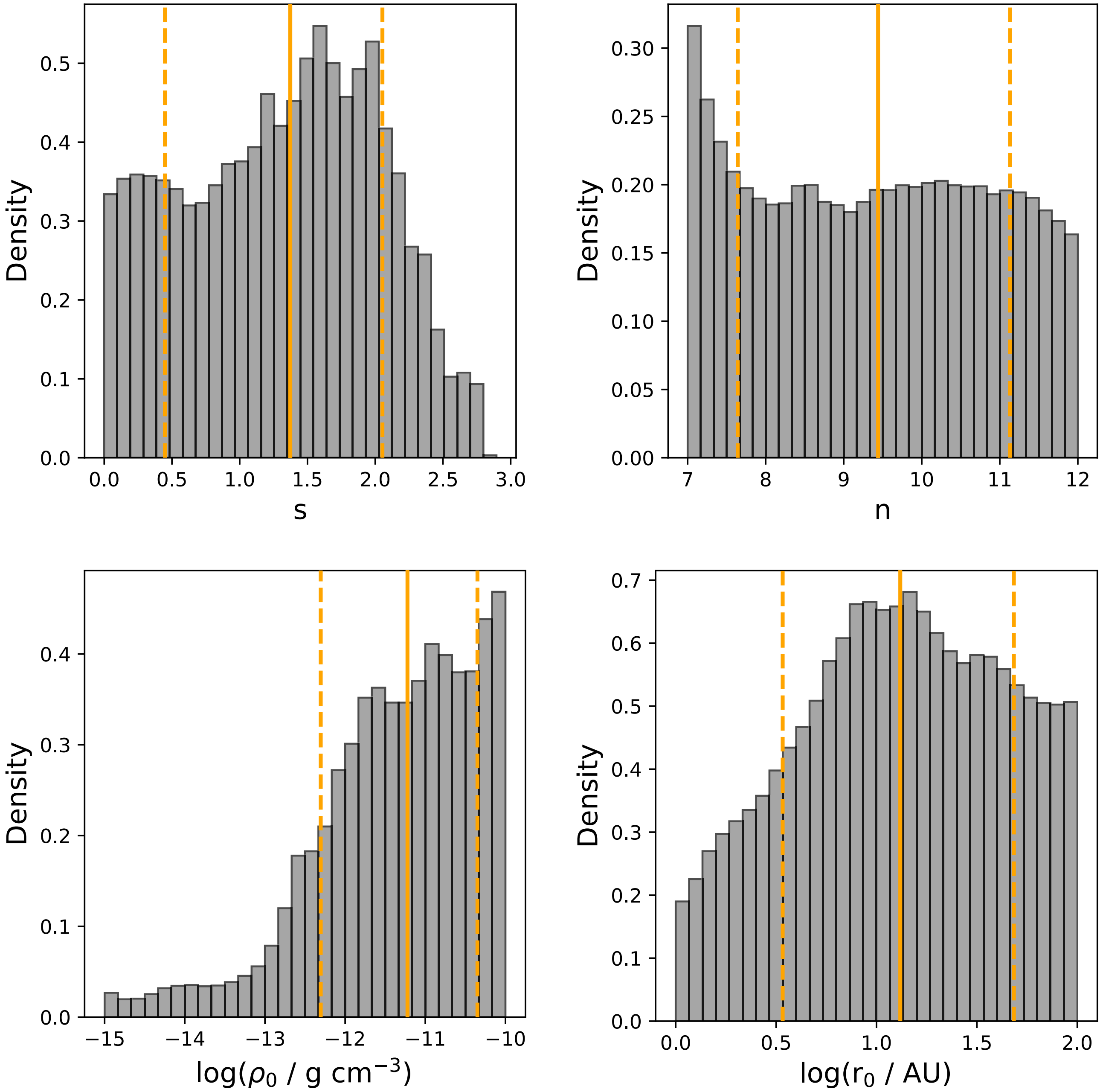

Figure 5. Histograms showing parameter distributions for our SNe IIn, calculated by `MOSFiT` light-curve modeling. Top left: the distribution of the geometric parameter that describes the CSM density profile, s. Top right: the distribution of n, which governs the inner SN ejecta density profile. Bottom left: the distribution of the inner density of the CSM in log-space. Bottom left: the distribution of the inner CSM radius.

Table 3
The Median Values of the Properties Derived from Observational Information and Also the Median Value for Calculated Quantities Derived Using Parameters from `MOSFiT`

Parameter	Median and Spread	Method
$M_{\mathrm{peak},r}$	18.7 ± 1.0 mag	Observed
Rise time	$39.2^{+22.5}_{-15.5}$ days	Observed
Fall time	$55.7^{+73.5}_{-27.2}$ days	Observed
$\log(E_{200}\ \mathrm{erg}^{-1})$	$50.3^{+0.5}_{-0.7}$	Derived
R_{CSM}	$73.5^{92.3}_{-30.7}$ au	Derived
t_{CSM}	$2.94^{+2.37}_{-0.49}$ yr	Derived
$\log(\dot{M}/M_\odot\ \mathrm{yr}^{-1})$	$-1.06^{+0.82}_{-1.14}$	Derived
v_{sh}	2846^{+2850}_{-1665} km s^{-1}	Derived
v_{CSM}	370^{+157}_{-209} km s^{-1}	Spectra

and diffuse CSM beyond the limits of our light-curve probe. In Figure 7, one can see that the population distribution roughly follows that of the ejecta mass, with a median total mass and spread of $\sim 24^{+19}_{-16}\,M_\odot$. This is consistent with typical literature estimates for SN IIn progenitors (N. Smith et al. 2011; I. Boian & J. H. Groh 2018; S. J. Brennan et al. 2022). This range covers both the "canonical" massive LBVs and the lower progenitor mass estimates. For example, SN 1994W, SN 2009kn, and SN 2011ht had progenitor mass estimates of $\approx 10\,M_\odot$; however, it is noted that these explosions may have been weakened by a newly formed black hole from a more massive progenitor (J. Sollerman et al. 1998; E. Kankare et al. 2012; N. Smith 2013; N. N. Chugai 2016; N. Elias-Rosa et al. 2024). Assuming it was indeed a terminal event, SN 2008S had

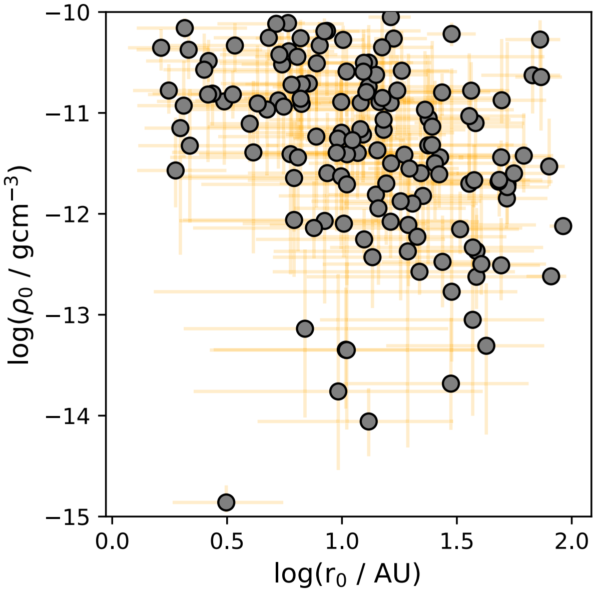

Figure 6. The distribution of ρ_0 at the respective r$_0$. Generally, the CSM density is lower for larger inner CSM radii.

pre-explosion data that suggested a low-mass progenitor of $\approx 10\,M_\odot$ (J. L. Prieto et al. 2008).

The final parameter of note we discuss is the representative ejecta velocity. The velocity distribution is shown on the bottom right of Figure 7. This distribution is apparently normally distributed around a median and spread of 4810^{+3454}_{-2082} km s^{-1}. The typical uncertainty in velocity is ∼400 km s^{-1} and the individual posteriors shown in Figure 19 are well constrained. These velocities are typical of the ejecta velocities of SNe IIn measured from broad line profiles in spectra (e.g., C. L. Ransome et al. 2021).

Finally, we search for multimodality within the parameter distributions described in this section. As SNe IIn are highly heterogeneous, probing for distinct groupings may prove informative on possible progenitor paths. In order to test for clustering in the SN IIn parameter distributions, we utilize a Gaussian mixture model approach (GMM; D. A. Reynolds 2009) with `scikit-learn` v1.4.2 (F. Pedregosa et al. 2011). The GMM attempts to describe our distributions with k-independent Gaussian distributions, each with differing means and variances. Using the Bayesian information criterion (BIC), we can determine the number of Gaussian distributions that best fit our data without overfitting. Here, we restrict our search to a combination of (at most) $k = 3$ Gaussians, similarly to the analysis of A. Nyholm et al. (2020). We consider distributions to be multimodal if the BIC score for $k = 2$ or $k = 3$ is significantly lower ($\Delta\mathrm{BIC} > 10$) than the $k = 1$ case. We note that this is a more stringent limit than used in previous work (e.g., J. Sollerman et al. 2009; A. Nyholm et al. 2020).

As the individual posterior distributions themselves are not necessarily normally distributed, we test the validity of using the median posterior values for our GMM analysis. We pseudo-bootstrap our sample by taking each SN IIn the light-curve fit and randomly sampling one realization (i.e., the individual light-curve fits) for each event. This is then repeated 10^3 times. For each resampling, the GMM analysis is repeated, with the mean of each Gaussian component from the GMM being recorded along with the variance. We find that the number of Gaussian components for each physical parameter is consistent with the number of components when we use the median value of each posterior distribution.

Some quantities may be derived from the inferred parameters from `MOSFiT`. For example, the CSM radius is presented in the bottom right panel of Figure 8. The CSM typically extends to a few 10^{15} cm, consistent with some estimates of CSM radii in the literature (T. J. Moriya et al. 2017; L. Dessart & D. J. Hillier 2022). However, we do note that the CSM radii derived from the models implemented by `MOSFiT` may underestimate the CSM radii when compared to other methods. This can be seen in the case of SN 2021foa where the CSM radius was $\sim 10^{14}$ cm (D. Farias et al. 2024). Given the typical shock velocities for SNe IIn (a few 10^3 km s^{-1}), and the duration of the typical interaction (over 100 days), one may expect the CSM radius to be more extended than a relatively confined region around the progenitor. Indeed, when there is spectroscopic follow-up, the interaction features my persist for many days (to years), indicating higher CSM radii, typically at least $\sim 10^{16}$ cm (e.g., SN 1998S, SN 2005ip, SN 2006jd, SN 2010jl and SN 2015da) (A. Fassia et al. 2001; P. Chandra et al. 2012; S. Katsuda et al. 2013; E. Dwek et al. 2017; N. Smith et al. 2017; L. Tartaglia et al. 2020). Moreover, A. L. Ibik et al. (2025) probe the mass-loss history of PS 11aop. Those authors follow the interaction using spectra and radio observations and compare the CSM radii using different models and observations. It was found that the models in `MOSFiT` (both with and without considering radioactive nickel decay) yielded a CSM radius of a few 10^{15} cm, while a simple CSM model extended to over 10^{16} cm, and radio observations showed that interaction was still occurring at radii exceeding 10^{17} cm. When we apply our GMM analysis to this distribution, we do not find multiple components. However, there is a peak at around 80 au and an apparent tail in the distribution that extends out to 10^3–10^4 au. As mentioned before, these CSM radii may be a lower limit as the optical light curves of our SNe IIn track interaction with relatively close material. More diffuse CSM further from the progenitor may exist from winds or previous episodes of mass loss.

To test for clustering in two dimensions, i.e., clustering in parameter pairs, we extend this GMM analysis. We fit two-dimensional Gaussian distributions with differing means and covariances to the parameter pair distributions. We do not find any clear examples of multiple components in the parameter pair distributions.

4.2. Observational Features

In addition to the parameters derived from `MOSFiT`, we extract observational features from our SN sample: the rise time, fall time, and peak brightness in the r band (used to compute the peak r-band absolute magnitude). We define rise time as the time taken to rise from t_{exp} to peak r-band brightness as calculated from the model light curves. We define the fall time as the time taken for the transient to fade by 1 mag from peak brightness (a similar analysis was performed by A. Nyholm et al. 2020, to which we compare our findings). We calculate the rise time and fall time directly from the `MOSFiT` model light curves. The subset of SNe IIn we use for this analysis is mostly made up of the ZTF BTS subsample, as it is the largest subsample with consistent use of the same r-band filter. In the ZTF BTS subsample, there are 89 SNe with

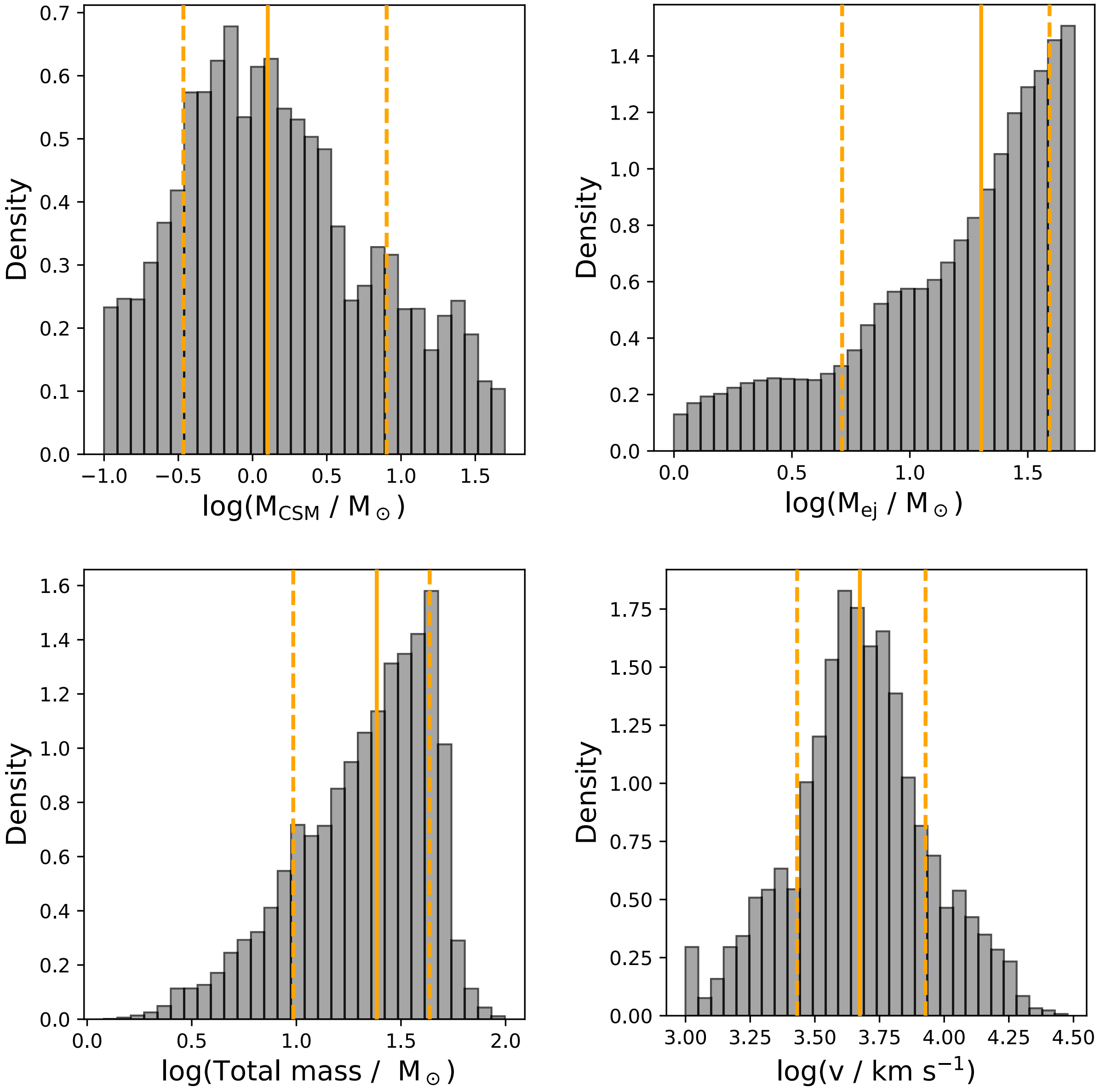

Figure 7. Histograms showing parameter distributions for our SNe IIn, calculated by `MOSFiT` light-curve modeling. Top left: the distribution of the CSM mass in log-space. Top right: the distribution of the ejecta mass. Bottom left: the distribution of the total mass (CSM mass + SN ejecta mass), roughly the pre-explosion progenitor mass minus the mass of a compact remnant such as a neutron star or black hole. Bottom left: the distribution of the outer CSM radius.

a measurable fall time metric. To account for time dilation, we correct these times by a factor of $(1 + z)$. The peak magnitudes are additionally corrected for extinction (host and Milky Way) and converted into absolute magnitudes. We do not attempt any k-corrections beyond the cosmological k-correction (which is not a concern given the low redshift distribution of the ZTF BTS subsample).

We present the distributions of the observational parameters in Figure 9. We find that the median rise time in the r band and spread is 39^{+16}_{-23} days. Our rise time distribution does not exhibit clear multimodality, but may have a tail at longer rise times. A. Nyholm et al. (2020) used a GMM test to find a possible bimodal population of fast and slow risers in their sample of PTF SNe IIn. Those authors find a fast-rising population with a mean of ∼20 days and a slow-rising population of SNe IIn with a mean rise time of ∼50 days. Our distribution peaks between these two possible populations, and the spread encompasses them. It should, however, be noted that the sample presented by A. Nyholm et al. (2020) is significantly smaller than our sample (32 SNe versus 142). Our method of calculating the rise time also differs from those authors. They fit a $\propto t^2$ power law to the rise of their light curves based on a template rising light curve of one of their SNe, assuming a smooth rise to peak brightness. While our methods are consistent for around half of the common sample, their method may produce somewhat faster rise times compared to our model. The input luminosity is dependent on n and s, and our input luminosity is given by $L_{\mathrm{in}} \propto t^{\alpha}$, so we typically have $\alpha < 2$, slowing the rise to peak.

The bottom panel of Figure 9 shows the distribution of the fall times of our SNe IIn. Our r-band fall time distribution has a median and spread of 56^{+74}_{-27} days. Our GMM analysis suggests that there is bimodality in the posterior distributions of the fall time. One component has a mean around the median of the distribution at 38 days with a standard deviation of 23 days, and the second component, at a longer fall time has a

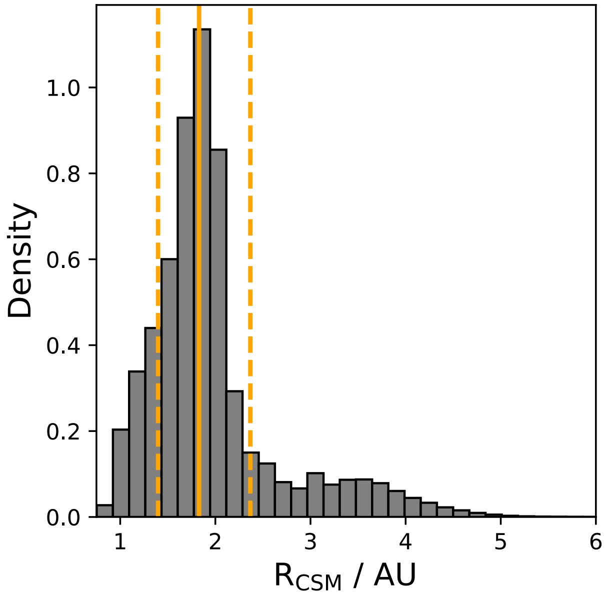

Figure 8. The joint posterior distribution of the CSM radius. The solid vertical line denotes the median value, and the dashed vertical lines mark the 16% and 84% spread. There peak in the distribution around 100 au. We note that there is an apparent tail to this distribution, but this is due to fits where bimodal solutions were found. Therefore, we do not consider a true bimodality in the CSM distribution.

mean of 194 days with a standard deviation of 16 days. We contrast this bimodality with the findings of A. Nyholm et al. (2020). They find a population of fast and slowly declining SNe IIn, where an average decline rate is defined in mag day^{-1} and is measured between 0 and 50 days post-peak magnitude. Converting to our fall time metric (i.e., 1/decline rate), these two populations correspond to a mean fall time of ∼25 days and 77 days. In other words, our faster peak has a mean in between the two modes of A. Nyholm et al. (2020) and our slower component is more than twice as long. It is possible that this difference is related to the definition of fall time (where we do not assume a constant decline rate). Our fall time metric, however, is roughly consistent with the decline rate measured by A. Nyholm et al. (2020) for the same objects in their PTF sample. This difference may simply be due to our larger sample; there are three objects with a fall time greater than 200 days and 13 are over 100 days. Finally, we note that we exclude the very slowly fading, long-lived SNe IIn in this analysis. At late times, the contribution of the Hα emission line (due to ongoing CSM interaction) starts to dominate over the continuum (e.g., SN 2005ip), which initially faded linearly followed by a plateau around 150 days post-peak (O. D. Fox et al. 2020), we discuss this effect in Appendix D. We also exclude transients that do not fade by 1 mag within the time frame of the data.[8]

In Figure 10, we show the distribution of the radiated energy of our sample of SNe IIn. To calculate the radiated energy of our SNe IIn, we take our posteriors and generate a bolometric luminosity light curve using the `MOSFiT` CSM model. We then integrate these bolometric light curves over a standard 200 day interval for consistency, resulting in an estimate of E_{200} (similar to the procedure employed by I. Salmaso et al. 2025). We find that the distribution of the radiated energy has

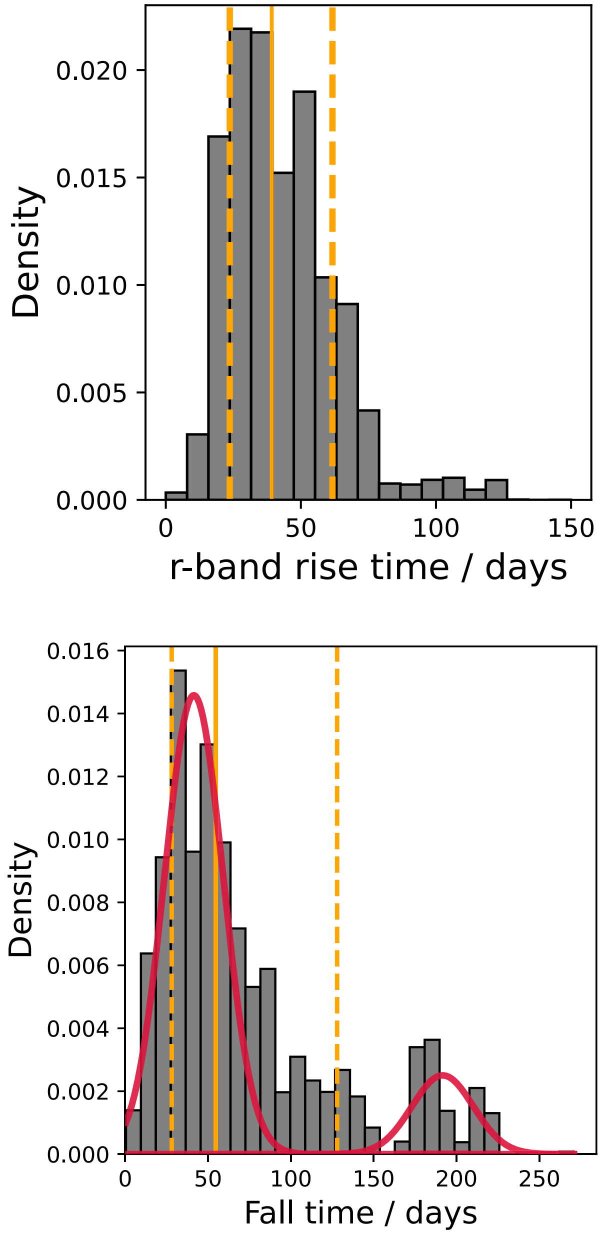

Figure 9. Top: r-band rise time distribution, defined as the rise from t_{exp} to peak brightness. The orange vertical lines denote the median (solid line) and the 16% and 84% spread (dashed lines). Bottom: the fall time distribution with the median and spread denoted by the solid and dashed orange lines. Also, in red, are the Gaussian components from the GMM analysis, showing a main component of a few tens of days and another component of longer-lasting SNe.

a median and spread of $\log(E_{200}\ \mathrm{erg}^{-1}) = 50.3^{+0.5}_{-0.7}$. Again, we repeat our GMM analysis and do not find evidence of a statistically significant multimodal distribution. We do note that there may be apparent peaks in the distribution at $\log(E_{200}\,\mathrm{erg}^{-1}) \approx 49.6$ and 50.4.[9] D. Hiramatsu et al. (2024a) recently found bimodality in their sample of SNe IIn, with peaks at a few 10^{49} erg and a few 10^{50} erg. Such bimodality may point to multiple progenitor routes, we discuss this result further in Section 8.

---

[8] However, these are compared as a silver sample, presented in Appendix E. We find that these distributions are consistent with each other.

[9] As the distribution seems to be multimodal by eye, we also tested for multimodality using a dip test and the bimodality coefficient. Both additional tests also suggest that there is no statistically significant evidence for multimodality.

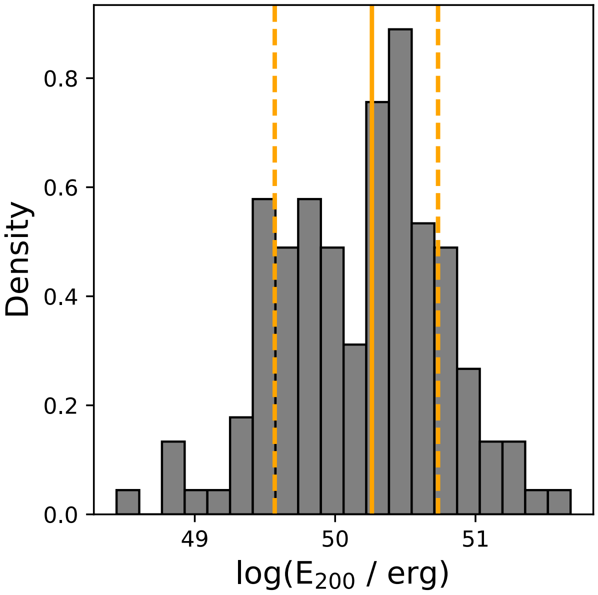

Figure 10. The integrated radiated energy of our sample of SNe IIn. We use the radiated energy over 200 days, E_{200} for consistency. Our GMM analysis does not indicate that there are multiple Gaussian components in this distribution at a high statistical significance.

4.3. Relations between Pairs of Parameters

To assess correlations in our parameters, we use the Pearson correlation coefficient (PCC; K. Pearson 1907). Implementing a bootstrapping method similar to T. J. Moriya et al. (2023), we resample 10^4 times. For each resample, we take one random sample from the posterior distribution of each object and then calculate the PCC. We can then calculate the standard deviation of the PCC (taking this as the uncertainty), and also the p-value. We use the PCC and bootstrapping implementation in `SciPy` (P. Virtanen et al. 2020).

The most salient correlations (as determined by our bootstrapping method) are shown in Figures 11 and 12. We find a positive correlation between: the r-band rise time and the CSM mass and the inner CSM density ($p < 0.05$); the fall time and the CSM mass and the inner CSM density ($p < 0.05$); the rise time and fall time ($p < 0.05$); and the fall time and peak r-band absolute magnitude ($p < 0.05$). The mass-loss rate (which we derive from other parameters described in detail in Section 6) is positively correlated with rise times ($p < 0.05$). Finally, we find negative correlations between the mass-loss rate and s.

Some of these correlations have been noted in the literature from smaller samples. A. Nyholm et al. (2020) note that their fast-rising SNe IIn tended to decline faster and vice versa. Those authors also show the correlation between the peak r-band absolute magnitude and the decline time (with 27 of their objects being used in this analysis). The rise and fall times are positively correlated with the CSM mass, and this is likely due to the diffusion timescale in the ejecta–CSM interaction models of E. Chatzopoulos et al. (2012) being proportional to the (optically thick) CSM mass as $\tau_{\rm diff} \propto M_{\rm CSM-thick}$. The diffusion timescale governs the rise time, with longer diffusion times producing a longer rise to peak. A longer diffusion timescale also produces a broader peak and slower decline. This may suggest that more massive progenitor systems (assuming massive progenitors have a more massive CSM) produce slower evolving SNe IIn with a higher mass-loss rate. There is a weaker, but significant, correlation (with a PCC of ∼–0.27) between the peak r-band absolute magnitude and the CSM mass. Hence, tentatively, brighter SNe IIn may be more likely to be slowly evolving and originating from a massive progenitor that has produced massive CSM.

A possible bias in this analysis is the lack of sufficient follow-up for some transients. The population with fall time estimates is smaller due to this lack of follow-up, perhaps missing some of the even slower declining transients as they have not decayed by 1 mag in the time frame of the observations.[10] It is unlikely that these observational biases impact the correlations discussed, as the well-studied, long-lived SNe IIn have high CSM masses. These long fall time, high CSM mass SNe also positively correlate with the mass-loss rate, a relation which is corroborated by slowly declining SNe IIn in the literature (e.g., ASASSN-14il, SN 2015da, and SN 2017hcc) (N. Smith & J. E. Andrews 2020; P. Chandra et al. 2022b; N. Dukiya et al. 2024; N. Smith et al. 2024), which had mass-loss rates of 0.1—a few solar masses per year and CSM masses of tens of solar masses.

While the salient correlations are presented in Figures 11 and 12, there are a number of significant PCC values between parameter pairs. These are shown in Figure 13. While there are more parameter pair relations that are "significant" due to their p-values, we only highlight the parameter pairs that we determine to have at least a moderate positive or negative correlation (i.e., a PCC over 0.3 or under −0.3). These relations are not further considered.

5. The Photometric Diversity of SNe IIn

Our `MOSFiT` modeling has revealed that the SN IIn population exhibits great diversity in its physical parameters, reflective of the diverse observable properties. The literature has identified several subgroups of SNe IIn: fast/slow risers, short/long fall time events, and under/overluminous events (e.g., J. L. Prieto et al. 2008; M. Stritzinger et al. 2012; S. M. Habergham et al. 2014; E. O. Ofek et al. 2014a; T. J. Moriya et al. 2018; A. Nyholm et al. 2020; L. Dessart & D. J. Hillier 2022). In this section, we discuss these photometric groupings, which are also summarized in Figure 14.

5.1. Rapidly Declining SNe

In our sample, there are 14 SNe IIn that display relatively rapid declines from peak, with a fall time of under 30 days (a timescale consistent with the short decliners of A. Nyholm et al. 2020). As an example, one of the fastest declining examples in our sample is PTF 10fjh (P. Challis et al. 2010a; G. Duszanowicz 2010; E. O. Ofek et al. 2014b). PTF 10fjh has a fall time of ∼ 15 days. This transient has a low CSM mass of $\sim 0.5\,M_\odot$, which is consistent with our observational correlations presented in Section 4.3. More broadly, the fraction of these short fall time SNe IIn is consistent with the fraction of fast decliners in the sample of A. Nyholm et al. (2020), when converted into our fall time metric. This is 18% of our subsample of 89 SNe IIn with a measurable fall time.

As a whole, this subgroup has small CSM masses, with a median of $\sim 0.45\,M_\odot$, again consistent with our correlations

---

[10] But we do extend our light-curve models with these objects, finding a similar distribution. This silver sample is presented in Appendix E, finding a similar distribution.

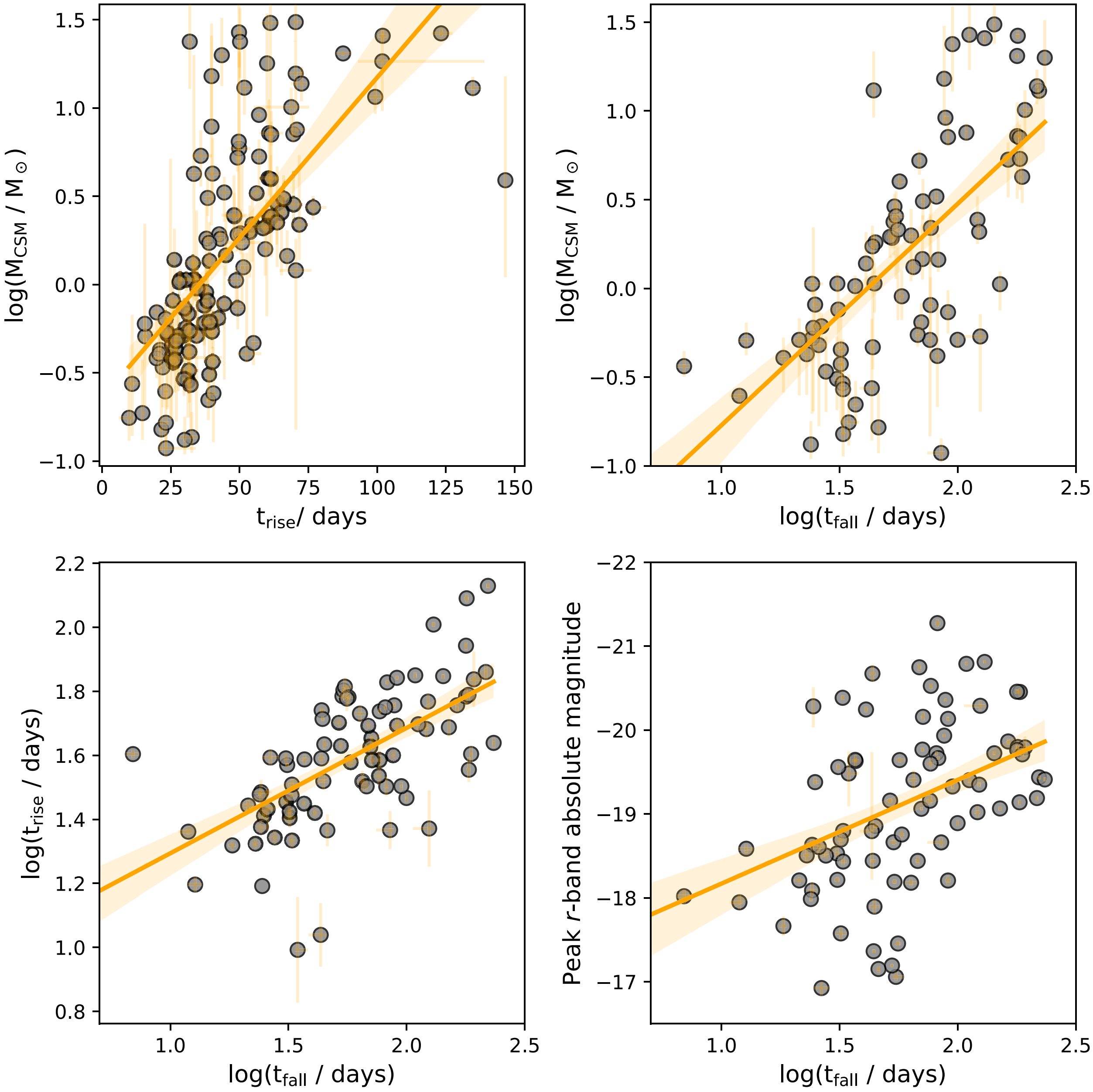

Figure 11. Parameter pair plots between observational and derived parameters from `MOSFiT`. Also plotted is the best-fit line from the PCC test, with the 1σ uncertainty region shaded for the correlation. Top left: the log–log scatter plot of the CSM mass against the *r*-band rise time to peak brightness. Top right: the log–log pair plot comparing the CSM mass to the *r*-band fall time. Bottom left: the log–log pair plot comparing the *r*-band rise time to peak against the *r*-band fall time, again showing a clear correlation. Bottom right: the log–log pair plot comparing the mass-loss rates against the *r*-band fall time.

between CSM mass and the fall times. These objects also tend to be relatively dim when compared to the full sample, with a median peak *r*-band absolute magnitude of –18.2 mag. These transients are also typically fast risers, consistent again with our correlations. We discuss the rise time subpopulations in the next section.

5.2. Slow and Fast Risers

As found by A. Nyholm et al. (2020), the SNe IIn population seems to contain subgroups based on their rise times to peak. These rise times are positively correlated with their fall time, as shown by Figure 11, which is likely due to the amount of CSM around the progenitor. One such fast riser in our sample is SN 2021kwc, which was discovered by ZTF (A. Dahiwale & C. Fremling 2021a; F. Forster et al. 2021h) and had a rise time to peak in the *r* band of ∼20 days. We find that SN 2021kwc has a small CSM mass of $\sim 0.4\,M_\odot$ and also had a short fall time of ∼25 days. Moreover, SN 2021kwc is on the lower end of our luminosity distribution with a peak *r*-band absolute magnitude of ∼–18.0 mag. Conversely, our slowest rising SN IIn is SN 2019qvr (F. Forster 2019a; C. Fremling et al. 2019f). This transient takes ∼120 days to rise to the *r*-band peak. This transient has $25\,M_\odot$ of CSM, with the fall time of ∼190 days and bright peak magnitude at $M_r = -19.8$ mag. For SN 2019qvr, $s \approx 1.6$, which indicates that the mass loss was not at a constant rate. It should be noted that slow-rising, interaction-driven SNe may have a flatter CSM density profile, with $s < 1.5$ (T. J. Moriya 2023; R. Chiba & T. J. Moriya 2024). This is within the spread of the

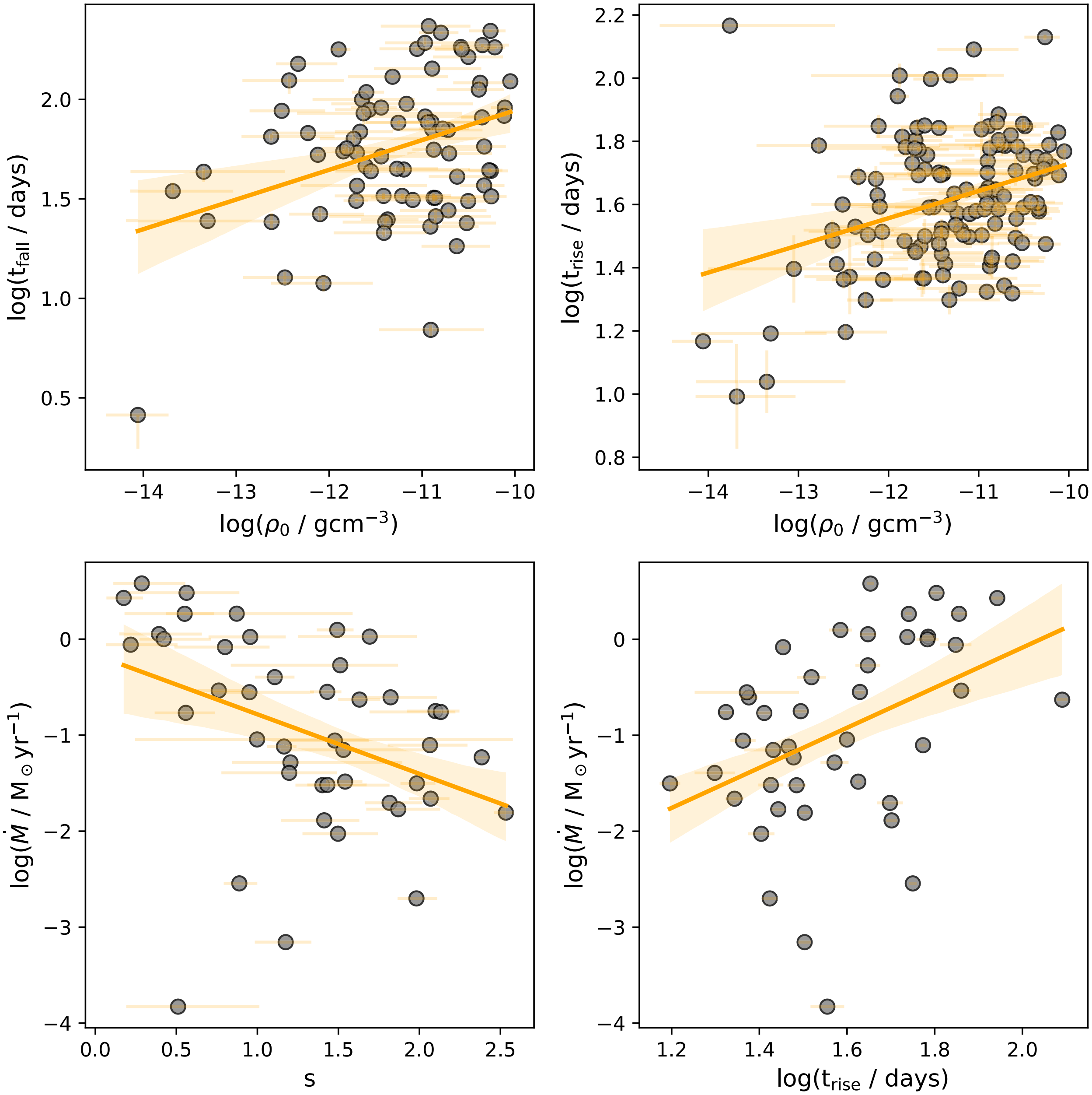

Figure 12. Parameter pair plots showing the correlations between parameters. Also plotted is the best-fit line from the PCC test, with the 1σ uncertainty region shaded for the correlation. Top left: the log–log scatter plot of the fall time against the inner CSM density. Top right: the log–log pair plot comparing the r-band rise time to the inner CSM density. Bottom left: the log–log pair plot comparing s to the mass-loss rate. Bottom right: the log–log pair plot comparing peak r-band absolute magnitude to the mass-loss rate.

distribution for SN 2019qvr, and the majority of the slower evolving SNe in our sample have s smaller than 1.5. The inferred mass-loss rate of SN 2019qvr is high, with a mass-loss rate of over $\sim$0.2 $M_\odot$ yr^{-1}. These two objects exemplify our correlations: objects with higher CSM masses evolve more slowly than SNe IIn with low CSM masses. When considering both of these subgroups, the median CSM mass for the short risers is $\sim$0.5 $M_\odot$, while the median CSM mass is $\sim$ 12.1 $M_\odot$ for the slow risers.

Generally, SNe IIn rise slowly relative to other SN classes. Indeed, around 34% of our sample have a rise time of 50 days or greater, a somewhat greater proportion than is found by A. Nyholm et al. (2020), who find that 25% of their sample had these longer rise times. Those authors find that around a third of their sample had a rise time of less than 20 days (the mean value of their "short risers"). Our sample has around 25% of the SNe IIn being fast risers, with a rise time of under 30 days. This contrasts with the findings of A. Nyholm et al. (2020), who found $\sim$ 65% of their sample were these faster rising transients. As previously mentioned, this may be a result of their method possibly producing faster rise time estimates.

5.3. Long-lived SNe

The photometric SN IIn subclass characterized by a slow light-curve decay is sometimes denoted as the "1988Z-like SNe IIn," after the archetype (e.g., N. N. Chugai & I. J. Danziger 1994; M. Stritzinger et al. 2012; S. M. Habergham et al. 2014). This subpopulation has also been noted in other, small sample size works (e.g., M. Kiewe et al. 2012; F. Taddia et al. 2013;

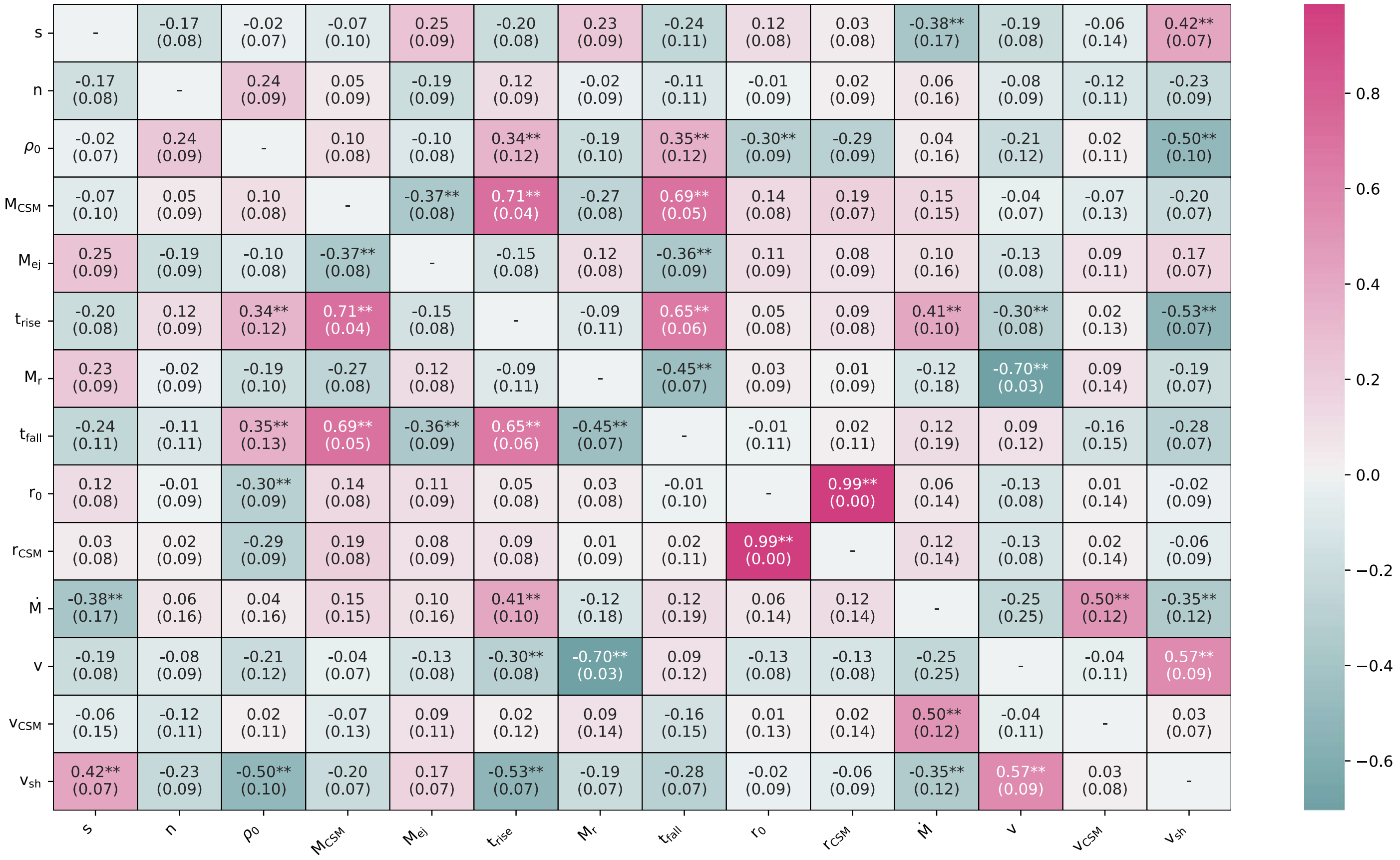

	s	n	ρ_0	M_{CSM}	M_{ej}	t_{rise}	M_r	t_{fall}	r_0	r_{CSM}	$\dot{M}$	v	v_{CSM}	v_{sh}
s	-	-0.17 (0.08)	-0.02 (0.07)	-0.07 (0.10)	0.25 (0.09)	-0.20 (0.08)	0.23 (0.09)	-0.24 (0.11)	0.12 (0.08)	0.03 (0.08)	-0.38** (0.17)	-0.19 (0.08)	-0.06 (0.14)	0.42** (0.07)
n	-0.17 (0.08)	-	0.24 (0.09)	0.05 (0.09)	-0.19 (0.09)	0.12 (0.09)	-0.02 (0.09)	-0.11 (0.11)	-0.01 (0.09)	0.02 (0.09)	0.06 (0.16)	-0.08 (0.09)	-0.12 (0.11)	-0.23 (0.09)
ρ_0	-0.02 (0.07)	0.24 (0.09)	-	0.10 (0.08)	-0.10 (0.08)	0.34** (0.12)	-0.19 (0.10)	0.35** (0.12)	-0.30** (0.09)	-0.29 (0.09)	0.04 (0.16)	-0.21 (0.12)	0.02 (0.11)	-0.50** (0.10)
M_{CSM}	-0.07 (0.10)	0.05 (0.09)	0.10 (0.08)	-	-0.37** (0.08)	0.71** (0.04)	-0.27 (0.08)	0.69** (0.05)	0.14 (0.08)	0.19 (0.07)	0.15 (0.15)	-0.04 (0.07)	-0.07 (0.13)	-0.20 (0.07)
M_{ej}	0.25 (0.09)	-0.19 (0.09)	-0.10 (0.08)	-0.37** (0.08)	-	-0.15 (0.08)	0.12 (0.08)	-0.36** (0.09)	0.11 (0.09)	0.08 (0.09)	0.10 (0.16)	-0.13 (0.08)	0.09 (0.11)	0.17 (0.07)
t_{rise}	-0.20 (0.08)	0.12 (0.09)	0.34** (0.12)	0.71** (0.04)	-0.15 (0.08)	-	-0.09 (0.11)	0.65** (0.06)	0.05 (0.08)	0.09 (0.08)	0.41** (0.10)	-0.30** (0.08)	0.02 (0.13)	-0.53** (0.07)
M_r	0.23 (0.09)	-0.02 (0.09)	-0.19 (0.10)	-0.27 (0.08)	0.12 (0.08)	-0.09 (0.11)	-	-0.45** (0.07)	0.03 (0.09)	0.01 (0.09)	-0.12 (0.18)	-0.70** (0.03)	0.09 (0.14)	-0.19 (0.07)
t_{fall}	-0.24 (0.11)	-0.11 (0.11)	0.35** (0.13)	0.69** (0.05)	-0.36** (0.09)	0.65** (0.06)	-0.45** (0.07)	-	-0.01 (0.11)	0.02 (0.11)	0.12 (0.19)	0.09 (0.12)	-0.16 (0.15)	-0.28 (0.07)
r_0	0.12 (0.08)	-0.01 (0.09)	-0.30** (0.09)	0.14 (0.08)	0.11 (0.09)	0.05 (0.08)	0.03 (0.08)	-0.01 (0.10)	-	0.99** (0.00)	0.06 (0.14)	-0.13 (0.08)	0.01 (0.14)	-0.02 (0.09)
r_{CSM}	0.03 (0.08)	0.02 (0.09)	-0.29 (0.09)	0.19 (0.08)	0.08 (0.09)	0.09 (0.08)	0.01 (0.09)	0.02 (0.11)	0.99** (0.00)	-	0.12 (0.14)	-0.13 (0.08)	0.02 (0.14)	-0.06 (0.09)
$\dot{M}$	-0.38** (0.17)	0.06 (0.16)	0.04 (0.16)	0.15 (0.15)	0.10 (0.16)	0.41** (0.10)	-0.12 (0.18)	0.12 (0.19)	0.06 (0.14)	0.12 (0.14)	-	-0.25 (0.25)	0.50** (0.12)	-0.35** (0.12)
v	-0.19 (0.08)	-0.08 (0.09)	-0.21 (0.12)	-0.04 (0.07)	-0.13 (0.08)	-0.30** (0.08)	-0.70** (0.03)	0.09 (0.12)	-0.13 (0.08)	-0.13 (0.08)	-0.25 (0.25)	-	-0.04 (0.11)	0.57** (0.09)
v_{CSM}	-0.06 (0.15)	-0.12 (0.11)	0.02 (0.11)	-0.07 (0.13)	0.09 (0.11)	0.02 (0.12)	0.09 (0.14)	-0.16 (0.15)	0.01 (0.13)	0.02 (0.14)	0.50** (0.12)	-0.04 (0.11)	-	0.03 (0.07)
v_{sh}	0.42** (0.07)	-0.23 (0.09)	-0.50** (0.10)	-0.20 (0.07)	0.17 (0.07)	-0.53** (0.07)	-0.19 (0.07)	-0.28 (0.07)	-0.02 (0.09)	-0.06 (0.09)	-0.35** (0.12)	0.57** (0.09)	0.03 (0.08)	-

Figure 13. The correlation matrix heatmap for our parameter pairs. Each cell is annotated with the PCC and in parentheses are the 1σ uncertainties on the PCC as calculated using our bootstrap method. If the correlation is at least moderately strong (i.e., with a PCC of above 0.3 or below -0.3) and also significant (with a p-value below 0.05), the PCC is highlighted with "**".

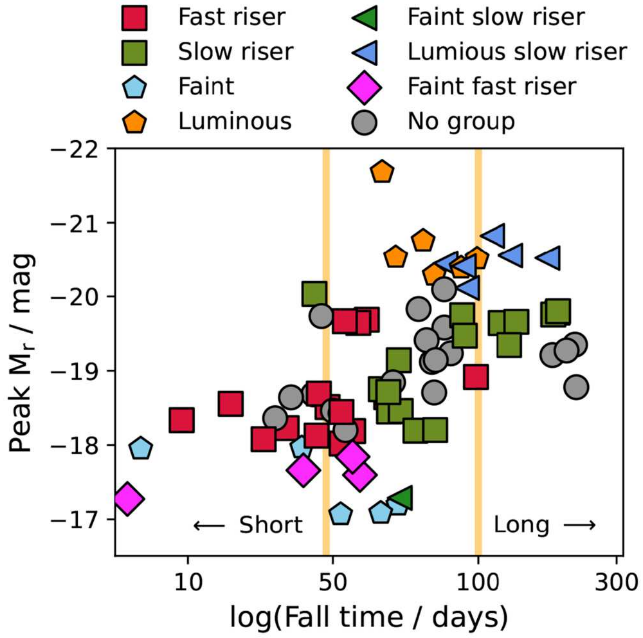

Figure 14. The peak r-band absolute magnitude against the r-band fall time. The photometric groupings are denoted by different markers. The boundaries between the long fall time and short fall time SNe IIn (which we define as over 100 days or under 30 days, respectively) are marked by vertical orange lines.

A. Nyholm et al. 2020). While famous literature examples were excluded from our analysis due to the Hα emission features from CSM–ejecta interaction dominating the r-band flux at later times, we can still probe for longer-lived transients in our sample. Typically, the photometric data extends a few hundred days post-discovery, so the late-time Hα effect is unimportant in these epochs (or the transients are relatively young). We define a long-lived SN as having a long fall time, in excess of 100 days (consistent with the slow decliners identified by A. Nyholm et al. 2020). In our sample, 22% of our events have a long fall time (of the subsample of 89, where the fall time can be measured). This fraction is somewhat higher than what is found by A. Nyholm et al. (2020), who found ∼15% of their sample had a fall time of 100 days or greater. This difference is likely due to the differences in measurement, where we measure the time taken to decline by 1 mag from peak brightness, rather than calculating the average decline rate over 50 days. We also note that our sample of measurable decline times (77) is larger than the sample (27) used in A. Nyholm et al. (2020).

An exemplar of this subclass in our sample is SN 2020jhs, which was collected from the YSE sample (J. Nordin et al. 2020a; A. Dahiwale & C. Fremling 2021b). SN 2020jhs had a peak $M_r = -19.8$ mag and a fall time of 188 days. This transient was also a slow riser, with a rise time of ∼71.7 days, and has a large inferred CSM mass of $\sim 10.1\,M_\odot$. This object exemplifies the slow evolution seen in these luminous, high CSM mass objects.

As mentioned, the rise and fall times are strongly correlated with the CSM mass, and the fall time is correlated with the peak r-band absolute magnitude. We note that there is a weaker (but statistically significant) correlation between the peak r-band absolute magnitude and CSM mass (PCC = −0.27). Therefore, while high CSM mass leads to slower photometric evolution, it does not necessitate luminous transients (as seen in the archetypes of this class, SN 1988Z and SN 2005ip, with absolute magnitudes of −17.6 mag in the B band and −17.4 mag, unfiltered, respectively. (R. A. Stathakis & E. M. Sadler 1991; N. Smith et al. 2009c, 2017). These long-lived SNe IIn also tend to have high mass-loss rates (with a median of $\sim 0.4\,M_\odot$ yr^{-1}). Similarly to the slow risers, the long fall time is due to the longer diffusion timescale allowed by the massive CSM.

Finally, we note that we are unable to define a fall time for our whole sample.[11] This is due to the baseline of the photometric data not always covering 100 days post-peak. This is particularly true for the younger transients in the ZTF BTS sample. While this may result in unknown long-lived SNe IIn being omitted from this work, it is unlikely to affect the strong correlations we have found, with 61% of the sample with r-band data having a measurable fall time.

5.4. Fainter Transients

Another photometric subclass that has been identified in the SN IIn population is a group of subluminous transients. Well-studied examples of this subgroup include the enigmatic SN 2008S, which peaked at $M_{\rm V} = -14.0$ mag (M. T. Botticella et al. 2009; S. M. Adams et al. 2016). These fainter transients overlap in brightness space with SN impostors, typically with absolute V-band magnitudes of −10 to −14 mag (e.g., S. D. Van Dyk et al. 2000; C. S. Kochanek et al. 2012; M. Aghakhanloo et al. 2023a) and may reach the brightness of "normal" SNe II, such as the pre-explosion brightening of SN 1961V at $M_V = -16.5$ mag (e.g., F. Zwicky 1964; S. E. Woosley & N. Smith 2022). We explicitly exclude confirmed or suspected SN impostors from our analysis, but we do note that some fainter SNe IIn are present in our sample. While SNe IIn are luminous compared to normal SNe II, we define a "faint" SN IIn as peaking below $M_r = -18$ mag, around a magnitude (i.e., at $\sim 1\sigma$) fainter than the median of our uncorrected absolute magnitude distribution.

Our faintest example, SN 2021aapa was discovered by ZTF (K. C. Chambers et al. 2021; K. Davis 2021) and has a peak r-band absolute magnitude of −16.9 mag, typical of the peaks of fainter SNe IIP. Around 15% of the (uncorrected for Malmquist bias) SNe IIn have a peak absolute r-band magnitude fainter than −18.0 mag. This fraction is consistent with A. Nyholm et al. (2020). These fainter transients tend to have a smaller CSM mass (e.g., SN 2021aapa has a CSM mass of $\sim 0.6\,M_\odot$) and are more likely to quickly decline. In the literature, these objects are sometimes associated with having photometric similarities with SNe IIP (a tentative plateau may be seen in SN 2021ras in our sample). These transients, such as SN 2011ht (M. Fraser et al. 2013; J. C. Mauerhan et al. 2013) and SN 2020pvb (N. Elias-Rosa et al. 2024), have two explanations accounting for the relatively weak explosions, IIn-like spectra, and associated precursor outbursts. First, a weaker explosion from a low-mass progenitor system (8–10 $M_\odot$) as a product of an ecSN, with the precursor being a product of unstable burning ejecting some of the stellar envelope (e.g., L. Dessart et al. 2010; T. Matsumoto & B. D. Metzger 2022). However, we note that the only ecSN candidate to date, SN 2018zd, does not exhibit prolonged interaction signatures (D. Hiramatsu et al. 2021). Second, that the progenitor is indeed massive (N. Elias-Rosa et al. 2024, put a progenitor detection constraint on SN 2020pvb of $\lesssim 50\,M_\odot$), where the explosion is weakened due to the formation of a black hole, with material falling back (J. Sollerman et al. 1998; A. Heger et al. 2003). It should be noted that our models do not inform on either scenario here. Indeed, in the fallback scenario, it is unknown how much mass is "missing" from the ejecta due to the black hole formation (limits could likely be placed if there were a progenitor detection, however).

5.5. Bright Transients

On average, SNe IIn are intrinsically luminous compared to other classes of CCSNe due to the efficient conversion of kinetic energy into radiation in the shock interaction (M. Kiewe et al. 2012). Furthermore, there are many examples of superluminous (peaking brighter than −20 mag) SNe IIn in the literature, such as SN 2015da, ASASSN-15ua, and ASASSN-14il (D. Dickinson et al. 2024; N. Dukiya et al. 2024; N. Smith et al. 2024). The most luminous SN IIn in our sample is SN 2020vci, which peaked at −21.7 mag in the r band (J. Tonry et al. 2020a; A. Dahiwale & C. Fremling 2021c). While this transient does not have a high CSM mass, with $\sim 0.4\,M_\odot$, it has a high ejecta mass over $\sim 30\,M_\odot$ and also a high ejecta velocity, with $v_{\rm ej} \approx 1.3 \times 10^4$ km s^{-1}. Within our sample, around 17% have a peak absolute magnitude brighter than −20 mag in the r band, suggesting that intrinsically very luminous transients are relatively common among SNe IIn. This subpopulation has a somewhat heterogeneous set of parameters inferred from `MOSFiT`, but has a high mass-loss rate (when this can be measured) with a median average mass-loss rate of $\sim 1\,M_\odot$ yr^{-1}.

5.6. Other Exotic SNe IIn

As large-scale transient surveys discover more SNe IIn, it has become apparent that not all of these transients smoothly decline after initial peak (including bumpy declines and dramatic rebrightenings (e.g., SN 2010mc, iPTF13z, SN 2014C, SN 2019zrk, and SN 2021qqp) (E. O. Ofek et al. 2014b; A. Nyholm et al. 2017; R. Margutti et al. 2017; C. Fransson et al. 2022; D. Hiramatsu et al. 2024b). Some SNe exhibit dramatic rebrightenings, forming a secondary peak. For example, SN 2021qqp (for a thorough study of this object, see D. Hiramatsu et al. 2024b). This luminous SN IIn, peaking at an r-band magnitude of −19.5 mag has a slow initial rise to peak. The slow rise lasted for ∼300 days, followed by a 60 days period of brightening, ending in a rapid rise to peak in the few days prior to maximum brightness. This extreme behavior was linked to dramatic mass-loss episodes in the few years preceding the explosion, with mass-loss rates of up to $10\,M_\odot$ yr^{-1} resulting in the ejecta colliding with dense, massive detached CSM shells. There was also a long-lasting precursor event with a peak $M_g = -15.6$ mag. Using models adopted from T. Matsumoto & B. D. Metzger (2022), it was found that the progenitor suffered

---

[11] However, we do extend our models in these cases to form a silver sample, which is presented in Appendix E.

two distinct mass-loss events, producing 2–4 $M_\odot$ of CSM, occurring 0.8 and 2 yr prior to the terminal explosion. In our sample, three transients were identified as having precursor activity: SN 2021yaz, SN 2021ydc, and SN 2022prr. A more thorough analysis of the ZTF data, however, may reveal more precursors (e.g., N. L. Strotjohann et al. 2021). Furthermore, some SNe IIn in the literature show precursor events that are classified as SN impostors (e.g., SN 2009ip) (J. C. Mauerhan et al. 2013). SN 2021qqp was also identified in our initial sample selection but was omitted from this work due to the double peak and the long precursor occurring directly prior to the SN explosion.

As our models do not incorporate bumps, secondary peaks, or rebrightenings, we exclude these objects from our analysis. Regardless, these striking objects are an important feature in the SN IIn landscape, informing on the mass-loss history of the progenitor in the years prior to the terminal explosion. While we do not include these objects in our analysis, we present these objects in our full table of SN IIn (which includes cut objects) in the online materials.

6. Inferred Mass-loss Rates of Progenitor Systems

Here, we explore the pre-SN mass loss as inferred from a combination of `MOSFiT` and observational features. The mass-loss rate of the progenitor before the terminal SN explosion is key to the determination of the progenitor type. In this section, we compare our mass-loss rate estimates with the indicative mass-loss rate/CSM velocities of various progenitor types (as summarized by N. Smith 2017).

Progenitor mass loss may occur through massive winds, eruptions, binary interactions, or a combination of these effects. The typical mass-loss rates from the stellar winds of evolved stars such as RSGs may be insufficient to strip enough mass off a progenitor star to produce the CSM we infer for SNe IIn, with mass-loss rates of $\sim 10^{-6}\, M_\odot\, \mathrm{yr}^{-1}$ (E. R. Beasor et al. 2020). In contrast, LBVs have high line-driven wind velocities reaching a few 10^2–$10^3\, \mathrm{km\, s}^{-1}$, producing mass-loss rates of 10^{-5}–$10^{-4}\, M_\odot\, \mathrm{yr}^{-1}$ (J. S. Vink & A. de Koter 2002; N. Smith et al. 2004); this may *still* be too weak to be the sole mass-loss mechanism for SNe IIn. As previously discussed, LBVs are also known to undergo great eruptions with observed ejecta velocities ranging from 10^2 to $10^3\, \mathrm{km\, s}^{-1}$, which may be due to some eruptive outburst or extreme, optically thick continuum-driven winds (e.g., N. Smith et al. 2004; A. Kashi & N. Soker 2010). These great eruptions are distinct from the winds in that they have a mass-loss rate in excess of $1\, M_\odot\, \mathrm{yr}^{-1}$ (R. M. Humphreys & K. Davidson 1994; D. J. Hillier et al. 2001; N. Smith et al. 2003) which may be triggered by an interaction with a companion (A. Kashi & N. Soker 2010). While the great eruptions may result in short periods of extreme mass loss (it should be noted that less extreme episodic eruptions can lead to more modest amounts of CSM; for example P Cygni has $\sim 0.1\, M_\odot$) (N. Smith & P. Hartigan 2006), it has been argued that eruptions in single massive stars cannot account for the tens of solar masses of CSM found around some SNe IIn. Instead, binary interactions may be critical (e.g., in the cases of η Car and SN 2015da) (A. Kashi & N. Soker 2010; N. Smith et al. 2024). These "binary interactions" arise from diverse scenarios, ranging from mergers in a common envelope to collisions and mergers with compact objects (e.g., N. Soker & R. Tylenda 2006; N. Langer 2012; N. Smith et al. 2018; S. L. Schrøder et al. 2020).

Table 4
The Telescopes, Instruments, and Number of Spectra Available for Our SNe IIn for CSM Velocity Estimation

Telescope	Instrument	No. of Spectra
LT	SPRAT	16
Palomar 200 inch	DBSP	13
NTT	EFOSC2	10
Keck1	LRIS	8
MMT	MMT Blue	5
Lick 3 m	KAST	4
UH 88	SNIFS	4
WHT	ISIS	3
APO 3.6 m	DIS	2
Magellan	IMACS	2
MMT	Hectospec	2
MMT	Binospec	1
Keck2	DEIMOS	1
INT	IDS	1
NOT	ALFOSC2	1
Gemini North	GMOS	1
Lijiang 2.4 m	YFOSC	1
ANU 2.3 m	WiFeS	1

Here, we describe our process for estimating the CSM velocity for our sample of SNe IIn in order to estimate the progenitor mass-loss rates. Although CSM velocities of $100\, \mathrm{km\, s}^{-1}$ are often assumed (e.g., T. J. Moriya et al. 2013, 2023), the mass-loss rate is highly sensitive to this velocity. Therefore, we infer the wind velocity using the narrow component of the Hα complex. By definition, our sample has at least a classification spectrum publicly available per transient, allowing such a measurement. We collect the available spectra from WISeREP[12] and YSE-PZ (D. A. Coulter et al. 2023), with the addition of a small amount of private data from C. L. Ransome et al. (2021) and the PS1 Medium Deep Survey. These data were produced by numerous instruments; the various instruments and respective telescopes are outlined in Table 4.

The CSM velocities are estimated by decomposing the Hα profiles into Gaussian components following the procedure from C. L. Ransome et al. (2021). Because each spectral line is effectively broadened by the instrumental response (i.e., the resolution), we deconvolve the instrumental width from the observed width. In order to estimate the instrumental broadening, we measure the width of lines (sky or host galaxy lines) that we do not expect to be broadened by some other mechanism. The degree of data reduction in each spectrum differs. As such, host or sky lines are not available in every instance, and, typically, the resolution or grating used is not known. We assume a constant instrumental broadening for each spectrograph based on the available measured sky or host lines. We do note, however, that the spectrograph configuration is not known for each spectrum, and the resolution of some instruments can vary significantly; for example, the R power of DBSP ranges from 10 to 10,000. Therefore, our CSM velocity estimates may be considered upper limits. Finally, we note that the CSM may be radiatively accelerated and therefore an overestimate of the CSM velocity (e.g., D. Tsuna et al. 2023). We are able to estimate the CSM velocities of 57 of our SNe IIn. Additionally, we measure the unresolved upper limits,

---

[12] https://www.wiserep.org

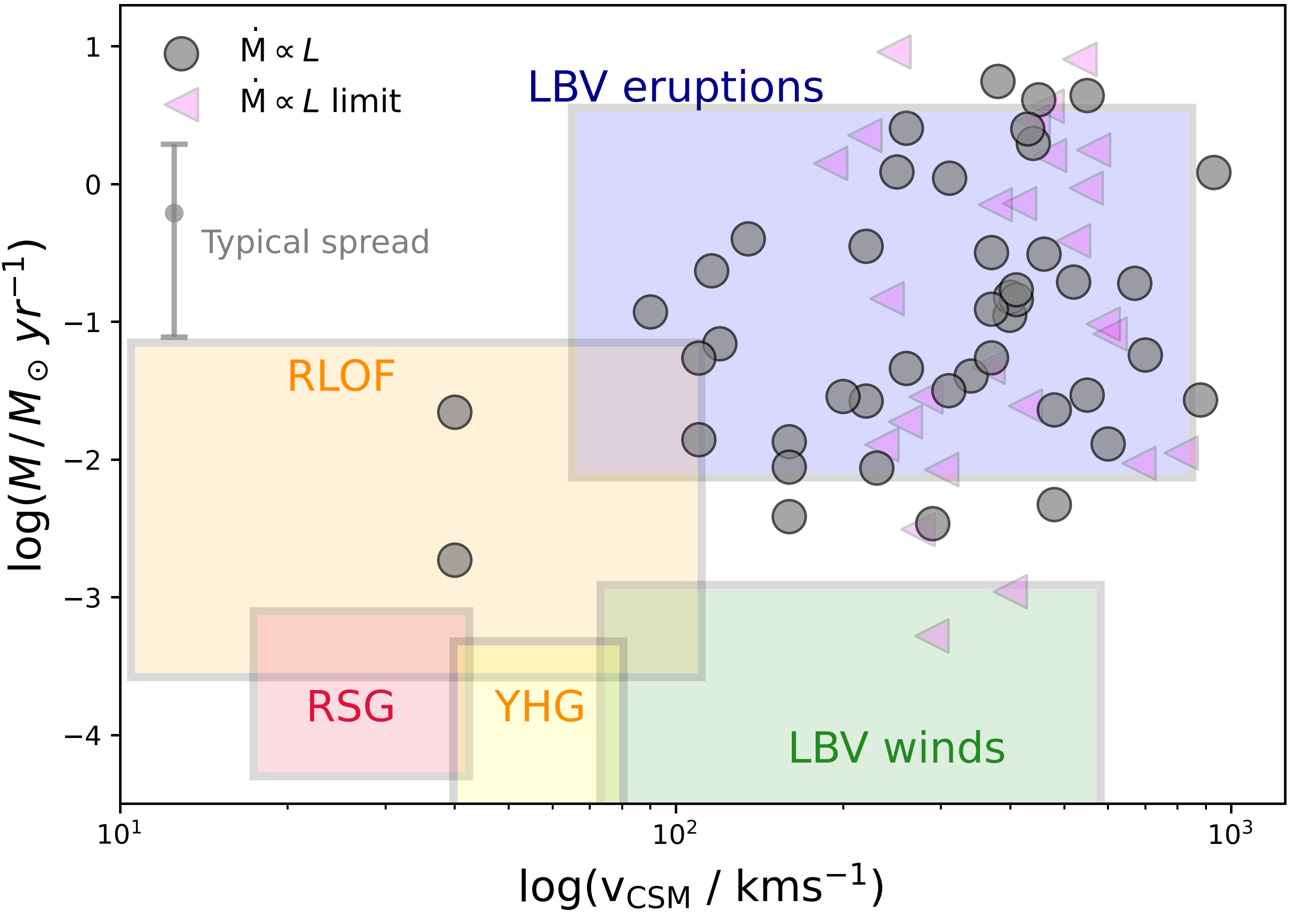

Figure 15. The mass-loss rate distributions of our SNe IIn. The shading corresponds to the indicative parameter space corresponding to different mass-loss regimes, against the CSM velocity expected for each mode (reproduced using C. de Jager et al. 1988; J. T. van Loon et al. 2005; R. M. Drout 2016; N. Smith 2017). The blue rectangle is indicative of the high mass-loss rates seen in the great eruptions of LBVs, spanning from 10^{-2} to 10^0 $M_\odot$ yr^{-1}. The green region shows the lower mass-loss rates seen from LBV winds. The orange region represents mass loss from RLOF, but not including more violent binary events. The red region depicts the mass-loss rates from extreme RSGs, and the yellow region shows the mass-loss rates expected from yellow hypergiants (YHGs). Also shown is the typical mass-loss rate spread of our sample. The large scatter of a few 0.1 dex is likely due to the sensitivity of the mass-loss rate to the shock velocity.

where the emission line is not resolved given our assumed instrumental responses; we have limits for 27 SNe IIn.

We use the measured velocities to estimate the mass-loss rate for each event. We use the mass-loss rate proportional to the luminosity (Equation (4)) (e.g., N. Smith 2017; D. Dickinson et al. 2024). Our mass-loss rate estimates are therefore dependent on the luminosity, the CSM velocity, and the shock velocity (which in turn is dependent on our parameters from `MOSFiT`).

We plot the mass-loss rates against the CSM velocity in Figure 15, along with the general regions in the phase space representing different mass-loss modes (N. Smith 2017). The mass-loss rate distribution is shown in Figure 15 for comparison between the mass-loss modes. Also shown are the limits using the widths of the narrow components that could not be deconvolved from their instrumental response due to being too narrow to be resolved using the assumed instrumental response. These upper limits on the CSM velocity are roughly consistent with our sample of SNe that have a CSM velocity measurement. This consistency may suggest that we are underestimating the instrumental response in some cases (as typically these spectra are not so high resolution, such that the FWHMs are almost unaffected after deconvolution), leading to an overestimate in mass-loss rate. Our median (and spread) for the mass-loss rate is $\log(\dot{M}/M_\odot\ \mathrm{yr}^{-1}) = -1.06^{+0.81}_{-1.15}$.

We now highlight just the one-dimensional mass-loss rate distribution in Figure 16. Our inferred mass-loss rates span from $\approx 10^{-3}$ to 10^0 $M_\odot$ yr^{-1}, with a peak at $\sim 10^{-2}$ $M_\odot$ yr^{-1}. We note that, as the mass-loss rates are proportional to the luminosity, the distribution may be skewed toward higher mass-loss rates due to using the peak luminosity (i.e., the highest mass-loss rate assuming the shock and CSM velocities are constant). The mass-loss evolution may be probed over time, but having a spectral time series would be more informative for such a calculation. Our mass-loss rate distribution is mostly consistent with the mass-loss rates expected to result from the great eruptions of LBVs. However, four of our SNe IIn have CSM velocities and mass-loss rates consistent with mass-loss due to RLOF (with two of these overlapping). None of our samples are consistent with the mass-loss from LBV winds (P. Cox et al. 1995; D. J. Hillier et al. 2001; F. Najarro 2001; J. Puls et al. 2008).

7. Host Galaxies of Our SNe IIn

Core-collapse SNe generally trace star formation in their hosts. As such, they are often found in spiral-like galaxies. While we do not study the hosts of our sample in detail, we now briefly discuss the Hubble types of our sample.

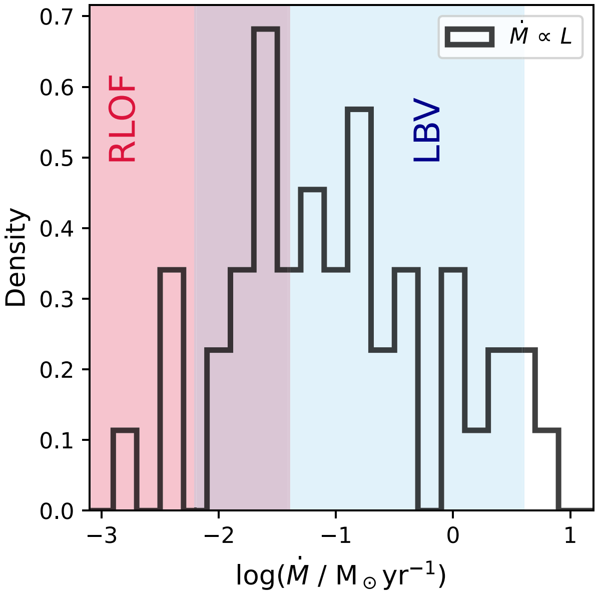

Figure 16. Histogram showing the mass-loss rate distribution of our sample of SNe IIn. The solid line shows the mass-loss rate proportional to the peak luminosity. The red shaded region is the mass-loss regime of binary interactions via RLOF, and the blue shaded region is the mass-loss rate region of LBV eruptions. In this single dimension, the mass-loss rate of our SNe IIn is consistent with both RLOF and the great eruptions of LBVs, with some overlap between these two regions.

Environmental studies have measured the association of SN locations with star formation or stellar population ages using either narrowband photometry or spectroscopy (S. M. Habergham et al. 2014; F. Taddia et al. 2015; L. Galbany et al. 2018; C. L. Ransome et al. 2022; T. J. Moriya et al. 2023). As previously mentioned, SNe IIn seem to inhabit a diverse set of environments, seemingly not being consistent with single massive stars. In Table 6, we present our sample of SNe IIn. In this table, we record the host galaxies of our transients, with this information being gathered from NED (G. Helou & B. Madore 1988) and SIMBAD (M. Wenger et al. 2000). All but two of the SNe in a classified host are from some class of spiral galaxy, as is the expectation for a CCSN, with one irregular and one elliptical host. In the case of an elliptical host, one may expect a thermonuclear SN. For SNe IIn, this possibly suggests SNe Ia CSM, e.g., SN 2002ic (M. Hamuy et al. 2003), SN 2005gj (J. Prieto et al. 2005), SN 2008J (F. Taddia et al. 2012), and SN 2012ca) (O. D. Fox et al. 2015; C. Inserra et al. 2016).

For a massive progenitor, it would be expected that its host galaxy would be an actively star-forming spiral galaxy. However, after a host galaxy search using SIMBAD, we find that two of the hosts in our sample of SNe IIn are elliptical galaxies. Elliptical galaxies, sometimes referred to as “red and dead” galaxies, have lost much of their gas over their evolution and are typically not expected to harbor massive stars due to a lack of active star formation. However, we have apparent elliptical hosts in our sample. In our sample, one SN IIn was found in an apparent elliptical host, SN 2019bxq in the host 2MASX J16575851+7836144. This transient has a total mass of $\sim$28 $M_\odot$, which may preclude a thermonuclear SN.

If the progenitor of this SN IIn is indeed massive, then it is possible that the host has underlying star formation. I. Irani et al. (2022) present CCSNe from ZTF BTS with elliptical hosts. Those authors add three CCSNe from ZTF BTS (one SN Ic and two SNe II) to seven CCSNe with elliptical hosts from the literature. Based on the spectroscopically complete sample of ZTF BTS, it is found that elliptical galaxies comprise $\sim$0.3% of CCSN hosts in the local universe. Those authors also find that CCSNe are more offset from the core of the elliptical hosts than SNe Ia that have elliptical hosts. Those authors conclude that there may be low surface brightness residual spiral features hosting some star formation, or there is star formation encouraged via the introduction of material from flows from the intergalactic medium (see also M. Fukugita et al. 2004; T. M. Sedgwick et al. 2021). Therefore, there may be limited star-forming activity in some elliptical hosts, possibly producing massive stars.

A large sample, detailed host study of these SNe IIn hosts would be complementary to our results and is the topic of future work. Measuring the properties of the local environments and linking these data with the physical and observed SN parameters from this work may further establish correlations and progenitor routes in lieu of direct progenitor detections.

8. The Progenitors of SNe IIn

We have modeled 142 SNe IIn using `MOSFiT`. As seen in smaller sample studies (e.g., M. Kiewe et al. 2012; F. Taddia et al. 2013; A. Nyholm et al. 2020), the overall population is diverse and forms a continuum of observed and derived parameters. Typically, the SNe IIn in our sample have a dense inner CSM, $\sim 10^{-12}$ g cm^{-3}, with a CSM density profile that is somewhat flat ($s \sim 1.4$). We infer that the progenitors generally lose a few solar masses of mass that forms the immediate CSM shell in the decades/centuries preceding the SN explosion (given the 1+ yr duration of interaction for most SNe IIn. The progenitors are inferred to be typically massive; the summed CSM and ejecta masses are $\sim$24 $M_\odot$. Although we again note that this is a lower limit on the progenitor mass (excluding the remnant).

We do not find any clustering in the parameter pairs that could have more clearly pointed to distinct progenitor channels. In posterior distributions of the individual parameters, we only find one example of a population that has multiple components. We find two populations in the fall time distribution, with a long fall time component (centered at around 200 days) as determined by a GMM. These long fall time SNe IIn have higher CSM masses on average as inferred by `MOSFiT`, and likely arise from more massive progenitor systems. We also find that there is an apparent high CSM tail within the sample (however, not a separate population). This population extends to a few thousand astronomical units and is associated with less dense CSM profiles (a few 10^{-14} g cm^{-3}). However, this apparent population is due to multiple solutions for ρ_0 being found for individual objects. Therefore, one should not necessarily consider this a true distinct population.

In addition to the clusters in singular parameters, we also find correlations in the observed light-curve features. We find that the rise time and fall time correlate with the inferred CSM mass. These correlations suggest that longer-lived, slower evolving SNe IIn have more CSM and that slower rising SNe IIn tend to be slower falling and vice versa. This is to be expected due to the dependency of the diffusion time on the CSM mass in our models. We also find that the slower decliners tend to be intrinsically brighter in the r band, similar to the findings of A. Nyholm et al. (2020). The mass-loss rates also correlate with the CSM mass, the fall time, *s,* and the peak *r*-band absolute magnitude. This suggests that the SNe IIn with high mass-loss rates tend to be intrinsically brighter. They also have a more eruptive/outburst-like mass-loss history, producing a massive CSM. These SNe IIn then evolve slowly from peak brightness.

The canonical picture of SN IIn progenitors is that they are LBVs, with pre-explosion detections and precursor emission being interpreted as LBV great eruptions. Pre-explosion, progenitor direct imaging is one "smoking gun" clue, although extremely limited. There are (at the time of writing) six SNe IIn with claimed direct progenitor detections: SN 1961V (LBV) (R. W. Goodrich et al. 1989; A. V. Filippenko et al. 1995; N. Smith et al. 2011); SN 2005gl (LBV-like) (A. Gal-Yam et al. 2007; A. Gal-Yam & D. C. Leonard 2009); SN 2009ip (possible LBV) (N. Smith et al. 2010; R. J. Foley et al. 2011; J. C. Mauerhan et al. 2013); SN 2010jl (possible LBV) (N. Smith et al. 2011; E. Dwek et al. 2017; O. D. Fox et al. 2017; Z. Niu et al. 2024); SN 2015bh (LBV) (C. Thoene et al. 2015; N. Elias-Rosa et al. 2016) and SN 2016jbu (LBV or YHG) (C. D. Kilpatrick et al. 2018; S. J. Brennan et al. 2022, respectively).

In this work, we put constraints on the CSM mass and the ejecta mass (therefore, the total pre-explosion mass). We also estimate the average mass-loss rates of the progenitors. We find that the CSM typically holds a few solar masses of material (but can be in excess of $10\,M_\odot$). Furthermore, the progenitors lose mass at a rate of $\sim$0.01–0.1 $M_\odot\,\mathrm{yr}^{-1}$ but can be in excess of $1\,M_\odot\,\mathrm{yr}^{-1}$. In lieu of our "smoking gun" progenitor detections, we can make inferences on the progenitor channel using these parameters. The massive CSM and generally massive progenitors, along with the high mass-loss rates we find, all suggest LBV progenitors. Indeed, this reasoning is employed in the literature. The high CSM mass, precursor events, and bumps in the light curve are likely formed by some LBV great eruption event(s), with some notable examples being SN 2006tf, SN 2011fh, SN 2015da, and SN 2021qqp (N. Smith et al. 2008; T. Pessi et al. 2022; D. Hiramatsu et al. 2024b; N. Smith et al. 2024). One SN IIn with a very high mass-loss rate is SN 2006tf, which had lost $20\,M_\odot$ of mass in the few decades leading up to the SN explosion (N. Smith et al. 2008). Furthermore, SN 2015da was also found to have a high mass-loss rate (up to $0.6\,M_\odot\,\mathrm{yr}^{-1}$) and large CSM mass ($\sim$$20\,M_\odot$) (L. Tartaglia et al. 2020; N. Smith et al. 2024). Furthermore, the precursor activity and dramatic secondary peak of SN 2021qqp allude to extreme mass-loss episodes consistent with an LBV progenitor (D. Hiramatsu et al. 2024b). This reasoning is reflected in SN impostors (which may precede true SNe) where these events are also consistent with LBV great eruptions, with examples being: SN 1954J (R. M. Humphreys & K. Davidson 1994; R. M. Humphreys et al. 2017); SN 2000ch (which periodically explodes, perhaps due to binary interactions) (N. Smith 2011; M. Aghakhanloo et al. 2023b); SN 2002 kg (K. Weis & D. J. Bomans 2005; J. R. Maund et al. 2006; R. M. Humphreys et al. 2017); SN 2003gm (C. S. Kochanek et al. 2012) and AT 2016blu (periodic and similar to SN 2000ch) (M. Aghakhanloo et al. 2023a).

From Figure 15, it is apparent that the majority of our SNe IIn have CSM velocities and corresponding mass-loss rates that are largely consistent with LBV eruptions. This conclusion is supported by the fact that we find the median CSM profile density parameter $s \simeq 1.4$, i.e., a more eruptive-like CSM profile in general. We do note that while we may overestimate the CSM velocity, even if we assume a modest value of $100\,\mathrm{km\,s^{-1}}$, $\sim$75% of our SNe IIn would still have mass-loss rates consistent with an LBV great eruption. We do note that a small proportion of our SNe IIn do have mass-loss rates more consistent with RLOF, so we also cannot rule out an extreme mass loss proposed for some RSGs.

However, we note that in the literature, there are some SNe IIn with inferred mass-loss rates inconsistent with LBV eruptions. For example, SN 1988Z, the aforementioned prototypical long-lived SN IIn, has been suggested to have a clumpy wind-like CSM, with a CSM geometry inconsistent with eruptions (N. N. Chugai & I. J. Danziger 1994). One transient that is presented as representing a possible continuum of mass loss and SN IIn progenitors is PTF 11iqb. This object exhibited weaker CSM interaction a earlier times (flash ionization) (D. Khazov et al. 2016; W. V. Jacobson-Galán et al. 2022) and stronger interaction at later times—possibly due to interaction with a more distant ring of CSM from more modest mass-loss rates of $\sim$$10^{-4}\,M_\odot\,\mathrm{yr}^{-1}$ (N. Smith et al. 2015). Those authors draw comparisons to the similar SN IIn, SN 1998S (A. Fassia et al. 2001; J. Mauerhan & N. Smith 2012). Those authors suggest that wind-like mass loss, perhaps coupled with a binary system shaping the CSM, may account for some of these weaker interacting SNe IIn (forming a continuum between SNe IIn and SNe IIP/L) (N. Smith et al. 2009b; M. Stritzinger et al. 2012; I. Shivvers et al. 2015). These lower mass-loss rate objects are a seemingly rare exception to the SN IIn landscape. Indeed, in our sample, $\sim$5% of the SNe IIn have mass-loss rates of $\sim$$10^{-4}\,M_\odot\,\mathrm{yr}^{-1}$ and have a more wind-like CSM geometry.

The discussion around progenitor routes is often centered around the initial mass of the progenitors, as this dictates the evolutionary path. Indeed, the majority of the literature SN IIn and SN impostor examples we have discussed in this section are claimed to be massive LBVs. Without pre-explosion data, the best estimate we have in this work of the progenitor mass is the "total mass" (i.e., the ejecta mass added to the CSM mass). This traces the mass of the progenitor in the few decades to hundreds of years prior to the terminal explosion. Most events in our sample have a large total mass (the sum of the ejecta and the CSM masses) with $M_{\mathrm{tot}} \simeq 24\,M_\odot$. Hence, our SN IIn sample is largely consistent with massive progenitors (e.g., LBVs, or massive RSGs). The total mass distribution is shown in the lower left panel of Figure 7. This distribution is skewed to larger total masses, covering a range of total masses from a few to over $50\,M_\odot$. We do note that the ejecta masses are not as well constrained as the CSM masses and the total mass traces our ejecta mass estimates, so the spread in the distribution of total masses is large.

In the literature, we see a range of total masses for SNe IIn: from progenitors that may be heavily stripped to the very massive. One example of a possibly highly stripped progenitor in the literature is SN 1988Z, with subsolar ejecta mass (however, such a degree of mass stripping may require binary mass loss) (N. N. Chugai & I. J. Danziger 1994). This SN may be an example of a quenched interaction SN IIn where $M_{\mathrm{ej}} \ll M_{\mathrm{CSM}}$ (L. Dessart 2024). In contrast, massive LBVs have been proposed as the progenitors for a number of SNe IIn (e.g., SN 2005gl, SN 2010jl, and SN 2015da) (A. Gal-Yam et al. 2007; A. Gal-Yam & D. C. Leonard 2009;

E. O. Ofek et al. 2014c; N. Smith et al. 2024), with masses reaching 50 $M_{\odot}$, and our findings are generally consistent with these objects. However, extreme mass loss from RSGs (particularly massive RSGs) cannot be ruled out as creating a progenitor path, with VY CMa reaching high mass-loss rates and could result in SNe IIn (e.g., A. Heger et al. 1997; J. T. van Loon et al. 2005; N. Smith et al. 2009b; S.-C. Yoon & M. Cantiello 2010; S. R. Goldman et al. 2017; M. Yang et al. 2023). Moreover, these extreme RSGs may evolve blueward as they approach their death, as has been observed with WOH G64, which was observed to have transitioned from an RSG to a YHG, and also has a complex circumstellar environment (G. Munoz-Sanchez et al. 2024; K. Ohnaka et al. 2024). Another exotic possibility is that of the pair instability SNe (PISNe), which arise from very massive stars (M_{*} 100 $M_{\odot}$) where the high pressure and temperature at the stellar core promote the creation of electron-positron pairs. This process lifts radiation pressure and collapses the core. Pulsational PISNe are thought to shed tens of solar masses prior to collapse and would likely explode as SNe IIn and have been offered as explanations for the impostor outbursts of SN 2009ip-like objects, and there may be an example in (the albeit H-poor) SN 2020acct (S. E. Woosley et al. 2007; A. Pastorello et al. 2013; S. E. Woosley 2017; C. R. Angus et al. 2024).

Finally, we note again that we cannot rule out an extended mass-loss history due to more distant, diffuse CSM not being dense enough for any interaction features to be observable. Sustained spectroscopic follow-up and extension to the IR or radio probes the CSM and a more accurate interaction duration (e.g., O. D. Fox et al. 2011; A. L. Ibik et al. 2025). Hence, these total masses should be treated as a lower limit on the initial mass of the progenitor.

We have shown that the physical parameters from `MOSFiT`, paired with observational parameters, for most of our sample are consistent with LBV-like progenitors. There is, however, still tension with other lines of investigation. Chiefly, the environments of SNe IIn are inconsistent with the progenitors being single massive stars (with some SNe IIn being apparently unassociated with ongoing star formation) (S. M. Habergham et al. 2014; L. Galbany et al. 2018; C. L. Ransome et al. 2022). Identified LBVs in nearby galaxies (the Small and Large Magellanic Clouds and M 33) seem well associated with ongoing star formation (T. Kangas et al. 2017). Some of this discrepancy may be explained by considering that some massive stars may be in low surface brightness H II regions. It has also been suggested that LBVs may also form as the product of mergers and mass accretion in binary systems with lower-mass stars (P. Podsiadlowski et al. 1992; S. Justham et al. 2014; N. Smith & R. Tombleson 2015), which may be corroborated when considering the extremely isolated SN 2009ip (N. Smith 2011; A. Kashi et al. 2013; J. C. Mauerhan et al. 2013; N. Soker & A. Kashi 2013). We do not perform a detailed environmental analysis in this work, but we do note that almost all of the SNe in our sample with a classified host (many SN IIn hosts are low surface brightness/dwarf galaxies) (e.g., C. L. Ransome et al. 2022) are in actively star-forming galaxies. A detailed analysis of the local environments of our SNe IIn is a topic of future work.

Recently, there has been growing evidence that at least some LBVs, and the great eruptions associated with them, may be the product of binary interaction (A. Kashi & N. Soker 2010; N. Smith 2011; A. Kashi et al. 2013; N. Soker & A. Kashi 2013; M. Aghakhanloo et al. 2023a, 2023b). If this is the case for at least a subset of LBV-like progenitors, this may alleviate some of the tension with the aforementioned environmental inconsistencies, as the progenitor mass may be lower in the case of some merger event (S. M. Habergham et al. 2014; L. Galbany et al. 2018; C. L. Ransome et al. 2022). As our sample is consistent with LBV progenitors, we now briefly discuss the evidence for LBVs in binaries. Observationally, the CSM geometry around SNe IIn is inferred to be often asymmetric. Such asymmetry may be revealed via the analysis of the Hα profiles or measurements from polarimetry. C. Bilinski et al. (2024) present multi-epoch spectropolarimetric observations for a sample of 14 SNe IIn. Those authors find that at peak optical light, there is an intrinsic polarization for most of their SNe IIn sample. This polarization level reached as high as 6% in the case of SN 2017hcc—the highest level of polarization seen in any SN. Those authors also note that their results suggest that SNe IIn are the most strongly polarized of any SN class. C. Bilinski et al. (2024) conclude that for such persistent asymmetric CSM profiles to be present, eruptive mass loss into spherical shells is unlikely. Rather, mass loss due to binary interaction or eruptive mass loss that is in some way enhanced in an equatorial torus is favored. S. J. Brennan et al. (2022) also argue that their models of the progenitor of SN 2016jbu are consistent with a massive binary system.

As previously discussed, the mass-loss rates from steady line-driven winds are insufficient to be the sole mass-loss mechanism for SNe IIn. The large CSM masses around some SNe IIn require extreme mass-loss rates, which we see in our sample but are also seen in the literature (e.g., ASASSN-14il, SN 2015da, ASASSN-15ua) (N. Dukiya et al. 2024; D. Dickinson et al. 2024; N. Smith et al. 2024). When considering the asymmetry seen in the CSM, it has been suggested that the high mass-loss rates may require violent interactions within a binary. Mass loss (and perhaps the SN itself) in binary systems may manifest from mechanisms such as: violent mass transfer events aside from normal Roche-lobe overflow (RLOF); mergers of massive stars; mergers of mass stars with a compact object; common envelope interactions or collisions (N. Soker & R. Tylenda 2006; R. A. Chevalier 2012; N. Smith & W. D. Arnett 2014; S. L. Schrøder et al. 2020; T. Matsuoka & R. Sawada 2024; A. Ercolino et al. 2024; F. R. N. Schneider et al. 2024). The semi-periodic eruptive episodes seen in SN impostors (with likely LBV progenitors) or other massive outbursts have also been linked to binary interactions (A. Kashi & N. Soker 2010; N. Smith 2011; N. Soker & A. Kashi 2013; M. Aghakhanloo et al. 2023a, 2023b). Indeed, a Galactic analog is the aforementioned η Car, which has at least one companion and is entombed in the highly asymmetric Homunculus nebula (with the 19th century Great Eruption possibly being some merger event) (N. Smith et al. 2003, 2010; A. Kashi & N. Soker 2010; N. Smith 2011). These observational clues lead to the argument that, as well as the continuum-driven (or other mechanisms) eruptions in LBVs, violent binary interactions may be key to understanding the mass loss around SN IIn progenitors.

We note that even with binary interactions, an LBV progenitor may still be required (given the observed progenitors and observed LBV outbursts). We do note that our models cannot inform on the mass-loss mechanisms outside of the mass-loss rate estimates. Nonetheless, these are important considerations in the discussion of SN IIn progenitors (indeed, most massive stars, and LBVs, in particular, are in binaries) (e.g., H. Sana et al. 2012; L. Mahy et al. 2022). The more extreme, massive RSGs may also suffer mass loss in binary systems, producing SNe IIn. We do, however, caution that the regions shown in Figure 15 are indicative based on empirical measurements. With more theoretical work, an additional illustrative region may be added for LBVs suffering violent binary interactions (or the great eruption region may be split into single star/binaries, as there are likely degeneracies or overlap). Specifically, models that can reproduce a CSM forming rapidly and/or episodically would help solidify our understanding of these systems. Observationally, the binary scenario for individual objects could be confirmed with late-time imaging that reveals a surviving companion.

Furthermore, in Figure 10, we show the radiated energy distribution of our SNe IIn. Our GMM analysis indicates no evidence of a statistically significant multimodal distribution. This differs from D. Hiramatsu et al. (2024a), who found a bimodal distribution in the radiated energies in their SN IIn sample. We do note, however, that there are tentative, apparent peaks in the distribution at $\sim 10^{49.6}$ and $\sim 10^{50.4}$ erg. As mentioned by D. Hiramatsu et al. (2024a), these radiated energy populations may indicate different explosion energy groups and therefore separate populations in the progenitor paths, given assumptions on the energy conversion factor, ϵ. The lower energy population may therefore be the proposed lower-mass progenitors such as RSGs and super-AGB stars (e.g., N. Smith et al. 2009b; N. Smith 2013; T. J. Moriya et al. 2014). The higher energy population may be comprised of the more massive progenitors, which are more consistent with our (albeit incomplete for our sample) mass-loss rate estimates. Alternatively, some of these SNe may be weakened via black hole formation (J. Sollerman et al. 1998). In order to better understand any possible multimodality, we require more observations and larger sample sizes.

To summarize this discussion, the typical set of parameters from `MOSFiT` and other measured observational quantities from the photometry indicates that most of our progenitors are consistent with LBV progenitors. We do, however, note that our measured CSM velocities may be upper limits and overestimate the mass-loss rates. Typically, our mass-loss rates and CSM velocities are too high to be attributed to line-driven winds and RLOF mass loss in binaries. However, there is observational evidence (e.g., C. Bilinski et al. 2024) that many SNe IIn are in binary systems, and mass-loss mechanisms in these systems may be more violent than the RLOF scenario. The mass-loss rates of binary interactions are poorly understood and may extend a large region of the mass-loss rate parameter space that we show in Figure 15 (N. Langer 2012; N. Smith et al. 2014). Some of our SNe IIn have mass-loss rates higher than what are typically understood to be from the great eruptions of LBVs (i.e., a few solar masses per year), such extreme mass-loss rates are attributed to dramatic mass-loss events due to binary interactions, beyond the mass-loss rates expected from RLOF (A. Kashi & N. Soker 2010; N. Soker & A. Kashi 2013; N. Smith & W. D. Arnett 2014; D. Dickinson et al. 2024; N. Smith et al. 2024). In this study, we have demonstrated that SNe IIn exhibit a diverse range of properties. When we consider the masses, CSM geometries, ejecta geometries, and mass-loss rates, we find that our sample is most consistent with massive progenitors, with many of these being likely LBVs (and perhaps some extreme RSGs). These findings are consistent with findings in the literature, where direct progenitor detections, high CSM masses, and high mass-loss rates converge on LBVs being the main progenitor path for SNe IIn.

9. Future Prospects and Discovery Rates in the Legacy Survey of Space and Time

Large surveys have made great strides in the discovery and classification of SNe. At the time of writing, there are $\sim 10^4$ classified SNe. The Legacy Survey of Space and Time (LSST) conducted at the Vera C. Rubin Observatory is scheduled to start observations in 2025 (LSST Science Collaboration et al. 2009; Ž. Ivezić et al. 2019), and is expected to increase the discovery rate of SNe to 10^6 yr^{-1}.

LSST has great potential to construct large samples of rare transients, such as SNe IIn. In order to estimate the SN IIn rate in LSST, we use our SN IIn sample to simulate a realistic population of transients observable with LSST, following V. A. Villar et al. (2018). First, we generate model light curves using the `MOSFiT` CSM models in the LSST *ugrizy* filter set using the priors from this work. We use rejection sampling of the simulated light curves to match the observed luminosity function with our Malmquist-corrected luminosity function. For these generated light curves, we use a log-uniform distribution of host galaxy extinction from 10^{-5} to 1 mag, consistent with the extinction observed in this sample. We inject simulated light curves into an LSST-like simulation, using `OpSim`.[13] In `OpSim`, we inject 100 generated SNe IIn into 20 equally spaced redshift bins spanning $z = 0.01$–1.5. These SNe are injected uniformly across the sky. For each SN at each redshift bin, we determine if $>=$ 10 points were detected at an SNR $>=$ 10 in any of the LSST *ugrizy* filters; if they are, then this is considered a detection. The number of detected SNe IIn is then multiplied by a volumetric rate at each redshift (see Equation (2) in V. A. Villar et al. 2018). This volumetric rate follows the models of L.-G. Strolger et al. (2015), assuming that SNe IIn comprise around 4% of CCSNe (e.g., C. Cold & J. Hjorth 2023). The resultant annual SN IIn rate in LSST is $\sim 1.6 \times 10^5$ yr^{-1}. This is a much higher rate than the estimate from `PLAsTiCC` of $\sim 6 \times 10^4$ yr^{-1} (R. Kessler et al. 2019), likely due to an artificially dim luminosity function used in the `PLAsTiCC` training set.

Clearly, not all of these objects will be able to be spectroscopically followed. Therefore, to build new, large samples of SNe IIn, photometric classifiers are required for rapid classification (e.g., SuperRAENN, Superphot, and Superphot+) (G. Hosseinzadeh et al. 2020; V. A. Villar et al. 2020; K. M. de Soto et al. 2024). Anomaly detection on real-time data may be able to find the peculiar light-curve bumps or precursor activity we see in many of our SNe IIn (e.g., LAISS) (P. D. Aleo et al. 2024). Furthermore, LSST may even aid in the direct progenitor detection of SNe IIn, elucidating the progenitor paths of these enigmatic transients (e.g., N. L. Strotjohann et al. 2024).

10. Conclusions and Summary

In this paper, we have performed the first systematic light-curve modeling of a large sample of 142 SNe IIn, mostly collected from large surveys such as ZTF, PTF, YSE, and PS1-MDS. Our light-curve models from E. Chatzopoulos et al. (2012) and implemented via `MOSFiT` allow us to infer the physical parameters of these

---

[13] v2.1.0 https://github.com/lsst/rubin_sim.

enigmatic and highly diverse transients. These parameters, along with other observational features, were used to explore correlations between parameter pairs and also to calculate mass-loss rates when accompanied by spectral information. Our conclusions can be summarized as follows:

1. Our large sample of SNe IIn shows a broad continuum of inferred parameters. However, these events typically have high mass-loss rates, large CSM, and pre-explosion masses, and a CSM geometry suggestive of eruptive mass loss. These parameters are all consistent with LBV progenitors.
2. These SNe have typical mass-loss rates of $\sim 10^{-2}\,M_\odot\,\mathrm{yr}^{-1}$. These mass-loss rates are consistent with the values in the literature and are typical of LBV progenitors.
3. The density profiles of the CSM skew toward $s = 2$, but the inferred population distribution spans a wide range of geometries. The median value of $s \approx 1.4$ suggests that the mass loss of SNe IIn progenitors is typically not undergoing steady-state, wind-like mass loss.
4. The inferred CSM mass surrounding SNe IIn is typically $\sim 1\,M_\odot$. This distribution does, however, extend to larger CSM masses (in excess of $10\,M_\odot$).
5. Ejecta mass is not particularly well constrained by our models. However, the median ejecta mass of $\sim 20\,M_\odot$ suggests massive progenitors.
6. The density profile of the inner ejecta, n, has a broad posterior distribution, with a median of ∼9.4 at the lower end of our physically informed prior. This is indicative of a more stripped or compact progenitor, such as LBVs.
7. Our SNe have very dense inner CSM profiles, with an average $\rho_0 \simeq 6 \times 10^{-12}\,\mathrm{g\,cm^{-3}}$. This value is consistent with the range found in the literature.
8. The r-band rise time is strongly, positively correlated with the CSM mass– i.e., the more CSM the progenitor has around it, the slower its rise to peak. The fall time of the r-band light curve is also strongly positively correlated with the CSM mass, with higher CSM masses resulting in a more slowly fading transient. This is consistent with the findings of A. Nyholm et al. (2020).
9. Similarly, the r-band fall times and rise times are positively correlated, indicating that slowly rising SNe IIn also slowly fade. There is a negative correlation between the r-band fall time and the peak absolute r-band magnitude, suggesting that the more luminous an SN IIn is, the slower it will fade. These correlations are driven by the CSM in each SN.
10. We find multimodality in the fall time, with a long fall time subgroup which is centered around 200 days and a main grouping centered around 50 days. These long fall time SNe IIn tend to have massive CSM.
11. We find no statistically significant evidence of multimodality in the distribution of the radiated energy in our SNe IIn. However, we do note that there are tentative peaks in the distribution at a few 10^{49} erg and a few 10^{50} erg.
12. We can group our SNe into several broad photometric categories, which form a continuum. There is a small population of fast decliners, with ∼20% of our sample having fall times of less than a month. While our temporal coverage is typically not long enough to confirm, there are several examples of slowly declining SNe IIn in our sample. These may be consistent with the observed population of long-lived SNe IIn. Within our sample, around 15% of the transients are very luminous, with a peak r-band absolute magnitude of at least –20 mag. Conversely, there is a population of fast risers, which makes up around 25% of the sample, a smaller proportion than found by A. Nyholm et al. (2020).
13. The host galaxies of our SNe IIn are primarily star-forming spiral galaxies (as expected for massive progenitors), with one exception of an elliptical host.
14. Our sample of SNe is consistent with the distribution of the peak r-band absolute magnitude found in the literature (e.g., M. Kiewe et al. 2012), with a Malmquist-corrected average (and standard deviation) of -18.7 ± 1.0 mag.
15. Finally, using our Malmquist-corrected luminosity function, we simulate the discovery rates of SNe IIn in the upcoming LSST. We estimate that the SN IIn discovery rate will be $\sim 1.6 \times 10^5\,\mathrm{yr}^{-1}$.

For the first time, utilizing a large sample and systematic modeling, we have found that the majority of the progenitors of SNe IIn are consistent with LBVs. The high mass-loss rates, large CSM masses and total masses, along with the typical CSM geometries, are all suggestive of massive progenitors that suffer eruptive mass-loss events (whether as a single star or due to binary interaction). In the upcoming years, we expect the SNe IIn sample to increase by over three orders of magnitude–opening the possibility to better understand the explore the energetics, environments, and progenitor channels of these events.

Acknowledgments

We thank the anonymous referee for their insightful comments, which helped to improve this paper. C.L.R. and V.A.V. acknowledge previous support from the Charles E. Kaufman Foundation through the New Investigator grant KA2022-129525. The Villar Astro Time Lab acknowledges support through the David and Lucile Packard Foundation, National Science Foundation under AST-2433718, AST-2407922, and AST-2406110, as well as an Aramont Fellowship for Emerging Science Research. This work is additionally supported by NSF under Cooperative Agreement PHY-2019786 (The NSF AI Institute for Artificial Intelligence and Fundamental Interactions.[14]

The Pan-STARRS1 Surveys (PS1) and the PS1 public science archive have been made possible through contributions by the Institute for Astronomy, the University of Hawaii, the Pan-STARRS Project Office, the Max-Planck Society and its participating institutes, the Max Planck Institute for Astronomy, Heidelberg and the Max Planck Institute for Extraterrestrial Physics, Garching, The Johns Hopkins University, Durham University, the University of Edinburgh, the Queen's University Belfast, the Harvard-Smithsonian Center for Astrophysics, the Las Cumbres Observatory Global Telescope Network Incorporated, the National Central University of Taiwan, the Space Telescope Science Institute, the National Aeronautics and Space Administration under grant No. NNX08AR22G issued through the Planetary Science Division of the NASA Science Mission Directorate, the National

---

[14] https://iaifi.org/

Science Foundation grant No. AST-1238877, the University of Maryland, Eotvos Lorand University (ELTE), the Los Alamos National Laboratory, and the Gordon and Betty Moore Foundation.

This research has made use of the NASA/IPAC Extragalactic Database (NED), which is operated by the Jet Propulsion Laboratory, California Institute of Technology, under contract with the National Aeronautics and Space Administration.

YSE-PZ was developed by the UC Santa Cruz Transients Team with support from The UCSC team is supported in part by NASA grants NNG17PX03C, 80NSSC19K1386, and 80NSSC20K0953; NSF grants AST-1518052, AST-1815935, and AST-1911206; the Gordon & Betty Moore Foundation; the Heising-Simons Foundation; a fellowship from the David and Lucile Packard Foundation to R. J. Foley; Gordon and Betty Moore Foundation postdoctoral fellowships and a NASA Einstein fellowship, as administered through the NASA Hubble Fellowship program and grant HST-HF2-51462.001, to D. O. Jones; and a National Science Foundation Graduate Research Fellowship, administered through grant No. DGE-1339067, to D. A. Coulter.

Facilities: PS1, PO:1.2m.

Software: `astropy` (The Astropy Collaboration et al. 2013), `MOSFiT` (J. Guillochon et al. 2017), `NumPy` (T. Oliphant 2006), `pandas` (pandas development team 2020), `scikit` (F. Pedregosa et al. 2011).

Appendix A
Testing `MOSFiT` CSM Models with the Superluminous Models of L. Dessart et al. (2015)

It has been noticed that the CSM–ejecta interaction models implemented in `MOSFiT` may overestimate CSM masses in some cases. M. Nicholl et al. (2020) used `MOSFiT` to model the light curve of the SLSN-II, SN 2016aps. Those authors initially argued that the transient may be an example of a PISN from a very massive star. Along with a large radiated energy budget of $\sim 10^{52}$ erg and a slow evolution timescale, modeling suggested that SN 2016aps could be explained by $\sim 100\,M_\odot$ of ejecta colliding with $\sim 100\,M_\odot$ of CSM. However, A. Suzuki et al. (2021) note that the models for SLSNe IIn from L. Dessart et al. (2015) can reproduce a similar luminosity and photometric timescale evolution to SN 2016aps with much more modest parameters (with $M_{\rm CSM} \sim 17\,M_\odot$ and $M_{\rm ej} \sim 10\,M_\odot$). Those authors go on to model SN 2016aps with radiation-hydrodynamic simulations, finding that SN 2016aps still had a very massive progenitor, but consisted of $30\,M_\odot$ of ejecta colliding around $8\,M_\odot$ of CSM.

To test the validity of the `MOSFiT` inferences for SNe IIn that verge on the superluminous (i.e., ~ -20 mag), we take the models of SLSNe IIn from L. Dessart et al. (2015) and fit the light curves with `MOSFiT`. In these models, $\sim 10\,M_\odot$ of ejecta interacts with varying CSM masses at various maximum ejecta velocities. The inner CSM is at $R_0 \approx 70$ au. In our `MOSFiT` fits, we leave the CSM mass and ejecta velocity as free parameters, but fix the others to match that of L. Dessart et al. (2015). The comparisons of the CSM mass values from our fits with the values from L. Dessart et al. (2015) are shown in Figure 17. Within the 1σ uncertainties, four out of the eight trials are consistent with the L. Dessart et al. (2015) models. The other trials, however, are typically within $\sim 10\%$ of the L. Dessart et al. (2015) value. The one set of parameters that does not agree well is the Xe10m6 trial, which had high ejecta and SN kinetic energies, $\sim 17\,M_\odot$ of CSM, and a high ejecta velocity of $\sim 30{,}000$ km s^{-1}. This configuration results in a very high inner CSM density of $\sim 10^{-8}$ g cm^{-3}, which is well outside of our allowed range.

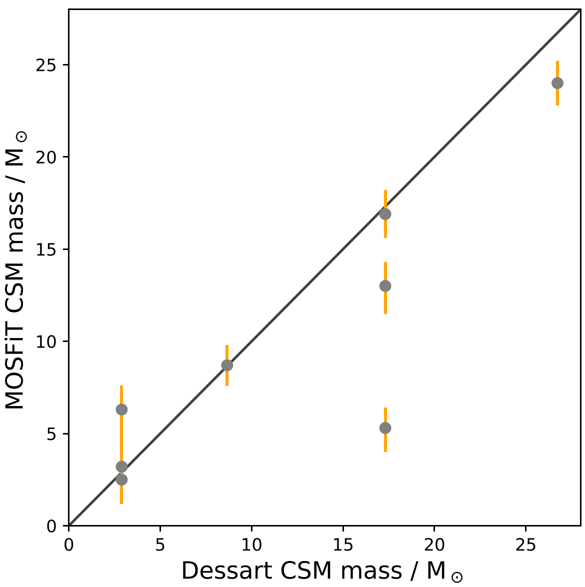

Figure 17. Scatter between the CSM masses inferred by `MOSFiT` and the models of L. Dessart et al. (2015). Error bars are at the 1σ level, and the 1:1 line is plotted in black.

Appendix B
Luminosity Function

Our sample suffers from Malmquist bias, meaning that our sample is biased toward SNe that are observationally brighter (K. G. Malmquist 1922). Some of our sample is constructed from magnitude-limited surveys, which inherently contain Malmquist bias, with around 60% of the sample coming from ZTF BTS, which has a cut for peak magnitude but is spectroscopically complete. In order to correct this bias in our luminosity function (absolute *r*-band magnitude, the most comparable measure in our sample), we implement the method outlined in D. Richardson et al. (2014), F. Taddia et al. (2019), and A. Nyholm et al. (2020), which was used on magnitude-limited surveys such as PTF/iPTF (F. Taddia et al. 2019; A. Nyholm et al. 2020) and samples from numerous sources (D. Richardson et al. 2014).

To set up our Malmquist bias correction, we find the absolute magnitude limit based on a selected survey limiting magnitude. In this case, as the majority of our sample is from the ZTF BTS, we use the apparent magnitude cutoff of 19.5 mag in the *r* band (this is shown as the diagonal line in Figure 18). Any SNe found to the diagonal left (i.e., brighter than the limit) is considered part of a "complete" sample. Then, the intrinsically faintest member of the sample is identified. In this case, the faintest SN in our BTS sample has an *r*-band absolute magnitude of –17.0 mag. The intersection between this faintest SN and the ZTF BTS magnitude cutoff tells us to which distance modulus our sample is complete to (i.e., 35.69). The sample is then split

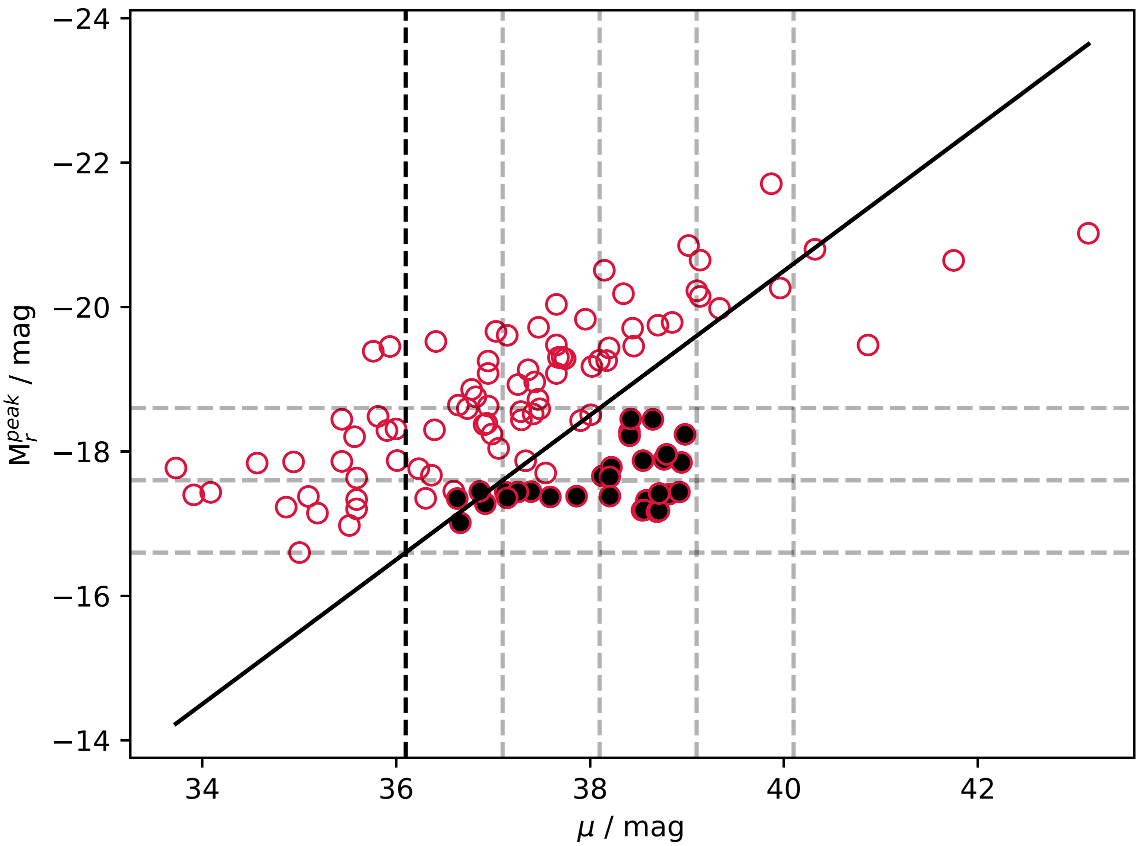

Figure 18. A Miller diagram, showing the peak r-band absolute magnitudes of our SNe IIn (the subsample that shares a comparable r-band filter) against their distance moduli. The solid diagonal line is the absolute r-band magnitude cutoff for the ZTF BTS. The vertical dashed black line is the distance modulus at which the absolute magnitude of the faintest member of the sample intercepts with the ZTF BTS magnitude cut limit. The gray dashed lines define the magnitude and distance modulus bins that are used in the simulation of the missing SNe IIn. The empty circles are the SNe IIn used in this analysis, and the circles filled in black are the simulated missing SNe IIn from our Malmquist bias correction.

between –17 and –18 mag as our intrinsic distribution of "faint" SNe, and another between –18 and –19 mag. These distributions, while not complete in the sense that all SNe are present, are taken to be representative of the luminosity distribution. The fraction of luminous SNe to the fainter ones is then used to simulate the missing SNe at larger distance moduli, iteratively for each of the subsequent 2 distance bins. Before the correction for the Malmquist bias, the distribution is roughly Gaussian with a mean peak r-band absolute magnitude and spread of -19.2 ± 1.0 mag; with correction, it is -18.7 ± 1.0 mag, both of which are consistent with the average found by M. Kiewe et al. (2012). Our simulated missing SNe are represented by the filled circles in Figure 18.

Appendix C
Individual Object Posterior Distributions

Due to there being an apparent "pile-up" in the joint posterior distributions shown in Section 4.1, we plot the individual transient posteriors and compare against the full sample. Many of our parameters probe the full prior distribution, showing a slight preference for the higher/lower end of the prior range (e.g., s and n). The velocity posterior distributions are centered around the average value seen in the joint posterior. The apparent pile-up to the extremes of the prior distributions is less pronounced here, suggesting an additive effect. We also calculate the fraction of the individual posterior distributions where the modal bins are at the extreme bounds of the prior distribution (i.e., the first and last bins). These distributions are shown in Figure 19.

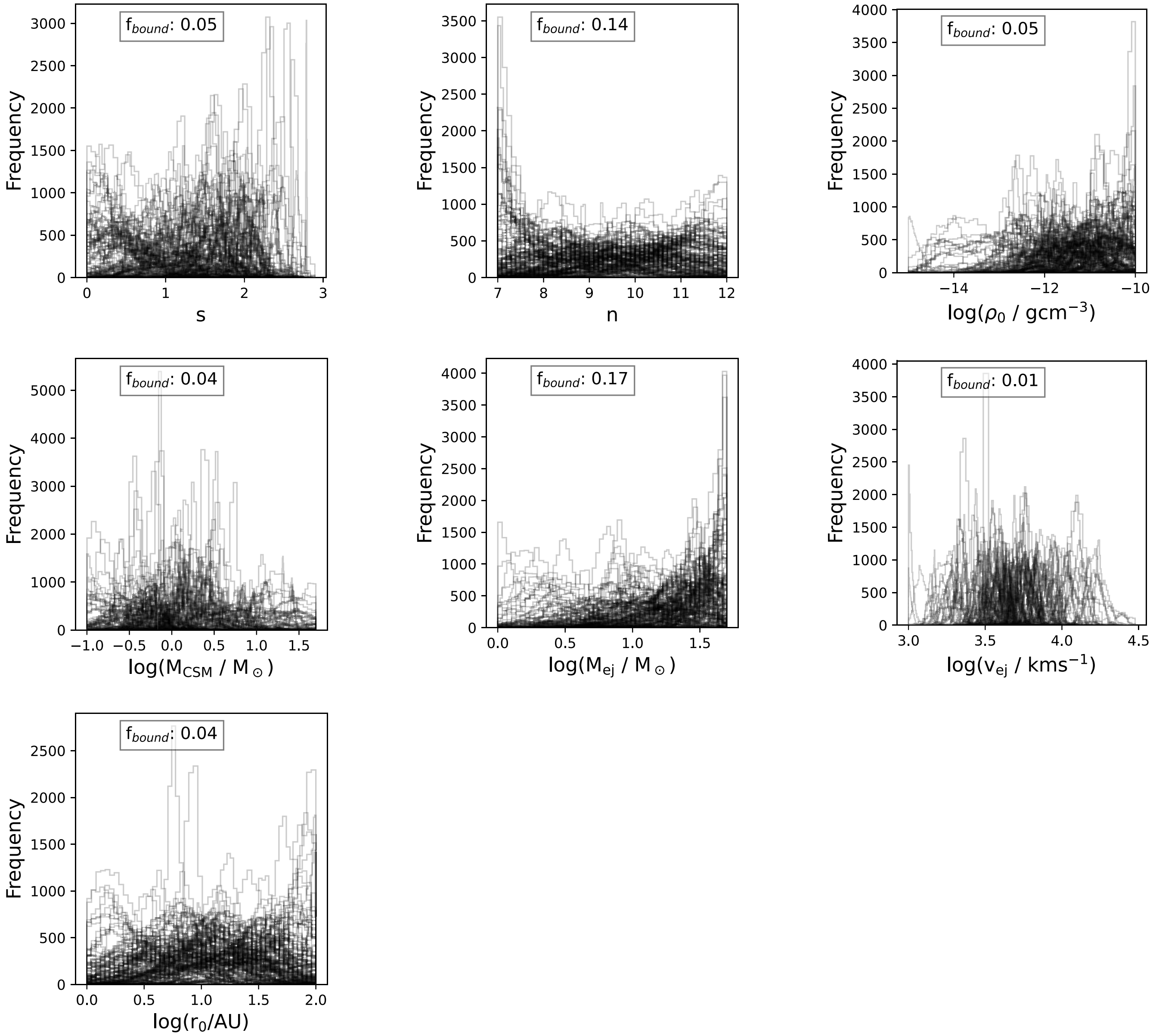

Figure 19. Top left: the individual posteriors of s. While there is a slight apparent preference toward $s = 2$, there is a spread over all values of s, suggesting we are probing a diverse set of geometry parameters. Top middle: the individual posterior distributions for n. These distributions show a preference for smaller n values, but again, generally span the full prior distribution. Top right: the individual posterior distributions for ρ_0. These distributions show a preference for a denser inner CSM. Bottom left: the individual posterior distributions for the CSM mass. Here, the distributions prefer a CSM mass of around 1 $M_\odot$. Bottom middle: the individual posteriors for the ejecta mass. Our distributions skew to the higher end of the prior distribution, but also probe smaller masses. Bottom right: the individual posterior distributions of the ejecta velocity. These distributions are centered around ~4000 km s^{-1}. This is representative of the Gaussian-like joint posterior distribution. Also shown in each of these plots is the fraction of the realizations with modal values at either bound of the prior distribution.

Appendix D
Assessing the Contribution of the Hα Line to the *r*-band Flux

The CSM interaction model we implement does not explicitly consider the flux contribution from the strong Hα emission lines. In the local universe, the Hα line is in the r band. We assess this contribution in order to determine if there is a significant systematic difference between the light-curve fits and observations due to unaccounted Balmer emission.

In order to estimate this contribution, we performed synthetic photometry on a representative sample of SN IIn spectra using `synphot` version 1.1.2 (STScI Development Team 2018). We use the spectra for the SNe IIn in C. L. Ransome et al. (2021), which were collated from the Open Supernova Catalog (J. Guillochon et al. 2017). In total, 139 spectra are used. These SNe IIn have multiple spectral epochs spanning a range of ~10–10^3 days. An r-band filter in `synphot` was used for the synthetic photometry on the spectra. The flux from the full r-band bandpass (5400–7000 Å) was measured for each spectrum. Then the flux from these spectra with the Hα region masked out and the spectrum interpolated to the continuum, effectively removing the Hα emission. The flux differences between the unaltered and altered spectra were assessed using

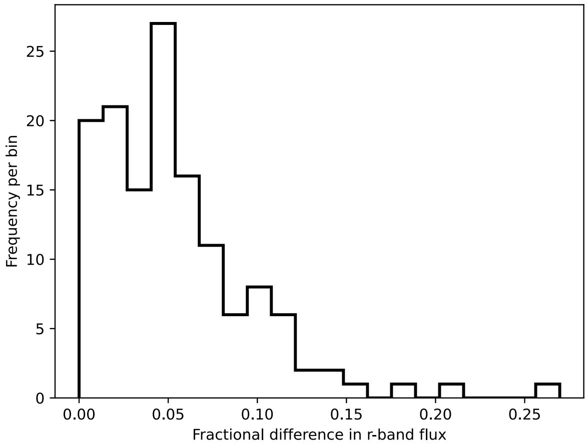

Figure 20. Histogram showing the fractional difference in *r*-band flux, i.e., the fractional difference between synthetic photometry measurements of SN IIn spectra and spectra with the Hα lines removed.

the fractional difference of flux in the *r*-band bandpass, where the difference in counts is normalized by the full *r*-band flux.

The fractional flux differences between the spectra within 100 days of the explosion are shown in Figure 20. We find that 60% of the fractional differences are below the 5% level, and 84% of the sample is below the 10% level. We find that when the differences are assessed over longer timescales, especially in the case of the long-lasting SNe IIn, such as SN 2005ip and SN 2006jd, these differences are more appreciable. When these data are available, we see that the fractional differences may increase with time. At late times for the long-lasting SNe IIn (thousands of days post-explosion), the fractional differences increase and may begin to dominate over the continuum.

In this paper, our `MOSFiT` models are fitted for a duration of a few hundred days post-peak brightness, so the typical fractional flux differences are largely negligible.

Appendix E
Fall Time Silver Sample

In our analysis measuring the fall time from peak, we exclude SNe IIn that do not have data covering a decay of 1 mag from the *r*-band peak. Here we extend our models beyond the time range of the data to estimate the fall times for a "silver" sample (albeit, less constrained, with a median spread of ~5 days for the silver sample, compared to ~1 day for the gold sample). There are 46 silver SNe IIn for this analysis. A histogram of the fall time distribution is shown in Figure 21. This distribution is consistent with the main set of fall time measurements presented in Section 4.2. The median fall time and spread is $\sim 60^{+88}_{-24}$ days. While the individual objects may be less constrained in terms of the fall times when the model light curves are extended, this set shows a similar distribution to the full set, with two components found by a GMM.

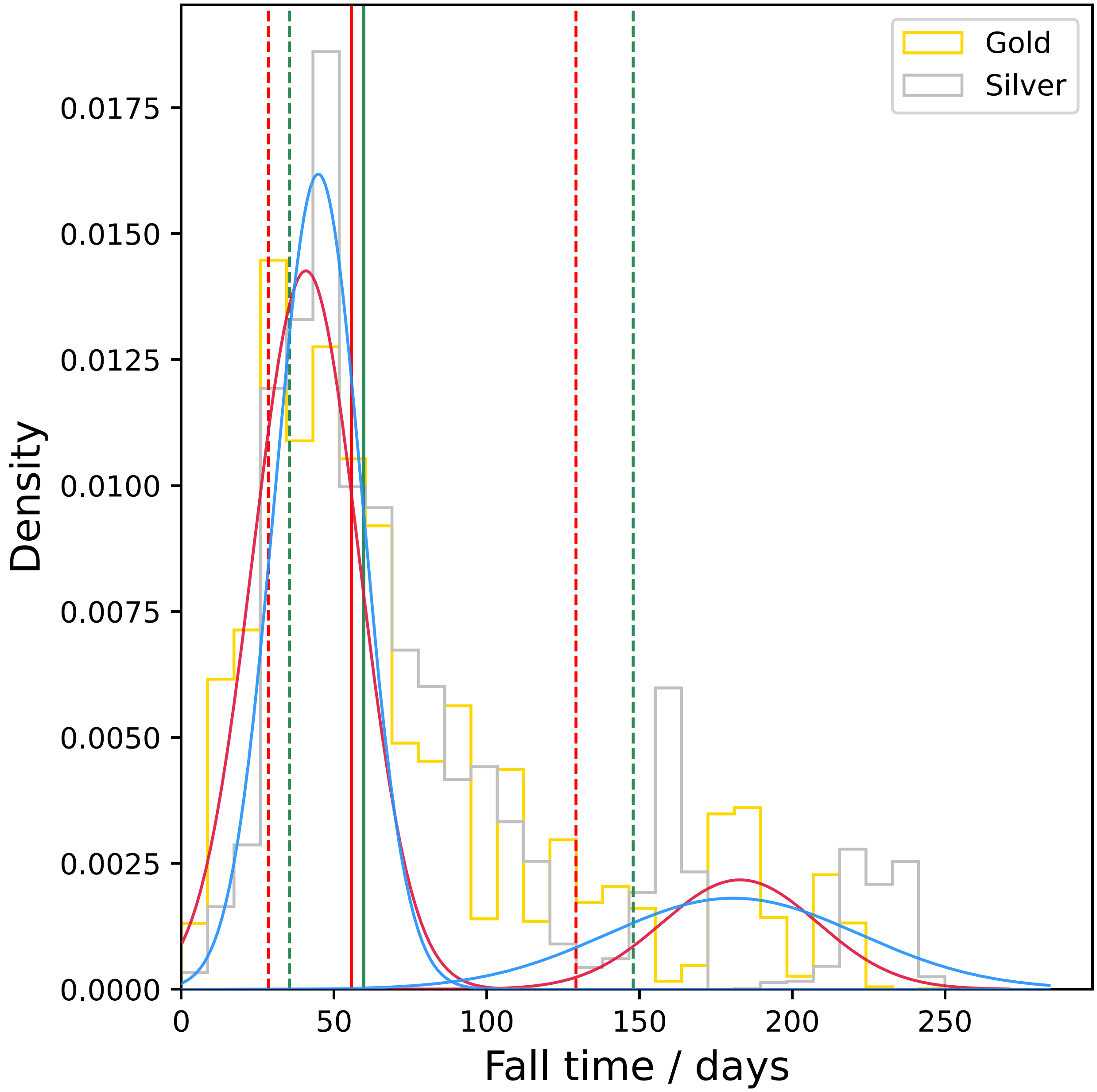

Figure 21. The fall time distribution of the silver SNe IIn, where the data does not show a decline of 1 mag from the *r*-band peak. This distribution is shown as a silver histogram. The median is shown by the solid green vertical line, and the bounds of the spread are highlighted by dashed vertical green lines. The blue Gaussians are the components found by a GMM analysis, and show a main shorter fall time component and a longer fall time component. Also plotted for comparison is the main sample, or gold sample, where a fall time measurement was possible. This is shown as a gold histogram, with red GMM components and red lines demarking the median and bounds of the spread.

Appendix F
Excluded Transients

Some subclasses of SNe IIn are omitted in our analysis as they likely deviate from the CCSN regime of SNe IIn. Notably, in the gold sample of C. L. Ransome et al. (2022), SN 2008S is a low luminosity, nearby transient in the Fireworks Galaxy, NGC 6946 (R. Arbour 2008). Due to the low energy of this SN, it was initially proposed to be an SN impostor. However, S. M. Adams et al. (2016), using Hubble Space Telescope and Spitzer data, conclude that the progenitor had disappeared. We exclude this transient as there is a possibility that a surviving progenitor is heavily dust enshrouded. SN 2008S was interacting throughout its evolution. If this transient was an ecSN, then the interaction possibly would have been fleeting (e.g., SN 2018zd) (D. Hiramatsu et al. 2021). As suggested by S. M. Adams et al. (2016), the ultimate fate of this object may be revealed by JWST in the future and may be included in future samples if the progenitor is truly gone. Other events classed as impostors were not included in our light-curve modeling, with these objects being cataloged by C. L. Ransome et al. (2021; e.g., SN 1997bs, SN 2000ch, and SN 2013fs).

The thermonuclear explosion of a white dwarf embedded in a dense CSM gives rise to the thermonuclear SN IIn subclass, or SNe Ia CSM (less commonly known as SNe IIa or SNe Ian (L. Dessart 2024). As these are not CCSNe, they are not an appropriate application of our models, so we exclude some transients in the gold sample of C. L. Ransome et al. (2021), including SN 2005gj (J. Prieto et al. 2005) and SN 2008J (F. Taddia et al. 2012). We still include the superluminous SN 2006gy, but we do note that recent work suggests that

SN 2006gy may have thermonuclear origins (based on late-time spectroscopy) (A. Jerkstrand et al. 2020).

Appendix G
Parameters from `MOSFiT`

Table 5 outlines a truncated parameter list from our light-curve fits.

Table 5
Truncated List Describing the Inferred `MOSFiT` Parameters for Our Sample

SN Name	s	s_{84}	s_{16}	log(ρ / g cm^{-3})	log(ρ_{84}/g cm^{-3})	log(ρ_{16}/g cm^{-3})	M_{CSM} / $M_\odot$	⋯
iPTF13agz	0.112680	0.107441	0.076236	−10.159243	0.097170	0.104867	0.348364	⋯
iPTF13asr	1.170783	0.099046	0.126736	−11.150525	0.258106	1.255099	0.739383	⋯
iPTF14bpa	0.248575	0.324317	0.177164	−10.350187	0.285098	0.446765	4.253895	⋯
iPTF15aym	1.950613	0.048451	0.062104	−10.109321	0.080193	0.147496	0.734564	⋯
iPTF15bky	0.800489	0.274837	0.312324	1.958260e-12	6.477530e-13	5.281630e-13	1.064046	⋯
⋯	⋯.	⋯	⋯	⋯	⋯	⋯	⋯	⋯

Note. Here we show the median and 84th and 16th percentile spread of the distribution. The full table with the complete set of parameters for our full sample is found in the online materials.

(This table is available in its entirety in machine-readable form in the online article.)

Appendix H
Target Lists

Table 6 outlines our target list used in this work. Table 7 outlines the excluded transients from our larger sample.

Table 6
The Full Sample of Spectroscopically Confirmed SNe IIn That We Use in This Work

SN Name	Host	Host Type	z	R.A. (J2000)	Decl. (J2000)	Reference
SN 1989C	MCG+01-25-25	SB	0.0063	09:47:45.49	02:37:36.10	P. Challis[a]
SN 1994W	NGC 4041	SAB	0.0040	12:02:10.92	62:08:32.70	C. L. Ransome et al. (2021)
SN 1994Y	NGC 5371	SABbc	0.0085	13:55:36.90	40:27:53.40	A. Clocchiatti et al. (1994)
SN 1995N	MCG-02-38-17	IB	0.0062	14:49:28.29	−10:10:14.40	C. Pollas et al. (1995)
SN 1998S	NGC 3877	SA	0.0030	11:46:06.13	47:28:55.40	B. E. Schaefer & B. Roscherr (1998)
SN 2005db	NGC 214	Sbc	0.0151	00:41:26.79	25:29:51.60	N. Blanc et al. (2005a)
SN 2006gy	NGC 1260	SB 0a	0.0192	03:17:27.06	41:24:19.51	R. J. Foley et al. (2006)
SN 2008B	NGC 5829	⋯	0.0188	15:02:43.65	23:20:07.80	S. Blondin et al. (2008)
SN 2018fdt	Z 197-30	SBc	0.0550	17:04:44.33	+38:14:08.00	J. Tonry et al. (2018b), C. Fremling et al. (2018a)
SN 2018khn	WISEA J085619.17+523252.7	⋯	0.0910	08:56:18.01	+52:32:58.00	J. Nordin et al. (2018a), C. Fremling et al. (2019b)
SN 2018kyv	WISEA J130104.80+262103.2	⋯	0.0940	13:01:04.95	+26:21:03.80	J. Nordin et al. (2018b), J. Nordin et al. (2018b)
SN 2018leh	UGC 2949	SB:ab	0.0240	04:05:03.30	+25:15:42.90	M. Villi (2018), A. Dugas et al. (2019a)
SN 2018lmy	⋯	⋯	0.0520	18:24:27.77	+46:37:09.50	A. Delgado et al. (2019), M. A. Tucker et al. (2019b)
SN 2019bxq	2MASX J16575851+7836144	E	0.0140	16:57:58.51	+78:36:13.60	J. Nordin et al. (2019a), C. Fremling et al. (2019c)
SN 2019dvv	LEDA 89698	S	0.0305	12:23:17.77	+19:43:23.30	J. Nordin et al. (2019b), C. Fremling et al. (2019a)
SN 2019hgy	WISEA J174820.57+481206.9	⋯	0.0360	17:48:20.50	+48:12:07.00	C. Fremling (2019a), C. Fremling et al. (2020a)
SN 2019krt	SDSS J165256.08+204305.6	⋯	0.0300	16:52:54.76	+20:43:03.50	J. Nordin et al. (2019c), C. Fremling et al. (2019d)
SN 2019kud	SDSS J144429.05+335919.1	SBc	0.0324	14:44:29.73	+33:59:10.08	J. Tonry et al. (2019a), A. Dugas et al. (2019b)
SN 2019lkr	LEDA 2756618	⋯	0.0300	16:05:07.98	+73:35:04.00	J. Nordin et al. (2019d), S. J. Prentice et al. (2019a)
SN 2019pgu	⋯	⋯	0.1055	16:18:42.83	+67:54:00.30	J. Tonry et al. (2019b), A. Dahiwale & C. Fremling (2020a)
SN 2019qny	LEDA 1083065	⋯	0.0480	03:32:59.94	−02:46:41.50	K. C. Chambers et al. (2019a), C. Fremling et al. (2019c)
SN 2019qt	⋯	⋯	0.0350	14:59:10.65	+43:49:11.60	J. Nordin et al. (2019e), A. V. Payne et al. (2019)
SN 2019qvr	⋯	⋯	0.0750	03:41:21.69	+22:49:20.80	F. Forster (2019a), C. Fremling et al. (2019g)
SN 2019rz	UGC 3445	SB:b	0.0189	06:50:25.81	+43:03:11.60	K. Z. Stanek (2019), K. Z. Stanek (2019)
SN 2019sxv	2MASX J22195786+2537447	⋯	0.0400	22:19:58.25	+25:37:46.70	F. Forster (2019b), C. Fremling et al. (2019h)
SN 2019vkl	WISEA J015630.94+182623.5	⋯	0.0640	01:56:30.79	+18:26:23.80	J. Nordin et al. (2019f), J. Zhang (2019)
SN 2019wmf	WISEA J102954.55+704710.0	⋯	0.0600	10:29:53.88	+70:47:09.60	F. Forster et al. (2019), S. J. Prentice et al. (2019b)
SN 2019wnc	LEDA 1183665	⋯	0.0216	10:10:56.36	+01:04:17.10	K. De (2019), D. Perley (2019)
SN 2020fhw	WISEA J150029.88+171410.8	⋯	0.1116	15:00:29.89	+17:14:10.50	J. Tonry et al. (2020b), L. Yan et al. (2020b)
SN 2020hem	2MASX J15024011+0918137	⋯	0.0935	15:02:40.15	+09:18:13.80	F. Forster et al. (2020a), A. Dahiwale & C. Fremling (2020b)
SN 2020rc	⋯	⋯	0.0810	11:50:34.07	−04:20:22.70	C. Fremling (2020a), M. L. Graham et al. (2020a)
SN 2020rno	⋯	⋯	0.0640	01:18:51.79	+18:40:09.50	F. Forster et al. (2020b), D. A. Perley et al. (2020b)
SN 2020sj	⋯	⋯	0.0770	09:26:19.87	−07:28:30.00	J. Nordin et al. (2020b), I. Irani et al. (2020)
SN 2020tis	WISEA J235725.57+250330.7	⋯	0.0577	23:57:24.78	+25:03:48.60	F. Forster et al. (2020e), A. Dahiwale & C. Fremling (2020c)
SN 2020tyk	⋯	⋯	0.0870	01:37:58.38	+20:00:03.00	R. Shirley et al. (2020a), J. Tonry et al. (2020c)
SN 2020vci	⋯	⋯	0.1930	15:04:22.63	+51:04:56.80	J. Tonry et al. (2020a), A. Dahiwale & C. Fremling (2021d)
SN 2020vou	WISEA J233743.84+215110.8	⋯	0.1190	23:37:43.80	+21:51:14.60	K. C. Chambers et al. (2020a), K. E. Weil & D. Milisavljevic (2020)
SN 2020xpo	GALEXASC J023225.46–125741.7	⋯	0.0750	02:32:25.65	−12:57:41.00	F. Forster et al. (2020c), M. Gromadzki et al. (2020a)
SN 2020yy	SDSS J141853.90+630945.	⋯	0.0675	14:18:53.91	+63:09:45.00	R. Shirley et al. (2020b), S. Gomez et al. (2020)
SN 2020zos	WISEA J050632.07+074535.3	⋯	0.1400	05:06:32.08	+07:45:36.40	F. Forster et al. (2020d), P. Blanchard (2020)
SN 2020aafb	WISEA J015128.98+224947.2	⋯	0.0780	01:51:28.95	+22:49:44.10	A. Munoz-Arancibia et al. (2020a), D. Perley (2020)
SN 2020aaut	LEDA 1221074	⋯	0.0757	12:09:12.54	+02:15:24.30	A. Munoz-Arancibia et al. (2020b), A. Dahiwale & C. Fremling (2021e)
SN 2021bwf	SDSS J163457.25+562855.8	⋯	0.1940	16:35:02.90	+56:28:38.40	A. Munoz-Arancibia et al. (2021a), S. Prentice et al. (2021a)
SN 2021bxo	Mrk 1209Ê	Sp	0.0339	08:04:00.58	+10:00:33.50	K. De (2021a), D. Perley (2021a)
SN 2021ezt	2MASX J16583923+2629311	⋯	0.0502	16:58:38.98	+26:29:32.40	F. Forster et al. (2021a), A. Dahiwale & C. Fremling (2021f)
SN 2021fel	WISEA J165158.55+623404.8	⋯	0.0680	16:51:58.52	+62:34:04.30	A. Munoz-Arancibia et al. (2021b), M. A. Tucker (2021a)

Table 6
(Continued)

SN Name	Host	Host Type	z	R.A. (J2000)	Decl. (J2000)	Reference
SN 2021fpn	ZwCl 1012–0047	⋯	0.0424	10:13:47.65	−00:54:55.00	J. Tonry et al. (2021a), P. Pessi et al. (2021)
SN 2021gpw	WISEA J132154.84+164439.7	⋯	0.0750	13:21:54.85	+16:44:39.70	J. Tonry et al. (2021b), D. Perley (2021b)
SN 2021hsn	⋯	⋯	0.0540	19:22:16.83	+56:21:00.20	F. Forster et al. (2021g), D. Perley (2021c)
SN 2021hur	LEDA 2773190	⋯	0.0300	13:30:59.36	+77:12:52.60	C. Fremling (2021a), S. Prentice et al. (2021b)
SN 2021iui	SDSS J141659.24+321406.7	⋯	0.1060	14:16:59.19	+32:14:06.50	J. Tonry et al. (2021c), F. Poidevin et al. (2021)
SN 2021 kat	⋯	⋯	0.1013	19:50:31.65	+57:59:28.00	F. Forster et al. (2021b), S. Schulze et al. (2021a)
SN 2021kqv	UGC 10132	SB:b	0.0510	15:56:52.03	+78:27:48.90	A. Munoz-Arancibia et al. (2021c), S. Schulze et al. (2021b)
SN 2021kwc	NGC 5231	SA	0.0218	13:35:47.91	+02:59:59.30	F. Forster et al. (2021h), A. Dahiwale & C. Fremling (2021a)
SN 2021kwj	WISEA J181949.35+561011.3	⋯	0.0250	18:19:49.50	+56:10:01.20	F. Forster et al. (2021c), D. Perley (2021d)
SN 2021lhy	WiggleZ R22J213215370–00310110	⋯	0.1420	21:32:14.94	−00:30:05.10	A. Munoz-Arancibia et al. (2021d), M. Pursiainen et al. (2021)
SN 2021osr	2MASX J21345199–0726529	⋯	0.0855	21:34:51.91	−07:26:54.50	A. Munoz-Arancibia et al. (2021e), G. Hosseinzadeh et al. (2021)
SN 2021qeq	⋯	⋯	0.0550	16:54:26.77	+53:43:26.30	J. Nordin et al. (2021a), D. A. Perley et al. (2021)
SN 2021qug	J220232.70–164537.8	⋯	0.0570	22:02:32.45	−16:45:36.40	C. Fremling (2021b), D. Perley (2021e)
SN 2021ras	2MASX J17385176+2622447	⋯	0.0290	17:38:51.92	+26:22:44.20	J. Nordin et al. (2021b), J. Nordin et al. (2021b)
SN 2021srg	WISEA J231817.23+145004.	⋯	0.0690	23:18:17.26	+14:50:04.80	C. Fremling (2021c), S. Gomez et al. (2021)
SN 2021ukt	UGC 505	S	0.0129	00:49:24.86	−01:45:58.70	K. De (2021b), J. Hinkle (2021)
SN 2021uru	LEDA 864812	⋯	0.0540	02:52:22.67	−18:41:47.50	J. Tonry et al. (2021d), M. A. Tucker (2021b)
SN 2021vzp	2MASX J03473546+0252586	⋯	0.0310	03:47:35.55	+02:52:58.40	J. Tonry et al. (2021e), M. Deckers et al. (2021)
SN 2021wrr	WISEA J171107.70+722919.8	⋯	0.0480	17:11:07.79	+72:29:19.80	F. Forster et al. (2021d), M. Chu et al. (2021a)
SN 2021yaz	⋯	⋯	0.0390	02:30:37.00	+25:26:07.50	J. Nordin et al. (2021c), M. Chu et al. (2021b)
SN 2021ydc	WISEA J012517.64+222324.8	⋯	0.0550	01:25:17.62	+22:23:25.30	A. Munoz-Arancibia et al. (2021f), C. Gutierrez et al. (2022)
SN 2021yys	2MASX J07254250+4449209	⋯	0.0433	07:25:42.21	+44:49:25.10	A. Munoz-Arancibia et al. (2021g), D. Perley (2021f)
SN 2021yyy	WISEA J224007.46–050012.4	⋯	0.0930	22:40:07.55	−05:00:12.50	R. Carini et al. (2021)
SN 2022fnl	WISEA J153342.47+434445.5	⋯	0.1035	15:33:42.47	+43:44:45.40	J. Tonry et al. (2022a), S. Schulze et al. (2022)
SN 2022jie	LEDA 2669503	⋯	0.0748	12:42:48.12	+64:34:29.60	A. Munoz-Arancibia et al. (2022a), D. Perley & K. Hinds (2022)
SN 2022mds	WISEA J173233.61+431623.3	⋯	0.0745	17:32:33.90	+43:16:27.10	A. Munoz-Arancibia et al. (2022b), F. Poidevin et al. (2022a)
SN 2022mma	Z 104–58	Sc	0.0380	14:39:01.49	+15:59:11.70	I. Perez-Fournon et al. (2022a), C. Pellegrino et al. (2022)
SN 2022myl	Z 169–7	⋯	0.0371	16:51:02.37	+30:39:52.30	F. Forster et al. (2022a), K. Hinds & D. Perley (2022)
SN 2022oeh	LEDA 2273049	⋯	0.0300	19:16:50.01	+45:57:18.60	F. Forster et al. (2022b), D. Perley et al. (2022b)
SN 2022paz	⋯	⋯	0.0660	18:05:09.01	+32:09:00.90	K. C. Chambers et al. (2022), M. E. Huber (2022)
SN 2022prr	NGC 6745	⋯	0.0152	19:01:41.90	+40:45:03.70	K. Z. Stanek (2022), T. D. Jaeger (2022)
SN 2022pss	⋯	⋯	0.0600	01:28:19.22	+20:23:45.30	A. Munoz-Arancibia et al. (2022c), C. Gutierrez et al. (2022)
SN 2022rhl	⋯	⋯	0.1180	19:20:44.21	+46:52:54.70	C. Fremling (2022a), F. Poidevin et al. (2022b)
SN 2022tbh	LEDA 2706824	⋯	0.0520	17:25:09.72	+67:49:45.77	C. Fremling (2022b), S. Schulze & J. Sollerman (2022)
SN 2022ymc	⋯	⋯	0.0280	03:13:40.62	−01:16:32.21	D. O. Jones et al. (2022), X. Sheng et al. (2022)
SN 2022zyd	⋯	⋯	0.0630	02:08:33.20	+52:49:36.37	C. Fremling (2022c), K. Hinds et al. (2022a)
SN 2022aahy	⋯	⋯	0.135	06:58:56.24	+39:38:06.87	C. Fremling (2022d), K. Hinds et al. (2022c)
SN 2023adz	⋯	⋯	0.0500	11:32:37.72	+68:23:48.74	F. Forster et al. (2023), J. Sollerman et al. (2023a)
SN 2023awp	NGC 5936	Sc	0.0136	15:30:01.54	+12:59:15.56	C. Fremling (2023a), J. Sollerman et al. (2023b)
SN 2023erg	⋯	⋯	0.0670	15:30:05.64	+35:40:19.92	C. Fremling (2023b), Z. Delgado-González et al. (2023)
SN 2023iex	2MASX J21395531+2439332	⋯	0.0290	21:39:56.07	+24:39:34.67	C. Fremling (2023c), T. Kravstov et al. (2023)
SN 2023kqw	SDSS J143643.35+120523.8	⋯	0.0547	14:36:43.33	+12:05:24.26	A. Munoz-Arancibia et al. (2023a), K. Taggart (2023)
SN 2023meo	SDSS J143643.35+120523.8	⋯	0.0540	21:40:59.12	+24:00:26.28	J. Peloton et al. (2023), B. Godson et al. (2023)
SN 2023nof	2dFGRS TGS855Z331	⋯	0.0692	22:39:44.18	−15:50:04.38	A. Munoz-Arancibia et al. (2023b), C. Lidman et al. (2023)
SN 2023pfj	⋯	⋯	0.1110	02:17:12.15	+01:35:56.35	C. Fremling (2023d), P. Charalampopoulos (2023)
SN 2023usc	⋯	⋯	0.0600	05:21:31.65	+00:28:20.72	J. Tonry et al. (2023), M. A. Tucker (2023)

Table 6
(Continued)

SN Name	Host	Host Type	z	R.A. (J2000)	Decl. (J2000)	Reference
SN 2019uit	NGP9 F378–0626697	⋯	0.0710	12:50:16.09	+21:20:15.40	S. T. Hodgkin et al. (2019), M. R. Siebert et al. (2020a)
SN 2020jhs	⋯	⋯	0.0650	09:28:14.09	+25:40:13.30	J. Nordin et al. (2020a), A. Dahiwale & C. Fremling (2021b)
SN 2020qmj	LEDA 1280605	⋯	0.0220	00:44:06.006	+05:15:35.93	J. Nordin et al. (2020c), D. A. Perley et al. (2020c)
SN 2020tan	SDSS J010944.57+002024.3	⋯	0.0790	01:09:44.599	+00:20:24.93	D. O. Jones et al. (2020a), M. R. Siebert et al. (2020c)
SN 2020uaq	SDSS J153452.65+105839.1	⋯	0.1150	15:34:49.030	+10:58:37.34	D. O. Jones et al. (2020b), M. R. Siebert et al. (2021)
SN 2020utm	LEDA 1078124	⋯	0.0440	03:15:27.45	−03:00:38.19	D. O. Jones et al. (2020c), M. R. Siebert et al. (2020d)
SN 2020ybn	⋯	⋯	0.0960	06:11:02.260	−22:17:50.28	J. Tonry et al. (2020d), T. Hung (2020)
SN 2021bmv	⋯	⋯	0.0900	04:26:38.67	−11:53:45.72	J. Tonry et al. (2021f), C. Angus (2021)
SN 2021aapa	MCG-02–11–023	⋯	0.0320	22:04:24.170	−19:32:28.63	K. C. Chambers et al. (2021), K. W. Davis et al. (2021)
PTF 10abui	⋯	⋯	0.0516	06:12:18.46	−22:46:15.60	A. Nyholm et al. (2020)
PTF 10acsq	SDSS J080133.14+464553.0	⋯	0.1730	08:01:33.17	+46:45:52.50	A. Nyholm et al. (2020)
PTF 10cwl	⋯	⋯	0.0845	12:36:22.06	+07:47:38.00	A. J. Drake et al. (2010)
PTF 10cwx	2dFGRS TGN321Z210	⋯	0.0731	12:33:16.53	−00:03:10.60	A. Nyholm et al. (2020)
PTF 10ewc	⋯	⋯	0.0542	14:01:59.08	+33:50:11.60	A. Nyholm et al. (2020)
PTF 10fjh	UGC 10547	SAb	0.0321	16:46:55.36	+34:09:34.70	G. Duszanowicz (2010), P. Challis et al. (2010a)
PTF 10flx	WISEA J164658.92+642650.0	⋯	0.0674	16:46:58.28	+64:26:48.50	A. Nyholm et al. (2020)
PTF 10gvd	⋯	⋯	0.0693	16:53:02.12	+67:00:08.90	A. Nyholm et al. (2020)
PTF 10gvf	SDSS J111344.87+533749.6	⋯	0.0810	11:13:45.24	+53:37:44.90	A. Nyholm et al. (2020)
PTF 10oug	⋯	⋯	0.1501	17:20:44.79	+29:04:25.60	A. Nyholm et al. (2020)
PTF 10qwu	⋯	⋯	0.2259	16:51:10.36	+28:18:06.20	A. Nyholm et al. (2020)
PTF 10tel	A J172130+4807	⋯	0.0349	17:21:30.68	+48:0:47.40	O. Ofek (2012), D. A. Howell & D. Murray (2012)
PTF 10tyd	LEDA 1818789	⋯	0.0633	17:09:19.41	+27:49:08.60	A. Nyholm et al. (2020)
PTF 10weh	⋯	⋯	0.1379	17:26:50.46	+58:51:07.40	S. Ben-Ami et al. (2010)
PTF 11fzz	⋯	⋯	0.0813	11:10:46.68	+54:06:18.80	A. Nyholm et al. (2020)
PTF 11oxu	WISEA J033834.32+223242.7	⋯	0.0878	03:38:34.38	+22:32:59.40	A. J. Drake et al. (2011)
iPTF 13agz	SDSS J143432.09+250941.5	⋯	0.0572	14:34:32.12	+25:09:43.60	A. Nyholm et al. (2020)
iPTF 13asr	⋯	⋯	0.1543	12:47:28.61	+27:04:03.60	A. Nyholm et al. (2020)
iPTF 13cuf	⋯	⋯	0.2199	02:04:52.97	+14:37:59.70	I. Arcavi et al. (2013)
iPTF 14bpa	⋯	⋯	0.1220	15:26:59.96	+24:41:17.50	A. Nyholm et al. (2020)
iPTF 15aym	MCG+09–22–059	⋯	0.0334	13:26:26.67	+55:23:43.40	A. Nyholm et al. (2020)
iPTF 15bky	NGC 5837	S	0.0288	15:04:40.80	+12:37:43.40	D. C. Leonard et al. (2015)
iPTF 15blp	⋯	⋯	0.1949	16:27:15.21	+41:08:58.10	A. Nyholm et al. (2020)
iPTF 15eqr	WISEA J040115.10+331700.1	⋯	0.0467	04:01:15.67	+33:16:58.30	D. Young (2016)
iPTF 16fb	WISEA J102209.12+152822.4	⋯	0.0811	10:22:09.25	+15:28:19.20	K. C. Chambers et al. (2016b), T. Faran et al. (2016)
PSc 130812	⋯	⋯	0.0141	12:22:32.93	+47:19:48.36	V. Villar et al. (2019)
PSc 130942	⋯	⋯	0.0087	16:01:26.26	+55:14:25.80	V. Villar et al. (2019)
PSc 150582	⋯	⋯	0.0099	10:47:16.30	+59:01:26.04	V. Villar et al. (2019)
PSc 300140	⋯	⋯	0.0406	23:30:48.91	−01:12:26.64	V. Villar et al. (2019)
PSc 350633	⋯	⋯	0.0059	10:45:19.15	+59:04:54.84	V. Villar et al. (2019)
PSc 360030	⋯	⋯	0.0142	12:20:37.27	46:31:22.10	V. Villar et al. (2019)
PSc 430005	⋯	⋯	0.0564	22:17:39.86	+00:37:35.40	V. Villar et al. (2019)
PSc 450025	⋯	⋯	0.0237	02:23:33.53	−05:32:01.68	V. Villar et al. (2019)
PSc 450266	⋯	⋯	0.0259	08:40:55.46	+44:56:41.64	V. Villar et al. (2019)
PSc 460001	⋯	⋯	0.0077	03:33:04.15	−28:12:49.32	V. Villar et al. (2019)
PSc 480845	⋯	⋯	0.0135	12:29:08.59	+46:52:47.28	V. Villar et al. (2019)

Table 6
(Continued)

SN Name	Host	Host Type	z	R.A. (J2000)	Decl. (J2000)	Reference
PSc 500063	⋯	⋯	0.0118	12:25:06.67	+47:55:33.96	V. Villar et al. (2019)
PSc 530085	⋯	⋯	0.0661	22:12:43.46	−00:05:07.44	V. Villar et al. (2019)
PSc 550221	⋯	⋯	0.0243	02:21:52.39	−03:26:00.60	V. Villar et al. (2019)
PSc 580280	⋯	⋯	0.0074	03:32:54.12	−28:14:24.00	V. Villar et al. (2019)
PSc 580289	⋯	⋯	0.0373	02:28:34.32	−04:54:46.08	V. Villar et al. (2019)

Notes. These transients conform to the schema outlined in Section 3. This table shows the transient name, the host, discovery date, redshift, J2000 coordinates, and the source of the discovery/spectroscopic classification.

[a] As presented by C. L. Ransome et al. (2021).

(This table is available in machine-readable form in the online article.)

Table 7
SNe IIn Excluded from Our Sample

SN Name	Host	Host Type	z	R.A. (J2000)	Decl. (J2000)	References
SN 1987B	NGC 5850	No data	0.0085	15:07:02.92	01:30:13.20	E. M. Schlegel et al. (1996)
SN 1989R	UGC 2912	No data	0.0180	03:59:32.56	42:37:09.20	P. Challis[a]
SN 1993N	UGC 5695	No data	0.0098	10:29:46.33	13:01:14.00	C. L. Ransome et al. (2021)
SN 1994ak	NGC 2782	No data	0.0085	09:14:01.47	40:06:21.50	P. Garnavich et al. (1995)
SN 1995G	NGC 1643	No data	0.0160	04:43:44.26	−05:18:53.70	A. V. Filippenko & D. Schlegel (1995)
SN 1997eg	NGC 5012	No data	0.0087	13:11:36.73	22:55:29.40	A. V. Filippenko & A. J. Barth (1997)
SN 1999eb	NGC 664	No data	0.0180	01:43:45.45	04:13:25.90	M. Modjaz et al. (1999)
SN 1999el	NGC 6951	No data	0.0047	20:37:18.03	66:06:11.90	L. Cao et al. (1999)
SN 2000P	NGC 4965	No data	0.0075	13:07:10.53	−28:14:02.50	S. Jha et al. (2000)
SN 2000eo	MCG-02-09-03	No data	0.0100	03:09:08.17	−10:17:55.30	L. G. Strolger et al. (2000)
SN 2003G	IC 208	No data	0.0120	02:08:28.13	06:23:51.90	M. Hamuy & J. Maza (2003)
SN 2005gl	NGC 266	No data	0.0155	00:49:50.02	32:16:56.80	N. Blanc et al. (2005b)
SN 2005ip	NGC 2906	Long lived	0.0072	09:32:06.42	08:26:44.40	M. Modjaz et al. (2005)
SN 2005kj	A084009-0536	No data	0.0160	04:40:09.18	−05:36:02.20	C. Bonnaud et al. (2005)
SN 2006jd	UGC 4179	Long lived	0.0186	08:02:07.43	00:48:31.50	S. Blondin et al. (2006)
SN 2008J	MCG-02-07-33	Ia CSM	0.0159	02:34:24.20	−10:50:38.50	M. Stritzinger et al. (2008)
SN 2008S	NGC 6946	Imp?	0.0002	20:34:45.35	60:05:57.80	T. N. Steele et al. (2008)
SN 2009ip	NGC 7259	No data	0.0059	22:23:08.30	−28:56:52.40	W. Li et al. (2009)
SN 2009kn	MCG-03-21-06	No data	0.0143	08:09:43.04	−17:44:51.30	T. N. Steele et al. (2009)
SN 2010bt	NGC 7130	No data	0.0162	21:48:20.22	−34:57:16.50	N. Elias-Rosa[a]
SN 2010jl	UGC 5189A	Long lived	0.0107	09:42:53.33	09:29:41.80	M. Yamanaka et al. (2010)
SN 2010jp	A 061630-2124	No data	0.0092	06:16:30.63	−21:24:36.30	P. Challis et al. (2010b)
SN 2011A	NGC 4902	No data	0.0089	13:01:01.19	−14:31:34.80	M. Stritzinger et al. (2011)
SN 2011ht	UGC 5460	No data	0.0036	10:08:10.56	51:50:57.12	A. Pastorello et al. (2011)
SN 2012ca	ESO 336-G9	Ia CSM	0.0190	18:41:07.25	−41:47:38.40	C. Inserra et al. (2012)
SN 2013fc	ESO 154-G10	No data	0.0186	02:45:08.95	−55:44:27.30	E. Kankare et al. (2013)
SN 2013gc	ESO 430-G20	No data	0.0034	08:07:11.88	−28:03:26.30	A. Reguitti[a]
SN 2015da	NGC 5337	Long lived	0.0072	13:52:24.11	39:41:28.60	J. Zhang[a]
SN 2016bdu	⋯	No data	0.0170	13:10:13.95	32:31:14.07	N. Elias-Rosa[a]
SN 2018jdo	MCG+06-06-007	Short baseline	0.0390	02:17:48.70	+35:48:29.10	J. Tonry et al. (2018a), C. Fremling et al. (2018b)
SN 2019cac	2MASX J13504376-0230249	Spec	0.0467	13:50:43.89	−02:30:24.90	C. Fremling (2019b), J. Liang & J. Sollerman (2019)
SN 2019cqw	2MASX J09060852+6731212	Short baseline	0.0490	09:06:16.33	+67:30:50.1	J. Nordin et al. (2019g), M. A. Tucker et al. (2019a)
SN 2019ctt	⋯	Spec	0.0460	10:00:42.29	+12:02:23.40	J. Nordin et al. (2019h), M. A. Tucker et al. (2019a)
SN 2019dde	GAMA 50846	Spec	0.0570	14:28:12.03	−01:36:15.00	J. Nordin et al. (2019i), C. Fremling et al. (2019e)
SN 2019ejb	⋯	Spec	0.1180	14:08:28.58	+29:16:11.10	J. Tonry et al. (2019c)
SN 2019gjs	UGC 9634	Short baseline	0.0430	14:58:57.16	+20:03:10.50	K. C. Chambers et al. (2019b), A. Dugas et al. (2019c)
SN 2019mom	⋯	Short baseline	0.0488	01:55:36.52	+53:35:30.80	C. Fremling (2019c), A. Dahiwale et al. (2019)
SN 2019njv	2MASX J20195707+1522402	Short baseline	0.0146	20:19:57.19	+15:22:38.70	C. Fremling (2019d), A. Dahiwale & C. Fremling (2020d)
SN 2019smj	WISEA J074940.69+050411.1	Double peaked	0.0600	07:49:40.71	+05:04:27.10	F. Forster (2019c), C. Fremling et al. (2019i)
SN 2019tlv	⋯	Short baseline	0.0440	00:19:22.34	+21:46:32.9	K. C. Chambers et al. (2019c), A. Dahiwale & C. Fremling (2019)
SN 2019tpl	2MASX J01000084-0306377	Short baseline	0.0760	01:00:00.68	−03:06:30.20	J. Tonry et al. (2019d)
SN 2019wrt	WISEA J051648.34-072834.4	Short baseline	0.0573	05:16:47.98	−07:28:43.20	S. Reusch & R. Stein (2019), A. Dahiwale & C. Fremling (2020e)
SN 2019zrk	UGC 6625	Double peaked	0.0362	11:39:47.40	+19:55:46.70	K. De (2020), M. L. Graham et al. (2020b)
SN 2020acct	NGC 2981	Double peaked	0.0350	09:44:56.05	+31:05:45.70	C. Fremling (2020b), C. R. Angus et al. (2024)
SN 2020cn	⋯	Short Baseline	0.0770	21:28:10.73	+79:06:36.30	S. T. Hodgkin et al. (2020), L. Yan et al. (2020a)
SN 2020cke	WISEA J084717.88-203139.0	Short baseline	0.0350	08:47:17.91	−20:31:39.30	F. E. Bauer et al. (2020), A. Dahiwale & C. Fremling (2020f)
SN 2020hcr	2MASX J13542244-0521311	Spec	0.0510	13:54:22.59	−05:21:25.20	J. Tonry et al. (2020e); A. Dahiwale & C. Fremling (2020g)
SN 2020hfn	MCG-02-50-007	Short baseline	0.0249	19:48:47.98	−10:34:22.60	J. Tonry et al. (2020f), A. Dahiwale & C. Fremling (2020h)
SN 2020km	WISEA J043711.04+722725.6	Spec	0.1029	04:37:08.94	+72:27:37.00	J. Nordin et al. (2020d), L. Yan (2020)

Table 7
(Continued)

SN Name	Host	Host Type	z	R.A. (J2000)	Decl. (J2000)	References
SN 2020qmj	LEDA 1280605	Spec	0.0220	00:44:06.00	+05:15:35.80	J. Nordin et al. (2020c), D. A. Perley et al. (2020c)
SN 2020qpo	⋯	Spec	0.0530	17:16:41.36	+57:54:12.30	J. Nordin et al. (2020e), V. Quist et al. (2020)
SN 2020qyy	SDSS J155554.94+362451.7	Short baseline	0.0680	15:55:53.01	+36:24:35.40	J. Nordin et al. (2020f), A. Dahiwale & C. Fremling (2020i)
SN 2020xkx	⋯	Double peaked	0.0415	23:20:28.17	+22:59:12.80	J. Tonry et al. (2020g), M. Gromadzki et al. (2020b)
SN 2021cvd	UGC 8195	Short baseline	0.0230	13:06:23.22	+29:39:27.90	F. Forster et al. (2021e), F. Forster et al. (2021f)
SN 2021qqp	LEDA 1741591	Double peaked	0.0410	22:32:40.41	+25:34:34.80	K. De (2021c), M. Chu et al. (2021c)
SN 2022mgr	⋯	Spec	0.0680	18:32:37.01	+20:36:09.40	A. Munoz-Arancibia et al. (2022d), I. Perez-Fournon et al. (2022b)
SN 2022gzi	WISEA J174604.84 +421634.5	AGN?	0.0890	17:46:04.84	+42:16:34.50	A. Munoz-Arancibia et al. (2022c), D. Perley et al. (2022a)
SN 2022hev	2MASX J13143311-1025416	Short baseline	0.0540	13:14:36.72	−10:25:38.80	J. Tonry et al. (2022b)
SN 2022hsu	UGC 11946	Spec	0.0180	22:11:37.72	+46:18:40.00	C. Fremling (2022e), C. Ashall (2022)
SN 2022iaz	LEDA 860052	Spec	0.0670	12:30:31.31	−19:04:42.10	A. Munoz-Arancibia et al. (2022b)
SN 2022iep	LEDA 2164253	Spec	0.0250	16:29:41.96	+40:20:05.70	J. Tonry et al. (2022c), K. Hinds et al. (2022b)
SN 2020bwr	SDSS J163459.26+361227.7	Short baseline	0.0606	16:34:59.33	+36:12:27.43	K. Z. Stanek & C. S. Kochanek (2020), A. Do et al. (2020)
SN 2020noz	Z 42-125	Short baseline	0.0250	12:29:00.25	+07:50:58.42	D. O. Jones et al. (2020d), M. R. Siebert et al. (2020b)
SN 2020rdu	⋯	Spec	⋯	15:57:02.51	+24:34:50.72	K. C. Chambers et al. (2020b)
SN 2021xre	⋯	Spec	0.0600	00:15:07.19	+17:29:55.38	A. Munoz-Arancibia et al. (2021h), K. W. Davis et al. (2021)
PTF 09tm	2MASX J13465543 +6133179	Short baseline	0.0349	13:46:55.94	+61:33:15.60	A. Nyholm et al. (2020)
PTF 09uy	⋯	Short baseline	0.3135	12:43:55.80	+74:41:08.10	A. Nyholm et al. (2020)
PTF 09bcl	⋯	Short baseline	0.0621	18:06:26.78	+17:51:43.00	A. Nyholm et al. (2020)
PTF 10achk	2MASX J03055776-1031246	Short baseline	0.0325	03:05:57.54	−10:31:21.00	A. Nyholm et al. (2020)
PTF 10vag	⋯	Short baseline	0.0517	21:47:18.48	+18:07:51.5	A. Nyholm et al. (2020)
PTF 10xgo	⋯	Short baseline	0.0336	21:55:57.38	+01:19:14.10	A. Nyholm et al. (2020)
PTF 11mpg	SDSS J221736.67+003647.6	Spec	0.0933	22:17:36.66	+00:36:48.40	A. Nyholm et al. (2020)
PTF 11qnf	UGC 3344	Bumpy	0.0148	05:44:54.14	+69:09:06.90	A. Nyholm et al. (2020)
PTF 11qqj	WISEA J095801.73 +004315.2	Spec	0.0931	09:58:01.64	+00:43:14.70	A. Nyholm et al. (2020)
PTF 11rfr	⋯	Short baseline	0.0675	01:42:16.98	+29:16:25.70	A. Nyholm et al. (2020)
PTF 11rlv	WISEA J124934.15-092042.7	Short baseline	0.1323	12:49:34.04	−09:20:40.50	A. Nyholm et al. (2020)
PTF 12cxj	LEDA 2282052	Short baseline	0.0356	13:12:38.68	+46:29:06.30	A. Nyholm et al. (2020)
PTF 12frn	WISEA J162200.01 +320938.9	Short baseline	0.1365	16:22:00.16	+32:09:38.90	A. Nyholm et al. (2020)
PTF 12glz	⋯	Short baseline	0.0793	15:54:53.04	+03:32:08.50	A. Nyholm et al. (2020)
PTF 12ksy	⋯	Short baseline	0.0314	04:11:46.09	−12:28:00.80	A. Nyholm et al. (2020)
iPTF 13aki	⋯	Short baseline	0.1610	14:35:34.35	+38:38:31.00	A. Nyholm et al. (2020)
iPTF 14bcw	⋯	Short baseline	0.1206	13:48:41.18	+35:52:17.10	A. Nyholm et al. (2020)
PSc070763	⋯	⋯	0.0165	23:29:48.70	−00:17:29.80	V. Villar et al. (2019)
PSc110468	⋯	Short baseline	0.0179	10:00:45.53	02:01:24.20	V. Villar et al. (2019)
PSc120067	⋯	Short baseline	0.0071	10:56:21.02	57:39:55.40	V. Villar et al. (2019)
PSc360359	⋯	Spec	⋯	14:07:39.94	52:14:37.70	V. Villar et al. (2019)
PSc380012	⋯	Short baseline	0.0241	10:02:21.34	01:08:57.50	V. Villar et al. (2019)
PSc390712	⋯	Short baseline	0.0081	16:05:02.62	56:13:54.50	V. Villar et al. (2019)
PSc420248	⋯	Short baseline	0.0244	02:23:54.62	−03:36:47.90	V. Villar et al. (2019)
PSc580234	⋯	Short baseline	0.0253	10:03:44.64	02:45:47.90	V. Villar et al. (2019)

Notes. This table shows the transient name (survey name or IAU name), the reason why the transient was excluded from our sample, the J2000 coordinates, and the source of the discovery/spectroscopic classification.

[a] As presented in C. L. Ransome et al. (2021). Note that in this table, we report some objects as having “No data.” This means that there was no easily accessible public data, not necessarily that there is no photometric data existent in the literature.

(This table is available in machine-readable form in the online article.)

ORCID iDs

C. L. Ransome https://orcid.org/0000-0003-4175-4960
V. A. Villar https://orcid.org/0000-0002-5814-4061

References

Adams, S. M., Kochanek, C. S., Prieto, J. L., et al. 2016, MNRAS, 460, 1645
Aghakhanloo, M., Smith, N., Milne, P., et al. 2023a, MNRAS, 526, 456
Aghakhanloo, M., Smith, N., Milne, P., et al. 2023b, MNRAS, 521, 1941
Aleo, P. D., Engel, A. W., Narayan, G., et al. 2024, ApJ, 974, 172
Aleo, P. D., Malanchev, K., Sharief, S., et al. 2023, ApJS, 266, 9
Anderson, J. P., Habergham, S. M., James, P. A., & Hamuy, M. 2012, MNRAS, 424, 1372
Angus, C. 2021, TNSCR, 2021-649, 1
Angus, C. R., Woosley, S. E., Foley, R. J., et al. 2024, ApJL, 977, L41
Arbour, R. 2008, CBET, 1235, 2
Arcavi, I., Gal-Yam, A., Ofek, E., et al. 2013, ATel, 5407, 1
Arnett, W. D. 1980, ApJ, 237, 541
Arnett, W. D. 1982, ApJ, 253, 785
Ashall, C. 2022, TNSCR, 2022-1280, 1
Astropy Collaboration, Robitaille, T. P., Tollerud, E. J., et al. 2013, A&A, 558, A33
Bauer, F. E., Pignata, G., Forster, F., et al. 2020, TNSTR, 2020-466, 1
Beasor, E. R., Davies, B., Smith, N., et al. 2020, MNRAS, 492, 5994
Ben-Ami, S., Badenes, C., Kulkarni, S. R., et al. 2010, ATel, 2961, 1
Berger, E., Foley, R., & Ivans, I. 2009, ATel, 2184, 1
Bilinski, C., Smith, N., Williams, G. G., et al. 2024, MNRAS, 529, 1104
Blagorodnova, N., Neill, J. D., Walters, R., et al. 2018, PASP, 130, 035003
Blanc, N., Bongard, S., Copin, Y., et al. 2005a, ATel, 570, 1
Blanc, N., Bongard, S., Copin, Y., et al. 2005b, ATel, 630, 1
Blanchard, P. 2020, TNSCR, 2020-3730, 1
Blinnikov, S. I. 2010, PAN, 73, 604
Blondin, S., Calkins, M., Ayani, K., & Yamaoka, H. 2008, CBET, 1201, 1
Blondin, S., Modjaz, M., Kirshner, R., et al. 2006, CBET, 679, 1
Boian, I., & Groh, J. H. 2018, A&A, 617, A115
Bonnaud, C., Pecontal, E., Blanc, N., et al. 2005, CBET, 296, 1
Botticella, M. T., Pastorello, A., Smartt, S. J., et al. 2009, MNRAS, 398, 1041
Branch, D., & Wheeler, J. C. 2017, Supernova Explosions (Berlin: Springer)
Brennan, S. J., Fraser, M., Johansson, J., et al. 2022, MNRAS, 513, 5666
Brennan, S. J., Schulze, S., Lunnan, R., et al. 2023, A&A, 690, A259
Cao, L., Qiu, Y. L., Qiao, Q. Y., et al. 1999, IAUC, 7288, 1
Cardelli, J. A., Clayton, G. C., & Mathis, J. S. 1989, ApJ, 345, 245
Carini, R., Gutierrez, C., & Yaron, O. 2021, TNSCR, 2021-3519, 1
Cenko, S. B., Fox, D. B., Moon, D.-S., et al. 2006, PASP, 118, 1396
Challis, P., Foley, R. J., & Berlind, P. 2010a, CBET, 2243, 1
Challis, P., Kirshner, R., & Smith, N. 2010b, CBET, 2548, 1
Chambers, K. C., Boer, T. D., Bulger, J., et al. 2019a, TNSTR, 2019-1876, 1
Chambers, K. C., Boer, T. D., Bulger, J., et al. 2019b, TNSTR, 2019-898, 1
Chambers, K. C., Boer, T. D., Bulger, J., et al. 2019c, TNSTR, 2019-2199, 1
Chambers, K. C., Boer, T. D., Bulger, J., et al. 2020a, TNSTR, 2020-3077, 1
Chambers, K. C., Boer, T. D., Bulger, J., et al. 2020b, TNSTR, 2020-2461, 1
Chambers, K. C., Boer, T. D., Bulger, J., et al. 2021, TNSTR, 2021-3423, 1
Chambers, K. C., Boer, T. D., Bulger, J., et al. 2022, TNSTR, 2022-2024, 1
Chambers, K. C., Huber, M. E., Flewelling, H., et al. 2016b, TNSTR, 2016-116, 1
Chambers, K. C., Magnier, E. A., Metcalfe, N., et al. 2016a, arXiv:1612.05560
Chandra, P., Chevalier, R. A., Chugai, N., et al. 2012, ApJ, 755, 110
Chandra, P., Chevalier, R. A., James, N. J. H., & Fox, O. D. 2022a, MNRAS, 517, 4151
Chandra, P., Chevalier, R. A., James, N. J. H., & Fox, O. D. 2022b, MNRAS, 517, 4151
Charalampopoulos, P. 2023, TNSCR, 2023-2094, 1
Chatzopoulos, E., Wheeler, J. C., & Vinko, J. 2012, ApJ, 746, 121
Chevalier, R. A. 1982, ApJ, 258, 790
Chevalier, R. A. 2012, ApJL, 752, L2
Chevalier, R. A., & Irwin, C. M. 2011, ApJL, 729, L6
Chiba, R., & Moriya, T. J. 2024, ApJ, 973, 14
Chu, M., Dahiwale, A., & Fremling, C. 2021a, TNSCR, 2021-3031, 1
Chu, M., Dahiwale, A., & Fremling, C. 2021b, TNSCR, 2021-3134, 1
Chu, M., Dahiwale, A., & Fremling, C. 2021c, TNSCR, 2021-2605, 1
Chugai, N. N. 1991, MNRAS, 250, 513
Chugai, N. N. 2001, MNRAS, 326, 1448
Chugai, N. N. 2016, AstL, 42, 82
Chugai, N. N., Blinnikov, S. I., Cumming, R. J., et al. 2004, MNRAS, 352, 1213
Chugai, N. N., & Danziger, I. J. 1994, MNRAS, 268, 173
Chugai, N. N., Danziger, I. J., & Della Valle, M. 1995, MNRAS, 276, 530
Clocchiatti, A., Garcia-Lopez, R., Barker, E. S., et al. 1994, IAUC, 6065, 1
Cold, C., & Hjorth, J. 2023, A&A, 670, A48
Colgate, S. A., & McKee, C. 1969, ApJ, 157, 623
Coulter, D. A., Jones, D. O., McGill, P., et al. 2023, PASP, 135, 064501
Cox, P., Mezger, P. G., Sievers, A., et al. 1995, A&A, 297, 168
Dahiwale, A., Dugas, A., & Fremling, C. 2019, TNSCR, 2019-1505, 1
Dahiwale, A., & Fremling, C. 2019, TNSCR, 2019-2230, 1
Dahiwale, A., & Fremling, C. 2020a, TNSCR, 2020-601, 1
Dahiwale, A., & Fremling, C. 2020b, TNSCR, 2020-1176, 1
Dahiwale, A., & Fremling, C. 2020c, TNSCR, 2020-3192, 1
Dahiwale, A., & Fremling, C. 2020d, TNSCR, 2020-1667, 1
Dahiwale, A., & Fremling, C. 2020e, TNSCR, 2020-1573, 1
Dahiwale, A., & Fremling, C. 2020f, TNSCR, 2020-808, 1
Dahiwale, A., & Fremling, C. 2020g, TNSCR, 2020-1114, 1
Dahiwale, A., & Fremling, C. 2020h, TNSCR, 2020-1756, 1
Dahiwale, A., & Fremling, C. 2020i, TNSCR, 2020-2576, 1
Dahiwale, A., & Fremling, C. 2021a, TNSCR, 2021-1501, 1
Dahiwale, A., & Fremling, C. 2021b, TNSCR, 2021-1501, 1
Dahiwale, A., & Fremling, C. 2021c, TNSCR, 2021-358, 1
Dahiwale, A., & Fremling, C. 2021d, TNSCR, 2021-223, 1
Dahiwale, A., & Fremling, C. 2021e, TNSCR, 2021-223, 1
Dahiwale, A., & Fremling, C. 2021f, TNSCR, 2021-1344, 1
Davis, K. 2021, TNSCR, 2021-3592, 1
Davis, K. W., Siebert, M. R., Rojas-Bravo, C., et al. 2021, TNSCR, 2021-3046, 1
De, K. 2019, TNSTR, 2019-2591, 1
De, K. 2020, TNSTR, 2020-33, 1
De, K. 2021a, TNSTR, 2021-367, 1
De, K. 2021b, TNSTR, 2021-2632, 1
De, K. 2021c, TNSTR, 2021-2150, 1
de Jager, C., Nieuwenhuijzen, H., & van der Hucht, K. A. 1988, A&AS, 72, 259
de Soto, K. M., Villar, V. A., Berger, E., et al. 2024, ApJ, 974, 169
Deckers, M., Dimitriadis, G., Terwel, J., Harvey, L., & Yaron, O. 2021, TNSCR, 2021-3182, 1
Delgado, A., Harrison, D., Hodgkin, S., et al. 2019, TNSTR, 2019-169, 1
Delgado-González, Z., Poidevin, F., Pérez-Fournon, I., et al. 2023, TNSCR, 2023-929, 1
Dessart, L. 2024, arXiv:2405.04259
Dessart, L., Audit, E., & Hillier, D. J. 2015, MNRAS, 449, 4304
Dessart, L., & Hillier, D. J. 2022, A&A, 660, L9
Dessart, L., Hillier, D. J., Gezari, S., Basa, S., & Matheson, T. 2009, MNRAS, 394, 21
Dessart, L., Livne, E., & Waldman, R. 2010, MNRAS, 405, 2113
Di Carlo, E., Massi, F., Valentini, G., et al. 2002, ApJ, 573, 144
Dickinson, D., Smith, N., Andrews, J. E., et al. 2024, MNRAS, 527, 7767
Do, A., Tucker, M. A., Payne, A. V., et al. 2020, TNSCR, 2020-607, 1
Dong, Y., Sand, D. J., Valenti, S., et al. 2023, ApJ, 957, 28
Dopita, M. A., & Ryder, S. D. 1990, IAUC, 4950, 3
Drake, A. J., Djorgovski, S. G., Graham, M. J., et al. 2011, CBET, 2948, 1
Drake, A. J., Djorgovski, S. G., Mahabal, A. A., et al. 2010, ATel, 2555, 1
Drout, R. M. 2016, PhD thesis, Harvard Univ.
Dugas, A., Fremling, C., & Sharma, Y. 2019a, TNSCR, 2019-1402, 1
Dugas, A., Fremling, C., & Sharma, Y. 2019b, TNSCR, 2019-1215, 1
Dugas, A., Fremling, C., & Sharma, Y. 2019c, TNSCR, 2019-1420, 1
Dukiya, N., Gangopadhyay, A., Misra, K., et al. 2024, ApJ, 976, 86
Duszanowicz, G. 2010, CBET, 2241, 1
Dwek, E., Arendt, R. G., Fox, O. D., et al. 2017, ApJ, 847, 91
Elias-Rosa, N., Brennan, S. J., Benetti, S., et al. 2024, A&A, 686, A13
Elias-Rosa, N., Pastorello, A., Benetti, S., et al. 2016, MNRAS, 463, 3894
Ercolino, A., Jin, H., Langer, N., & Dessart, L. 2024, A&A, 685, A58
Faran, T., Kromer, M., Taubenberger, S., & Yaron, O. 2016, TNSCR, 2016-121, 1
Farias, D., Gall, C., Narayan, G., et al. 2024, ApJ, 977, 152
Fassia, A., Meikle, W. P. S., Chugai, N., et al. 2001, MNRAS, 325, 907
Filippenko, A. V. 1989, AJ, 97, 726
Filippenko, A. V. 1997, ARA&A, 35, 309
Filippenko, A. V., & Barth, A. J. 1997, IAUC, 6794, 1
Filippenko, A. V., Barth, A. J., Bower, G. C., et al. 1995, AJ, 110, 2261
Filippenko, A. V., & Schlegel, D. 1995, IAUC, 6139, 2
Foley, R. J., Berger, E., Fox, O., et al. 2011, ApJ, 732, 32
Foley, R. J., Li, W., Moore, M., et al. 2006, CBET, 695, 1
Forster, F. 2019a, TNSTR, 2019-1897, 1
Forster, F. 2019b, TNSTR, 2019-2126, 1
Forster, F. 2019c, TNSTR, 2019-2069, 1
Forster, F., Bauer, F. E., Galbany, L., et al. 2020a, TNSTR, 2020-1027, 1

Forster, F., Bauer, F. E., Galbany, L., et al. 2020b, TNSTR, 2020-2513, 1
Forster, F., Bauer, F. E., Munoz-Arancibia, A., et al. 2020c, TNSTR, 2020-3183, 1
Forster, F., Bauer, F. E., Munoz-Arancibia, A., et al. 2020d, TNSTR, 2020-3437, 1
Forster, F., Bauer, F. E., Munoz-Arancibia, A., et al. 2021a, TNSTR, 2021-708, 1
Forster, F., Bauer, F. E., Munoz-Arancibia, A., et al. 2021b, TNSTR, 2021-1237, 1
Forster, F., Bauer, F. E., Munoz-Arancibia, A., et al. 2021c, TNSTR, 2021-1413, 1
Forster, F., Bauer, F. E., Munoz-Arancibia, A., et al. 2021d, TNSTR, 2021-2884, 1
Forster, F., Bauer, F. E., Munoz-Arancibia, A., et al. 2021e, TNSTR, 2021-452, 1
Forster, F., Bauer, F. E., Munoz-Arancibia, A., et al. 2021f, TNSTR, 2021-452, 1
Forster, F., Bauer, F. E., Pignata, G., et al. 2019, TNSTR, 2019-2587, 1
Forster, F., Bauer, F. E., Pignata, G., et al. 2021g, TNSTR, 2021-991, 1
Forster, F., Bauer, F. E., Pignata, G., et al. 2022a, TNSTR, 2022-1691, 1
Forster, F., Bauer, F. E., Pignata, G., et al. 2022b, TNSTR, 2022-1855, 1
Forster, F., Hernandez-Garcia, L., Munoz-Arancibia, A., et al. 2020e, TNSTR, 2020-2801, 1
Forster, F., Pignata, G., Bauer, F. E., et al. 2021h, TNSTR, 2021-1414, 1
Forster, F., Pignata, G., Bauer, F. E., et al. 2023, TNSTR, 2023-156, 1
Fox, O. D., Chevalier, R. A., Skrutskie, M. F., et al. 2011, ApJ, 741, 7
Fox, O. D., Dyk, S. D. V., Dwek, E., et al. 2017, ApJ, 836, 222
Fox, O. D., Filippenko, A. V., Skrutskie, M. F., et al. 2013, AJ, 146, 2
Fox, O. D., Fransson, C., Smith, N., et al. 2020, MNRAS, 498, 517
Fox, O. D., Silverman, J. M., Filippenko, A. V., et al. 2015, MNRAS, 447, 772
Fransson, C., Ergon, M., Challis, P. J., et al. 2014, ApJ, 797, 118
Fransson, C., Sollerman, J., Strotjohann, N. L., et al. 2022, A&A, 666, A79
Fraser, M., Magee, M., Kotak, R., et al. 2013, ApJL, 779, L8
Fremling, C. 2019a, TNSTR, 2019-988, 1
Fremling, C. 2019b, TNSTR, 2019-414, 1
Fremling, C. 2019c, TNSTR, 2019-1418, 1
Fremling, C. 2019d, TNSTR, 2019-1485, 1
Fremling, C. 2020a, TNSTR, 2020-97, 1
Fremling, C. 2020b, TNSTR, 2020-3738, 1
Fremling, C. 2021a, TNSTR, 2021-1028, 1
Fremling, C. 2021b, TNSTR, 2021-2149, 1
Fremling, C. 2021c, TNSTR, 2021-2377, 1
Fremling, C. 2022a, TNSTR, 2022-2343, 1
Fremling, C. 2022b, TNSTR, 2022-2569, 1
Fremling, C. 2022c, TNSTR, 2022-3285, 1
Fremling, C. 2022d, TNSTR, 2022-3310, 1
Fremling, C. 2022e, TNSTR, 2022-1010, 1
Fremling, C. 2023a, TNSTR, 2023-217, 1
Fremling, C. 2023b, TNSTR, 2023-738, 1
Fremling, C. 2023c, TNSTR, 2023-1085, 1
Fremling, C. 2023d, TNSCR, 2023-1940, 1
Fremling, C., Dahiwale, A., & Dugas, A. 2019a, TNSCR, 2019-1864, 1
Fremling, C., Dugas, A., & Sharma, Y. 2018a, TNSCR, 2018-1221, 1
Fremling, C., Dugas, A., & Sharma, Y. 2018b, TNSCR, 2018-1886, 1
Fremling, C., Dugas, A., & Sharma, Y. 2019b, TNSCR, 2019-188, 1
Fremling, C., Dugas, A., & Sharma, Y. 2019c, TNSCR, 2019-747, 1
Fremling, C., Dugas, A., & Sharma, Y. 2019d, TNSCR, 2019-1193, 1
Fremling, C., Dugas, A., & Sharma, Y. 2019e, TNSCR, 2019-581, 1
Fremling, C., Miller, A. A., Sharma, Y., et al. 2020a, ApJ, 895, 32
Fremling, C., Sharma, Y., & Dahiwale, A. 2019f, TNSCR, 2019-2297, 1
Fremling, C., Sharma, Y., & Dahiwale, A. 2019g, TNSCR, 2019-2297, 1
Fremling, C., Sharma, Y., & Dahiwale, A. 2019h, TNSCR, 2019-2297, 1
Fremling, C., Sharma, Y., & Dahiwale, A. 2019i, TNSCR, 2019-2297, 1
Fremling, C., Sharma, Y., & Dahiwale, A. 2020a, TNSCR, 2020-1757, 1
Fukugita, M., Nakamura, O., Turner, E. L., Helmboldt, J., & Nichol, R. C. 2004, ApJL, 601, L127
Fuller, J., & Tsuna, D. 2024, OJAp, 7, 47
Gal-Yam, A., & Leonard, D. C. 2009, Natur, 458, 865
Gal-Yam, A., Leonard, D. C., Fox, D. B., et al. 2007, ApJ, 656, 372
Galbany, L., Anderson, J. P., Sánchez, S. F., et al. 2018, ApJ, 855, 107
Garnavich, P., Challis, P., Riess, A., Kirshner, R., & Berlind, P. 1995, IAUC, 6124, 3
Godson, B., Warwick, B., O'Neill, D., et al. 2023, TNSCR, 2023-2000, 1
Goldman, S. R., van Loon, J. T., Zijlstra, A. A., et al. 2017, MNRAS, 465, 403
Gomez, S., Hosseinzadeh, G., Berger, E., & Blanchard, P. 2020, TNSCR, 2020-569, 1
Gomez, S., Hosseinzadeh, G., Berger, E., & Blanchard, P. 2021, TNSCR, 2021-2719, 1
Goodrich, R. W., Stringfellow, G. S., Penrod, G. D., & Filippenko, A. V. 1989, ApJ, 342, 908
Graham, M. L., Dahiwale, A., & Fremling, C. 2020a, TNSCR, 2020-348, 1
Graham, M. L., Dahiwale, A., & Fremling, C. 2020b, TNSCR, 2020-535, 1
Green, G. M., Schlafly, E. F., Finkbeiner, D., et al. 2018, MNRAS, 478, 651
Gromadzki, M., Ihanec, N., Callis, E., Fraser, M., & Irani, I. 2020a, TNSCR, 2020-3382, 1
Gromadzki, M., Ihanec, N., Callis, E., & Yaron, O. 2020b, TNSCR, 2020-3243, 1
Guillochon, J., Parrent, J., Kelley, L. Z., & Margutti, R. 2017, ApJ, 835, 64
Gutierrez, C., Kravtsov, T., & Bruch, R. J. 2022, TNSCR, 2022-2488, 1
Habergham, S. M., Anderson, J. P., James, P. A., & Lyman, J. D. 2014, MNRAS, 441, 2230
Hamuy, M., & Maza, J. 2003, IAUC, 8045, 2
Hamuy, M., Phillips, M., Suntzeff, N., & Maza, J. 2003, IAUC, 8151, 2
Heger, A., Fryer, C. L., Woosley, S. E., Langer, N., & Hartmann, D. H. 2003, ApJ, 591, 288
Heger, A., Jeannin, L., Langer, N., & Baraffe, I. 1997, A&A, 327, 224
Helou, G., & Madore, B. 1988, in ESO Conf. Workshop Proc. 28 (Garching: ESO), 335
Hillier, D. J., Davidson, K., Ishibashi, K., & Gull, T. 2001, ApJ, 553, 837
Hinds, K., & Perley, D. 2022, TNSCR, 2022-1912, 1
Hinds, K., Perley, D., Chu, M., Dahiwale, A., & Fremling, C. 2022a, TNSCR, 2022-3438, 1
Hinds, K., Perley, D., Chu, M., Dahiwale, A., & Fremling, C. 2022b, TNSCR, 2022-1302, 1
Hinds, K., Wise, J., & Perley, D. 2022c, TNSCR, 2022-3621, 1
Hinkle, J. 2021, TNSCR, 2021-2645, 1
Hiramatsu, D., Berger, E., Gomez, S., et al. 2024a, arXiv:2411.07287
Hiramatsu, D., Howell, D. A., Van Dyk, S. D., et al. 2021, NatAs, 5, 903
Hiramatsu, D., Matsumoto, T., Berger, E., et al. 2024b, ApJ, 964, 181
Hodgkin, S. T., Breedt, E., Delgado, A., et al. 2019, TNSCR, 2019-2300, 1
Hodgkin, S. T., Breedt, E., Delgado, A., et al. 2020, TNSCR, 2020-30, 1
Hosseinzadeh, G., Dauphin, F., Villar, V. A., et al. 2020, ApJ, 905, 93
Hosseinzadeh, G., Gomez, S., Berger, E., & Blanchard, P. 2021, TNSCR, 2021-2441, 1
Howell, D. A., & Murray, D. 2012, CBET, 3313, 2
Huang, C., & Chevalier, R. A. 2018, MNRAS, 475, 1261
Huber, M. E. 2022, TNSCR, 2022-2065, 1
Humphreys, R. M., & Davidson, K. 1994, PASP, 106, 1025
Humphreys, R. M., Davidson, K., Jones, T. J., et al. 2012, ApJ, 760, 93
Humphreys, R. M., Davidson, K., Van Dyk, S. D., & Gordon, M. S. 2017, ApJ, 848, 86
Hung, T. 2020, TNSCR, 2020-3431, 1
Ibik, A. L., Drout, M. R., Margutti, R., et al. 2025, ApJ, 979, 16
Inserra, C., Fraser, M., Smartt, S. J., et al. 2016, MNRAS, 459, 2721
Inserra, C., Smartt, S. J., Valenti, S., et al. 2012, CBET, 3101, 2
Irani, I., Prentice, S. J., Schulze, S., et al. 2022, ApJ, 927, 10
Irani, I., Zimmerman, E., Schulze, S., et al. 2020, TNSCR, 2020-223, 1
Ivezić, Ž., Kahn, S. M., Tyson, J. A., et al. 2019, ApJ, 873, 111
Jacobson-Galán, W. V., Dessart, L., Davis, K. W., et al. 2024, ApJ, 970, 189
Jacobson-Galán, W. V., Dessart, L., Jones, D. O., et al. 2022, ApJ, 924, 15
Jaeger, T. D. 2022, TNSCR, 2022-2129, 1
Jerkstrand, A., Maeda, K., & Kawabata, K. S. 2020, Sci, 367, 415
Jha, S., Challis, P., Kirshner, R., & Berlind, P. 2000, IAUC, 7381, 2
Jiang, B., Jiang, S., & Ashley Villar, V. 2020, RNAAS, 4, 16
Jones, D. O., Foley, R. J., Narayan, G., et al. 2021, ApJ, 908, 143
Jones, D. O., French, K. D., Agnello, A., et al. 2020a, TNSTR, 2020-2784, 1
Jones, D. O., French, K. D., Agnello, A., et al. 2020b, TNSTR, 2020-2913, 1
Jones, D. O., French, K. D., Agnello, A., et al. 2020c, TNSTR, 2020-3018, 1
Jones, D. O., French, K. D., Agnello, A., et al. 2020d, TNSTR, 2020-1958, 1
Jones, D. O., French, K. D., Agnello, A., et al. 2022, TNSTR, 2022-3089, 1
Justham, S., Podsiadlowski, P., & Vink, J. S. 2014, ApJ, 796, 121
Kangas, T., Portinari, L., Mattila, S., et al. 2017, A&A, 597, A92
Kankare, E., Ergon, M., Bufano, F., et al. 2012, MNRAS, 424, 855
Kankare, E., Kangas, T., Inserra, C., et al. 2013, ATel, 5338, 1
Kashi, A., & Soker, N. 2010, ApJ, 723, 602
Kashi, A., Soker, N., & Moskovitz, N. 2013, MNRAS, 436, 2484
Kasliwal, M. M., Cenko, S. B., Kulkarni, S. R., et al. 2011, ApJ, 735, 94
Katsuda, S., Maeda, K., Nozawa, T., Pooley, D., & Immler, S. 2013, ApJ, 780, 184
Kessler, R., Narayan, G., Avelino, A., et al. 2019, PASP, 131, 094501
Khatami, D. K., & Kasen, D. N. 2024, ApJ, 972, 140
Khazov, D., Yaron, O., Gal-Yam, A., et al. 2016, ApJ, 818, 3
Kiewe, M., Gal-Yam, A., Arcavi, I., et al. 2012, ApJ, 744, 10
Kilpatrick, C. D., Foley, R. J., Drout, M. R., et al. 2018, MNRAS, 473, 4805
Kochanek, C. S., Szczygieł, D. M., & Stanek, K. Z. 2012, ApJ, 758, 142
Kotak, R., & Vink, J. S. 2006, A&A, 460, L5
Kravstov, T., Hueichapan, E., Wiseman, P., & Yaron, O. 2023, TNSCR, 2023-1334, 1
Langer, N. 2012, ARA&A, 50, 107

Leonard, D. C., Sheehan, P., McCarthy, D., et al. 2015, ATel, 7690, 1
Li, W., Leaman, J., Chornock, R., et al. 2011, MNRAS, 412, 1441
Li, W., Smith, N., Miller, A. A., & Filippenko, A. V. 2009, ATel, 2212, 1
Liang, J., & Sollerman, J. 2019, TNSCR, 2019-1139, 1
Lidman, C., Martin, B., Brout, D., et al. 2023, TNSCR, 2023-1786, 1
LSST Science Collaboration, Abell, P. A., Allison, J., et al. 2009, arXiv:0912.0201
Mahy, L., Lanthermann, C., Hutsemékers, D., et al. 2022, A&A, 657, A4
Malmquist, K. G. 1922, MeLuF, 100, 1
Margutti, R., Kamble, A., Milisavljevic, D., et al. 2017, ApJ, 835, 140
Matsumoto, T., & Metzger, B. D. 2022, ApJ, 936, 114
Matsuoka, T., & Sawada, R. 2024, ApJ, 963, 105
Matzner, C. D., & McKee, C. F. 1999, ApJ, 510, 379
Mauerhan, J., & Smith, N. 2012, MNRAS, 424, 2659
Mauerhan, J. C., Smith, N., Filippenko, A. V., et al. 2013, MNRAS, 430, 1801
Maund, J. R., Smartt, S. J., Kudritzki, R. P., et al. 2006, MNRAS, 369, 390
Modjaz, M., Kirshner, R., Challis, P., & Calkins, M. 2005, IAUC, 8628, 2
Modjaz, M., Li, W. D., Garnavich, P., et al. 1999, IAUC, 7268, 1
Moran, S., Fraser, M., Kotak, R., et al. 2023, A&A, 669, A51
Moriya, T. J. 2023, MNRAS, 524, 5309
Moriya, T. J., Blinnikov, S. I., Tominaga, N., et al. 2012, MNRAS, 428, 1020
Moriya, T. J., Blinnikov, S. I., Tominaga, N., et al. 2013, MNRAS, 428, 1020
Moriya, T. J., Galbany, L., Jiménez-Palau, C., et al. 2023, A&A, 677, A20
Moriya, T. J., Maeda, K., Taddia, F., et al. 2013, MNRAS, 435, 1520
Moriya, T. J., Maeda, K., Taddia, F., et al. 2014, MNRAS, 439, 2917
Moriya, T. J., Sorokina, E. I., & Chevalier, R. A. 2018, SSRv, 214, 59
Moriya, T. J., Yoon, S.-C., Gräfener, G., & Blinnikov, S. I. 2017, MNRAS, 469, L108
Morozova, V., Piro, A. L., & Valenti, S. 2017, ApJ, 838, 28
Munoz-Arancibia, A., Forster, F., Bauer, F. E., et al. 2020a, TNSTR, 2020-3475, 1
Munoz-Arancibia, A., Forster, F., Bauer, F. E., et al. 2020b, TNSTR, 2020-3535, 1
Munoz-Arancibia, A., Forster, F., Bauer, F. E., et al. 2021a, TNSTR, 2021-342, 1
Munoz-Arancibia, A., Forster, F., Bauer, F. E., et al. 2021b, TNSTR, 2021-733, 1
Munoz-Arancibia, A., Forster, F., Bauer, F. E., et al. 2021c, TNSTR, 2021-1392, 1
Munoz-Arancibia, A., Forster, F., Bauer, F. E., et al. 2021d, TNSTR, 2021-1465, 1
Munoz-Arancibia, A., Forster, F., Bauer, F. E., et al. 2021e, TNSTR, 2021-1900, 1
Munoz-Arancibia, A., Forster, F., Bauer, F. E., et al. 2021f, TNSTR, 2021-3056, 1
Munoz-Arancibia, A., Forster, F., Bauer, F. E., et al. 2021g, TNSTR, 2021-3190, 1
Munoz-Arancibia, A., Forster, F., Bauer, F. E., et al. 2021h, TNSTR, 2021-3004, 1
Munoz-Arancibia, A., Forster, F., Bauer, F. E., et al. 2022a, TNSTR, 2022-1166, 1
Munoz-Arancibia, A., Forster, F., Bauer, F. E., et al. 2022b, TNSTR, 2022-1028, 1
Munoz-Arancibia, A., Forster, F., Bauer, F. E., et al. 2022c, TNSTR, 2022-2109, 1
Munoz-Arancibia, A., Forster, F., Pignata, G., et al. 2023a, TNSTR, 2023-1385, 1
Munoz-Arancibia, A., Bauer, F. E., Forster, F., et al. 2022b, TNSTR, 2022-1568, 1
Munoz-Arancibia, A., Bauer, F. E., Forster, F., et al. 2022c, TNSTR, 2022-914, 1
Munoz-Arancibia, A., Pignata, G., Bauer, F. E., et al. 2022d, TNSTR, 2022-1579, 1
Munoz-Arancibia, A., Pignata, G., Forster, F., et al. 2023b, TNSTR, 2023-1714, 1
Munoz-Sanchez, G., Kalitsounaki, M., de Wit, S., et al. 2024, arXiv:2411.19329
Najarro, F. 2001, in ASP Conf. Ser. 233, P Cygni 2000: 400 Years of Progress, ed. M. de Groot & C. Sterken (San Francisco, CA: ASP), 133
Nicholl, M., Blanchard, P. K., Berger, E., et al. 2020, NatAs, 4, 893
Niu, Z., Sun, N.-C., & Liu, J. 2024, ApJL, 966, L20
Nordin, J., Brinnel, V., Giomi, M., et al. 2018a, TNSTR, 2018-1958, 1
Nordin, J., Brinnel, V., Giomi, M., et al. 2018b, TNSTR, 2018-1997, 1
Nordin, J., Brinnel, V., Giomi, M., et al. 2019a, TNSTR, 2019-404, 1
Nordin, J., Brinnel, V., Giomi, M., et al. 2019b, TNSTR, 2019-623, 1
Nordin, J., Brinnel, V., Giomi, M., et al. 2019c, TNSTR, 2019-1174, 1
Nordin, J., Brinnel, V., Giomi, M., et al. 2019d, TNSTR, 2019-1287, 1
Nordin, J., Brinnel, V., Giomi, M., et al. 2019e, TNSTR, 2019-74, 1
Nordin, J., Brinnel, V., Giomi, M., et al. 2019f, TNSTR, 2019-2439, 1
Nordin, J., Brinnel, V., Giomi, M., et al. 2019g, TNSTR, 2019-486, 1
Nordin, J., Brinnel, V., Giomi, M., et al. 2019h, TNSTR, 2019-502, 1
Nordin, J., Brinnel, V., Giomi, M., et al. 2019i, TNSTR, 2019-1258, 1
Nordin, J., Brinnel, V., Giomi, M., et al. 2020a, TNSTR, 2020-1279, 1
Nordin, J., Brinnel, V., Giomi, M., et al. 2020b, TNSTR, 2020-105, 1
Nordin, J., Brinnel, V., Giomi, M., et al. 2020c, TNSTR, 2020-2340, 1
Nordin, J., Brinnel, V., Giomi, M., et al. 2020d, TNSTR, 2020-62, 1
Nordin, J., Brinnel, V., Giomi, M., et al. 2020e, TNSTR, 2020-2359, 1
Nordin, J., Brinnel, V., Giomi, M., et al. 2020f, TNSTR, 2020-2436, 1
Nordin, J., Brinnel, V., Santen, J. V., et al. 2021a, TNSTR, 2021-2097, 1
Nordin, J., Brinnel, V., Santen, J. V., et al. 2021b, TNSTR, 2021-2214, 1
Nordin, J., Brinnel, V., Santen, J. V., et al. 2021c, TNSCR, 2021-3057, 1
Nyholm, A., Sollerman, J., Taddia, F., et al. 2017, A&A, 605, A6
Nyholm, A., Sollerman, J., Tartaglia, L., et al. 2020, A&A, 637, A73
Ofek, E. O., Arcavi, I., Tal, D., et al. 2014a, ApJ, 788, 154
Ofek, E. O., Sullivan, M., Shaviv, N. J., et al. 2014b, ApJ, 789, 104
Ofek, E. O., Zoglauer, A., Boggs, S. E., et al. 2014c, ApJ, 781, 42
Ofek, O. 2012, CBET, 3313, 1
Ohnaka, K., Hofmann, K. H., Weigelt, G., et al. 2024, A&A, 691, L15
Oliphant, T. 2006, NumPy: A guide to NumPy (USA: Trelgol Publishing) http://www.numpy.org/
pandas development team, 2020 pandas-dev/pandas: Pandas, latest, Zenodo doi:10.5281/zenodo.3509134
Pastorello, A., Cappellaro, E., Inserra, C., et al. 2013, ApJ, 767, 1
Pastorello, A., Stanishev, V., Smartt, S. J., Fraser, M., & Lindborg, M. 2011, CBET, 2851, 2
Payne, A. V., Tucker, M. A., Do, A., Shappee, B. J., & Huber, M. E. 2019, TNSCR, 2019-97, 1
Pearson, K. 1907, Natur, 76, 613
Pedregosa, F., Varoquaux, G., Gramfort, A., et al. 2011, JMLR, 12, 2825
Pellegrino, C., Li, W., Burke, J., et al. 2022, TNSCR, 2022-1677, 1
Peloton, J., Moller, A., & Ishida, E. E. O. 2023, TNSTR, 2023-1535, 1
Perez-Fournon, I., Angel, C. J., Poidevin, F., et al. 2022a, TNSCR, 2022-1626, 1
Perez-Fournon, I., Poidevin, F., Angel, C. J., et al. 2022b, TNSCR, 2022-1652, 1
Perley, D. 2019, TNSCR, 2019-2724, 1
Perley, D. 2020, TNSCR, 2020-3827, 1
Perley, D. 2021a, TNSCR, 2021-450, 1
Perley, D. 2021b, TNSCR, 2021-1071, 1
Perley, D. 2021c, TNSCR, 2021-1355, 1
Perley, D. 2021d, TNSCR, 2021-1786, 1
Perley, D. 2021e, TNSCR, 2021-2305, 1
Perley, D. 2021f, TNSCR, 2021-3472, 1
Perley, D., Chu, M., Dahiwale, A., & Fremling, C. 2022a, TNSCR, 2022-1478, 1
Perley, D., Chu, M., Hinds, K. R., & Fremling, C. 2022b, TNSCR, 2022-2174, 1
Perley, D., & Hinds, K. 2022, TNSCR, 2022-1479, 1
Perley, D. A., Dahiwale, A., & Fremling, C. 2021, TNSCR, 2021-2239, 1
Perley, D. A., Fremling, C., Sollerman, J., et al. 2020a, ApJ, 904, 35
Perley, D. A., Taggart, K., Dahiwale, A., & Fremling, C. 2020b, TNSCR, 2020-2766, 1
Perley, D. A., Taggart, K., Dahiwale, A., & Fremling, C. 2020c, TNSCR, 2020-2383, 1
Pessi, P., Mitra, A., Holas, A., et al. 2021, TNSCR, 2021-1178, 1
Pessi, T., Prieto, J. L., Monard, B., et al. 2022, ApJ, 928, 138
Planck Collaboration, Ade, P. A. R., Aghanim, N., et al. 2016, A&A, 594, A13
Podsiadlowski, P., Joss, P. C., & Hsu, J. J. L. 1992, ApJ, 391, 246
Poidevin, F., Perez-Fournon, I., Angel, C. J., et al. 2021, TNSCR, 2021-1738, 1
Poidevin, F., Perez-Fournon, I., Angel, C. J., et al. 2022a, TNSCR, 2022-1758, 1
Poidevin, F., Perez-Fournon, I., Clavero, R., et al. 2022b, TNSCR, 2022-2439, 1
Pollas, C., Albanese, D., Benetti, S., Bouchet, P., & Schwarz, H. 1995, IAUC, 6170, 1
Prentice, S., Maguire, K., Magee, M., et al. 2021a, TNSCR, 2021-903, 1
Prentice, S., Maguire, K., Magee, M., et al. 2021b, TNSCR, 2021-1334, 1
Prentice, S. J., Maguire, K., Skillen, K., Magee, M. R., & Clark, P. 2019a, TNSCR, 2019-1306, 1
Prentice, S. J., Maguire, K., Skillen, K., Magee, M. R., & Clark, P. 2019b, TNSCR, 2019-2659, 1

Prieto, J., Garnavich, P., Depoy, D., et al. 2005, CBET, 302, 1
Prieto, J. L., Kistler, M. D., Thompson, T. A., et al. 2008, ApJL, 681, L9
Puls, J., Vink, J. S., & Najarro, F. 2008, A&ARv, 16, 209
Pursiainen, M., Charalampopoulos, P., Paraskeva, E., Leloudas, G., & Zimmerman, E. 2021, TNSCR, 2021-1767, 1
Quist, V., Jepsen, K. S., Madsen, M. V., et al. 2020, TNSCR, 2020-2493, 1
Ransome, C. L., Habergham-Mawson, S. M., Darnley, M. J., James, P. A., & Percival, S. M. 2022, MNRAS, 513, 3564
Ransome, C. L., Habergham-Mawson, S. M., Darnley, M. J., et al. 2021, MNRAS, 506, 4715
Ransome, C. L., Villar, V. A., Tartaglia, A., et al. 2024, ApJ, 965, 93
Reguitti, A., Pignata, G., Pastorello, A., et al. 2024, A&A, 686, A231
Reusch, S., & Stein, R. 2019, TNSCR, 2019-2610, 1
Reynolds, D. A. 2009, in Encyclopedia of Biometrics, ed. S. Z. Li & A. Jain (Boston: Springer), 741
Richardson, D., Jenkins, R. L. I., Wright, J., & Maddox, L. 2014, AJ, 147, 118
Ryder, S., Staveley-Smith, L., Dopita, M., et al. 1993, ApJ, 416, 167
Salmaso, I., Cappellaro, E., Tartaglia, L., et al. 2025, A&A, 695, A29
Sana, H., de Mink, S. E., de Koter, A., et al. 2012, Sci, 337, 444
Schaefer, B. E., & Roscherr, B. 1998, IAUC, 7058, 2
Schlegel, E. M. 1990, MNRAS, 269, 244
Schlegel, E. M., Kirshner, R. P., Huchra, J. P., & Schild, R. E. 1996, AJ, 111, 2038
Schneider, F. R. N., Podsiadlowski, P., Laplace, E., et al. 2024, A&A, 686, A45
Schrøder, S. L., MacLeod, M., Loeb, A., Vigna-Gómez, A., & Mandel, I. 2020, ApJ, 892, 13
Schulze, S., Chu, M., Dahiwale, A., & Fremling, C. 2022, TNSCR, 2022-1282, 1
Schulze, S., Skan, M., Cehula, J., et al. 2021a, TNSCR, 2021-1593, 1
Schulze, S., Skan, M., Cehula, J., et al. 2021b, TNSCR, 2021-1699, 1
Schulze, S., & Sollerman, J. 2022, TNSCR, 2022-2630, 1
Sedgwick, T. M., Baldry, I. K., James, P. A., Kaviraj, S., & Martin, G. 2021, arXiv:2106.13812
Sheng, X., Ridley, E., Aamer, A., et al. 2022, TNSCR, 2022-3211, 1
Shiode, J. H., & Quataert, E. 2014, ApJ, 780, 96
Shirley, R., Perez-Fournon, I., Angel, C. J., et al. 2020a, TNSTR, 2020-2897, 1
Shirley, R., Perez-Fournon, I., Angel, C. J., et al. 2020b, TNSTR, 2020-147, 1
Shivvers, I., Groh, J. H., Mauerhan, J. C., et al. 2015, ApJ, 806, 213
Shrestha, M., Bostroem, K. A., Sand, D. J., et al. 2024, ApJL, 972, L15
Siebert, M. R., Dimitriadis, G., & Foley, R. J. 2020a, TNSCR, 2020-544, 1
Siebert, M. R., Dimitriadis, G., & Foley, R. J. 2020b, TNSCR, 2020-2271, 1
Siebert, M. R., Taggart, K., Dimitriadis, G., et al. 2020c, TNSCR, 2020-3770, 1
Siebert, M. R., Taggart, K., & Foley, R. J. 2021, TNSCR, 2021-449, 1
Siebert, M. R., Tinyanont, S., Taggart, K., Dimitriadis, G., & Foley, R. J. 2020d, TNSCR, 2020-3121, 1
Smartt, S. J. 2009, ARA&A, 47, 63
Smartt, S. J., Eldridge, J. J., Crockett, R. M., & Maund, J. R. 2009, MNRAS, 395, 1409
Smith, N. 2006, ApJ, 644, 1151
Smith, N. 2011, MNRAS, 415, 2020
Smith, N. 2013, MNRAS, 434, 102
Smith, N. 2014, ARA&A, 52, 487
Smith, N. 2017, in Handbook of Supernovae, ed. A. W. Alsabti & P. Murdin (Cham: Springer), 403
Smith, N., & Andrews, J. E. 2020, MNRAS, 499, 3544
Smith, N., Andrews, J. E., Milne, P., et al. 2024, MNRAS, 530, 405
Smith, N., Andrews, J. E., Rest, A., et al. 2018, MNRAS, 480, 1466
Smith, N., & Arnett, W. D. 2014, ApJ, 785, 82
Smith, N., Chornock, R., Li, W., et al. 2008, ApJ, 686, 467
Smith, N., Ganeshalingam, M., Chornock, R., et al. 2009a, ApJL, 697, L49
Smith, N., Gehrz, R. D., Hinz, P. M., et al. 2003, AJ, 125, 1458
Smith, N., & Hartigan, P. 2006, ApJ, 638, 1045
Smith, N., Hinkle, K. H., & Ryde, N. 2009b, AJ, 137, 3558
Smith, N., Kilpatrick, C. D., Mauerhan, J. C., et al. 2017, MNRAS, 466, 3021
Smith, N., Li, W., Foley, R. J., et al. 2007, ApJ, 666, 1116
Smith, N., Li, W., Miller, A. A., et al. 2011, ApJ, 732, 63
Smith, N., Li, W., Silverman, J. M., Ganeshalingam, M., & Filippenko, A. V. 2011, MNRAS, 415, 773
Smith, N., Mauerhan, J. C., Cenko, S. B., et al. 2015, MNRAS, 449, 1876
Smith, N., Mauerhan, J. C., Kasliwal, M. M., & Burgasser, A. J. 2013, MNRAS, 434, 2721
Smith, N., Mauerhan, J. C., & Prieto, J. L. 2014, MNRAS, 438, 1191
Smith, N., Miller, A., Li, W., et al. 2010, AJ, 139, 1451
Smith, N., Silverman, J. M., Chornock, R., et al. 2009c, ApJ, 695, 1334
Smith, N., & Tombleson, R. 2015, MNRAS, 447, 598
Smith, N., Vink, J. S., & de Koter, A. 2004, ApJ, 615, 475
Soker, N. 2022, MNRAS, 516, 4942
Soker, N., & Kashi, A. 2013, ApJL, 764, L6
Soker, N., & Tylenda, R. 2006, MNRAS, 373, 733
Sollerman, J., Cumming, R. J., & Lundqvist, P. 1998, ApJ, 493, 933
Sollerman, J., Meynardie, W., Chu, M., & Fremling, C. 2023a, TNSCR, 2023-272, 1
Sollerman, J., Meynardie, W., Chu, M., & Fremling, C. 2023b, TNSCR, 2023-301, 1
Sollerman, J., Mörtsell, E., Davis, T. M., et al. 2009, ApJ, 703, 1374
Speagle, J. S. 2020, MNRAS, 493, 3132
Stanek, K. Z. 2019, TNSTR, 2019-83, 1
Stanek, K. Z. 2022, TNSTR, 2022-2111, 1
Stanek, K. Z., & Kochanek, C. S. 2020, TNSTR, 2020-394, 1
Stathakis, R. A., & Sadler, E. M. 1991, MNRAS, 250, 786
Steele, T. N., Cobb, B., & Filippenko, A. V. 2009, CBET, 2011, 1
Steele, T. N., Silverman, J. M., Ganeshalingam, M., et al. 2008, CBET, 1275, 1
Stritzinger, M., Folatelli, G., & Morrell, N. 2008, CBET, 1218, 1
Stritzinger, M., Prieto, J. L., Morrell, N., & Pignata, G. 2011, CBET, 2623, 2
Stritzinger, M., Taddia, F., Fransson, C., et al. 2012, ApJ, 756, 173
Strolger, L.-G., Dahlen, T., Rodney, S. A., et al. 2015, ApJ, 813, 93
Strolger, L. G., Seguel, J. C., Krick, J., et al. 2000, IAUC, 7524, 2
Strotjohann, N. L., Ofek, E. O., Gal-Yam, A., et al. 2021, ApJ, 907, 99
Strotjohann, N. L., Ofek, E. O., Gal-Yam, A., et al. 2024, ApJ, 960, 72
STScI Development Team, 2018 synphot: Synthetic Photometry Using Astropy, v1.1.2, Astrophysics Source Code Library, ascl:1811.001
Suzuki, A., Nicholl, M., Moriya, T. J., & Takiwaki, T. 2021, ApJ, 908, 99
Taddia, F., Stritzinger, M. D., Phillips, M. M., et al. 2012, A&A, 545, L7
Taddia, F., Stritzinger, M. D., Sollerman, J., et al. 2013, A&A, 555, A10
Taddia, F., Sollerman, J., Fremling, C., et al. 2015, A&A, 580, A131
Taddia, F., Sollerman, J., Fremling, C., et al. 2019, A&A, 621, A71
Taggart, K. 2023, TNSCR, 2023-1802, 1
Tartaglia, L., Pastorello, A., Sollerman, J., et al. 2020, A&A, 635, A39
Thoene, C., de Ugarte Postigo, A., Leloudas, G., Cano, Z., & Maeda, K. 2015, ATel, 8417, 1
Thompson, T. A., Prieto, J. L., Stanek, K. Z., et al. 2009, ApJ, 705, 1364
Tonry, J., Denneau, L., Heinze, A., et al. 2018a, TNSTR, 2018-1830, 1
Tonry, J., Denneau, L., Heinze, A., et al. 2019a, TNSTR, 2019-1168, 1
Tonry, J., Denneau, L., Heinze, A., et al. 2019b, TNSTR, 2019-1694, 1
Tonry, J., Denneau, L., Heinze, A., et al. 2019c, TNSTR, 2019-687, 1
Tonry, J., Denneau, L., Heinze, A., et al. 2019d, TNSTR, 2019-2217, 1
Tonry, J., Denneau, L., Heinze, A., et al. 2020a, TNSTR, 2020-3053, 1
Tonry, J., Denneau, L., Heinze, A., et al. 2020b, TNSTR, 2020-894, 1
Tonry, J., Denneau, L., Heinze, A., et al. 2020c, TNSTR, 2020-3053, 1
Tonry, J., Denneau, L., Heinze, A., et al. 2020d, TNSTR, 2020-3216, 1
Tonry, J., Denneau, L., Heinze, A., et al. 2020e, TNSTR, 2020-1024, 1
Tonry, J., Denneau, L., Heinze, A., et al. 2020f, TNSTR, 2020-1028, 1
Tonry, J., Denneau, L., Heinze, A., et al. 2020g, TNSTR, 2020-3173, 1
Tonry, J., Denneau, L., Heinze, A., et al. 2021a, TNSTR, 2021-771, 1
Tonry, J., Denneau, L., Heinze, A., et al. 2021b, TNSTR, 2021-836, 1
Tonry, J., Denneau, L., Heinze, A., et al. 2021c, TNSTR, 2021-1136, 1
Tonry, J., Denneau, L., Heinze, A., et al. 2021d, TNSTR, 2021-2665, 1
Tonry, J., Denneau, L., Heinze, A., et al. 2021e, TNSTR, 2021-2818, 1
Tonry, J., Denneau, L., Heinze, A., et al. 2021f, TNSTR, 2021-312, 1
Tonry, J., Denneau, L., Weiland, H., et al. 2022a, TNSTR, 2022-828, 1
Tonry, J., Denneau, L., Weiland, H., et al. 2022b, TNSTR, 2022-928, 1
Tonry, J., Denneau, L., Weiland, H., et al. 2022c, TNSTR, 2022-1050, 1
Tonry, J., Denneau, L., Weiland, H., et al. 2023, TNSTR, 2023-2550, 1
Tonry, J., Stalder, B., Denneau, L., et al. 2018b, TNSTR, 2018-1186, 1
Tsuna, D., Murase, K., & Moriya, T. J. 2023, ApJ, 952, 115
Tucker, M. A. 2021a, TNSCR, 2021-913, 1
Tucker, M. A. 2021b, TNSCR, 2021-2720, 1
Tucker, M. A. 2023, TNSCR, 2023-2697, 1
Tucker, M. A., Payne, A. V., Do, A., Huber, M. E., & Shappee, B. J. 2019a, TNSCR, 2019-514, 1
Tucker, M. A., Payne, A. V., Do, A., et al. 2019b, TNSCR, 2019-515, 1
Turatto, M., Cappellaro, E., Danziger, I. J., et al. 1993, MNRAS, 262, 128
Van Dyk, S. D., Peng, C. Y., King, J. Y., et al. 2000, PASP, 112, 1532
van Loon, J. T., Cioni, M. R. L., Zijlstra, A. A., & Loup, C. 2005, A&A, 438, 273
van Marle, A. J., Smith, N., Owocki, S. P., & van Veelen, B. 2010, MNRAS, 407, 2305
Villar, V., Berger, E., Miller, G., et al. 2019, ApJ, 884, 83
Villar, V. A., Berger, E., Metzger, B. D., & Guillochon, J. 2017, ApJ, 849, 70

Villar, V. A., Nicholl, M., & Berger, E. 2018, ApJ, 869, 166
Villar, V. A., Hosseinzadeh, G., Berger, E., et al. 2020, ApJ, 905, 94
Villi, M. 2018, TNSCR, 2018-2012, 1
Vink, J. S., & de Koter, A. 2002, A&A, 393, 543
Virtanen, P., Gommers, R., Oliphant, T. E., et al. 2020, NatMe, 17, 261
Wang, S. Q., Wang, L. J., & Dai, Z. G. 2019, RAA., 19, 063
Weil, K. E., & Milisavljevic, D. 2020, TNSCR, 2020-3472, 1
Weis, K., & Bomans, D. J. 2005, A&A, 429, L13
Wenger, M., Ochsenbein, F., Egret, D., et al. 2000, A&AS, 143, 9
Woosley, S. E. 2017, ApJ, 836, 244
Woosley, S. E., Blinnikov, S., & Heger, A. 2007, Natur, 450, 390
Woosley, S. E., & Smith, N. 2022, ApJ, 938, 57
Wu, S. C., & Fuller, J. 2022, ApJ, 930, 119
Yamanaka, M., Okushima, T., Arai, A., Sasada, M., & Sato, H. 2010, CBET, 2539, 1
Yan, L. 2020, TNSCR, 2020-2662, 1
Yan, L., Dahiwale, A., & Fremling, C. 2020a, TNSCR, 2020-2261, 1
Yan, L., Perley, D., Schulze, S., et al. 2020b, TNSCR, 2020-2663, 1
Yang, M., Bonanos, A. Z., Jiang, B., et al. 2023, A&A, 676, A84
Yaron, O., & Gal-Yam, A. 2012, PASP, 124, 668
Yaron, O., Perley, D. A., Gal-Yam, A., et al. 2017, NatPh, 13, 510
Yoon, S.-C., & Cantiello, M. 2010, ApJL, 717, L62
Young, D. 2016, TNSTR, 2016-61, 1
Zhang, J. 2019, TNSCR, 2019-2611, 1
Zhang, J., Wang, X., József, V., et al. 2020, MNRAS, 498, 84
Zwicky, F. 1964, ApJ, 139, 514